

DIESEL ENGINE AIR HANDLING STRATEGIES FOR FUEL EFFICIENT
AFTERTREATMENT THERMAL MANAGEMENT
&
CONNECTED AND AUTOMATED CLASS 8 TRUCKS

A Dissertation

Submitted to the Faculty

of

Purdue University

by

Alexander H. Taylor

In Partial Fulfillment of the

Requirements for the Degree

of

Doctor of Philosophy

December 2018

Purdue University

West Lafayette, Indiana

THE PURDUE UNIVERSITY GRADUATE SCHOOL
STATEMENT OF DISSERTATION APPROVAL

Dr. Gregory M. Shaver, Chair

School of Mechanical Engineering

Dr. Peter H. Meckl

School of Mechanical Engineering

Dr. Steven F. Son

School of Mechanical Engineering

Dr. Monika Ivantysynova c/o Dr. John Lumkes

School of Agricultural & Biological Engineering

Approved by:

Dr. Jay P. Gore

Head of the School Graduate Program

To those whose starting line in life is half a lap behind, keep going. Being on time, work ethic, effort, body language, energy, attitude, passion, being coachable, doing extra, and coming prepared require zero talent.

ACKNOWLEDGMENTS

First and foremost, engine tests would not have been possible without the shop staff of the Ray W. Herrick labs: David “Diesel Dave” Meyer, Ryan Thayer, Bob Brown and Ron Evans.

Thank you to Troy Odstrcil (MSME '18) for being my spotter in the Corec weight room and the engine test cell. Jon Ore for your coffee, confabs, and sense. Aswin Ramesh (PhDME '18) the renaissance man, for your voice of reason. Brady Black for the soonest safety check in the history of Herrick Labs engine testing. Miles Droege, fellow region rat, having a record four semesters of undergraduate research, for always giving 100% effort. Eric Holloway for your consistency and structure.

Thank you to all of the students I've mentored over the years (in chronological order): Michael Crawford, David Ross, Nicholas Gaeta, Joseph Wichlinski, Ehsan Esmaeli, Pablo Jimenez-Corredor, Miles Droege, Manya Subbaramaiah, Bella Ding, Conrad Lynch, and Reese Holloway.

Thank you Dr. Greg Shaver for the challenge and access to the wonderful Herrick Labs, and to my committee members for your support.

PREFACE

The work included in this document is intended to be read as an update to my master's thesis, 'Test Cell Set-Up to Enable Drive-Cycle Testing of a Variable Valve Actuation Enabled Camless Diesel Engine.' [1] The master's thesis covered the journey of building an empty test cell, called Test Cell #1, into a research-grade camless diesel engine laboratory capable of both steady-state and drive-cycle experiments. This dissertation discusses i) the new and novel experiments performed in Test Cell #1 to improve fuel efficiency and aftertreatment thermal performance and ii) work performed as part of the DOE-sponsored (Department of Energy) NEXTCAR (NEXT-Generation Energy Technologies for Connected and Automated On-Road Vehicles) project, and leading the project's "Team 2" which created a simulation framework to study connectivity enabled fuel efficiency improvements for class 8 trucks (including platooning). While these two projects are separate entities, the knowledge gained around diesel engine operation, air handling and its impact on fuel efficiency and aftertreatment performance in Test Cell #1 is directly applicable to the NEXTCAR project. Engine displacements, power outputs, fuel consumptions and emissions have all been normalized, where requested, to protect non-disclosure agreements with industry sponsors.

TABLE OF CONTENTS

	Page
LIST OF TABLES	ix
LIST OF FIGURES	xi
SYMBOLS	xxi
ABBREVIATIONS	xxii
GLOSSARY	xxiv
ABSTRACT	xxv
1. INTRODUCTION	1
1.1 Motivation	1
1.1.1 Air Handling on a Variable Valve Actuation Enabled Camless Diesel Engine	1
1.1.2 NEXTCAR: Connected & Automated Class 8 Trucks	8
1.2 Literature Review	10
1.2.1 Commercial Vehicle Regulations	10
1.2.2 Aftertreatment & Thermal Management	13
1.2.3 Cylinder Deactivation	15
1.2.4 Model-Based Compressor Surge Avoidance Algorithm for IC Engines Utilizing Cylinder Deactivation During Motoring Con- ditions	17
1.2.5 Road Grade Quality Necessary for Accurate Fuel Consumption & Performance Predictions in Class 8 Truck Simulation	19
1.2.6 Capturing the Impact of Speed, Grade, and Traffic on Class 8 Truck Platooning	20
1.3 Experimental Setup	22
1.3.1 Test Cell #1 with a Cummins ISB 6.7L Camless VVA Engine Used for Experiments in Chapters 2-4	22
1.4 Contributions	33
1.4.1 Test Cell #1 Set-Up & Drive-Cycle Repeatability	33
1.4.2 Internal Exhaust Gas Recirculation (iEGR)	33
1.4.3 Early Exhaust Valve Opening (EEVO)	34
1.4.4 Cylinder Deactivation (CDA)	34
1.4.5 Compressor Surge	35
1.4.6 Sensitivity Study of Simulation-predicted Fuel Consumption & Performance to Road Grade Data Quality	36

	Page
1.4.7 Simulation Tool Development & Baseline Operation Simulation Framework & Platooning Controller	36
1.5 Outline	37
2. IEGR & EEVO AS AIR HANDLING STRATEGIES FOR “WARM-UP” AFTERTREATMENT THERMAL MANAGEMENT	40
2.1 Motivation	40
2.2 Strategy Descriptions and Steady-State Results at Loaded Idle	44
2.3 Strategies Applied to Idle Portions of the HD-FTP	51
3. CYLINDER DEACTIVATION AS AN AIR HANDLING STRATEGY FOR FUEL EFFICIENT & “STAY-WARM” AFTERTREATMENT THERMAL MANAGEMENT	58
3.1 Motivation	58
3.2 Strategy Description and Steady-State Results at Idle	59
3.3 Strategy Applied to both Idle and 0-3 bar BMEP Portions of the HD-FTP	67
4. MODEL-BASED COMPRESSOR SURGE AVOIDANCE ALGORITHM FOR IC ENGINES UTILIZING CYLINDER DEACTIVATION DURING MOTORING CONDITIONS	74
4.1 Motivation	74
4.2 Methodology	77
4.3 Surge Avoidance Algorithm Applied to Transient Results	83
4.3.1 Model Validation	83
4.3.2 Low Load Results	84
4.3.3 High Load Results	85
5. MAKING THE GRADE: THE SENSITIVITY OF CLASS 8 TRUCK FUEL CONSUMPTION & OPERATIONAL BEHAVIOR PREDICTIONS TO ROAD GRADE DATA QUALITY	89
5.1 Motivation	89
5.2 Grade Determination Methods & Example Results for a Specific Corridor	89
5.2.1 Grade Data Acquisition	89
5.2.2 Grade Post-processing	94
5.2.3 Grade Regression Analysis	97
5.3 Simulation Model Framework	101
5.4 Sensitivity of Model-based Fuel Consumption Predictions to Estimated Grade Error	102
6. CAPTURING THE IMPACT OF SPEED, GRADE, AND TRAFFIC ON CLASS 8 TRUCK PLATOONING	107
6.1 Motivation	107
6.2 Simulation Framework	107

	Page	
6.2.1	Corridor Grade Data Acquisition & Post-processing	107
6.2.2	INDOT Traffic Speed	109
6.2.3	Single Truck Simulation	113
6.2.4	Platooning Trucks Simulation	114
6.3	Results	117
6.3.1	Comparison to Flat Ground Experimental Data	117
6.3.2	Steady-state Flat Ground Platooning	119
6.3.3	Steady-state Uphill and Downhill Platooning	120
6.3.4	West-Bound I-74 in Indiana (Moderate Traffic & Grade) . . .	124
6.3.5	North-Bound I-69 in Indiana (Heavy Grade)	131
6.3.6	Platoon-enabled Fuel Savings - Impact of Speed & Grade . . .	137
7.	SUMMARY AND FUTURE WORK	140
7.1	Summary	140
7.1.1	iEGR & EEVO as Aftertreatment Warm-Up Air Handling Strategies	140
7.1.2	Cylinder Deactivation as an Aftertreatment Stay-Warm Strategy	140
7.1.3	Model-Based Compressor Surge Avoidance Algorithm for IC Engines Utilizing Cylinder Deactivation During Motoring Conditions	141
7.1.4	Road Grade Quality Necessary for Accurate Fuel Consumption & Performance Predictions in Class 8 Truck Simulation	142
7.1.5	Capturing the Impact of Speed, Grade, and Traffic on Class 8 Truck Platooning	143
7.2	Future Work	145
7.2.1	Air Handling on VVA Engine	145
7.2.2	NEXTCAR Project - Connected & Automated Class 8 Trucks	146
	REFERENCES	148
	A. MEAN EFFECTIVE PRESSURES AND THE LOGP-LOGV DIAGRAM	153
	VITA	156

LIST OF TABLES

Table	Page
1.1 2010 U.S. EPA 'Tier IV' Emissions Standards for Heavy-Duty On-Road Engines in g/hp-hr.	11
4.1 Definition and description of variables used in Equations (4.1)- (4.4).	82
5.1 Grade data types available for 5,432 meters of south-bound US 231 in West Lafayette, Indiana, with labels and definitions.	92
5.2 Summary of grade data regression analysis compared to the LiDAR reference, where $\text{Grade}_{\text{AVG}}$ is the average grade, Grade Error is the error in average grade from as calculated by Equation (5.6), and $\text{Grade}_{\text{RMS}}$ is the root mean square (RMS) grade.	99
5.3 Simulation parameters and initial conditions.	102
5.4 Summary of fuel consumption (normalized to the LiDAR baseline) and grade data regression analysis compared to the LiDAR reference, grade error calculated per Equation (5.6).	106
6.1 Experimentally obtained fuel savings of platooning Peterbilt 386 trucks over a baseline single Peterbilt 386 truck compared to simulated platooning Peterbilt 579 trucks fuel savings relative to a single Peterbilt 579 truck. Trucks on flat ground traveling at 28.6 m/s (64MPH) with a platooning distance of 11m (36ft).	118
6.2 Comparison of platooning trucks' fuel savings with a gap setpoint expected to be used in the real world (distance = 16.7 m (54.8 ft)) at high and low speeds. At lower speeds, the platooning trucks save less fuel relative to baseline due to lower absolute aerodynamic drag.	120
6.3 Summary of predicted fuel and energy consumption over a 33.5 mile constant uphill (1% grade) for platooning Class 8 trucks relative to the single Class 8 truck baseline, operating at steady-state and constant speed of 28.6 m/s (64 MPH). Operation downhill (-3% grade) shows no fuel consumption as the trucks are engine braking.	124
6.4 Simulation parameters and initial conditions for west-bound I-74.	124

Table	Page
6.5 Summary of predicted fuel and energy consumption over a 34 mile section of I-74 in Indiana of the platooning Class 8 trucks relative to the single Class 8 truck baseline, using real-time traffic speed data as the reference speed.	128
6.6 A lower speed (24.5 m/s or 54.8 MPH) summary of predicted fuel and energy consumption over a 34 mile section of I-74 in Indiana of the platooning Class 8 trucks relative to the single Class 8 truck baseline.	128
6.7 Summary of predicted fuel and energy consumption over a 60.0 km (37.3 mile) section of I-69 in Indiana of the platooning Class 8 trucks relative to the single Class 8 truck baseline. The corridor's speed limit is used as the speed reference, with an average speed of 24.5 m/s (54.8 MPH).	133
6.8 Summary of predicted fuel and energy consumption over a 60.0 km (37.3 mile) section of I-69 in Indiana of the platooning Class 8 trucks relative to the single Class 8 truck baseline with a higher average speed of 28.2 m/s (63.1 MPH).	136

LIST OF FIGURES

Figure	Page
1.1 A Class 8 truck, on average, consumed the highest volume of fuel per vehicle type in 2015; fuel consumption normalized to the equivalent energy in a gallon of gasoline. [5]	2
1.2 A Class 8 truck travels 2 time as many miles as a transit bus, and 6 times more miles than a passenger car per 2015 data. [5]	2
1.3 Atmospheric NO _x over the USA in 2005 as visualized by the NASA Aura Climate Research Satellite. [7]	4
1.4 Atmospheric NO _x over the USA in 2015 as visualized by the NASA Aura Climate Research Satellite, the decreased concentration is attributed to Tier IV emissions regulations. [7]	4
1.5 Atmospheric concentrations of regulated emissions exceed the NAAQS guidelines in major metropolitan areas. [8]	5
1.6 Atmospheric concentrations of regulated emissions exceed the NAAQS guidelines in major metropolitan areas. [8]	6
1.7 87% of the world population lives in areas which do not meet the WHO guideline for ambient PM 2.5 concentration. [9]	6
1.8 A smog covered New York City in 1966, 4 years before the 1970 US Clean Air Act.	7
1.9 Delhi, India in 2016 - emerging economies in South and Southeast Asia do not yet have stringent emissions regulations, with India agreeing to implement EURO V emissions standards by 2020.	8
1.10 The HD-FTP reaches 850 ft-lbs of torque a maximum speed of 2600 RPM over a 1,200 second test period.	11
1.11 Reductions in NO _x and PM emissions as a result of diesel engine technology. [12]	12
1.12 The BSFC and PM vs. NO _x trade-off curve has been improved by technological advances, such as aftertreatment. [13]	13
1.13 The aftertreatment system as configured in Test Cell #1, including a DOC, DPF, Urea Injector, and SCR. [12]	14

Figure	Page
1.14 Conventional 6 cylinder operation, and three different CDA modes.	16
1.15 An example of compressor surge instigated by transitioning from 6 cylinder operation (white regions) to CDA (gray regions) seen as oscillating and reverse airflow through the compressor.	18
1.16 The bottom-end (shown in red) of the engine testbed is a stock, mid-range Cummins diesel engine.	23
1.17 The turbocharged Cummins engine allows for variable EGR flow and turbocharger geometry.	24
1.18 The PowerTest AC dynamometer (model # ACR-670) is air-cooled and ingests air via a filter shown on the top-left.	25
1.19 A CAD model of the aftertreatment system in Test Cell #1, detailing the layout, was made before installing the system.	26
1.20 Temperature and emissions measurements are made throughout the aftertreatment system, although it is configured to operate in passive (non-dosing) operation, tailpipe emissions are predicted based on measured temperatures and an SCR conversion model.	27
1.21 Tailpipe NOx values reported are predicted based on an SCR model provided by Cummins, Inc. and an assumed SCR efficiency curve provided by Eaton.	28
1.22 Crank angle input to the dSPACE-based controller is used to command valve actuation and avoid piston-valve contact.	29
1.23 3,000 PSIG hydraulic fluid is supplied to the VVA system in Test Cell #1 from a pump in the building's basement.	30
1.24 A weighted backdraft damper dumps excess air from the combustion air duct into Test Cell #1.	32
1.25 Organization chart of the NEXTCAR project, author is lead of Team 2: Simulation.	37
2.1 An example SCR conversion efficiency curve, where the ability of the SCR to convert NOx is a function catalyst bed temperature.	40
2.2 Analysis of the percentage of time spent within 8 different regions of the HD-FTP.	41
2.3 The 6 cylinder fuel economy (FE) baseline uses 2 injections, while thermal management (TM) mode uses 4 late injections; both EEVO and iEGR utilize valvetrain flexibility with the 4 late injections of thermal management mode.	43

Figure	Page
2.4 Both late injections and valvetrain flexibility manipulate the standard diesel P-V diagram to both decrease engine efficiency and increase exhaust temperatures.	45
2.5 Relative to the thermal management mode baseline, both iEGR and EEVO reduce CCE to enable additional fuel energy to the system.	46
2.6 Both iEGR and EEVO have elevated exhaust temperatures at idle, relative to the thermal management baseline, with iEGR having the best fuel-to-temperature trade-off.	48
2.7 iEGR allowed for the highest exhaust heat rate by both reducing EGR cooler loss to 0 (no external EGR) and reducing pumping losses.	49
2.8 The lower AFR iEGR method (dark green, 22AFR) has comparable engine-out NO _x and HC as the thermal management baseline, but produces more PM than the higher AFR iEGR method (light green, 24AFR).	50
2.9 The HD-FTP cycle, with candidate iEGR idle application portions highlighted as gray; After 600 seconds into the "hot start" portion, all strategies produce a peak efficiency SCR so instead fuel is conserved.	52
2.10 iEGR enables SCR outlet temperatures above 250°C faster than the thermal management baseline; after 600 seconds into the hot start, SCR outlet temperatures remain above 250°C, so iEGR is disabled and conventional thermal management operation is enabled.	53
2.11 iEGR reaches 90% SCR efficiency 100 seconds faster than the thermal management baseline.	54
2.12 FE Baseline has the highest cumulative engine-out and predicted tailpipe NO _x , iEGR has higher engine-out NO _x than the TM baseline but due to higher SCR conversion efficiencies throughout the HD-FTP it also has the lowest cumulative tailpipe NO _x	55
2.13 Despite having 12 times higher PM than TM baseline at idle, iEGR only has 6.7% higher cumulative PM over the HD-FTP as a result of low exhaust flow rates at idle.	55
2.14 iEGR fuel consumption during non-idle periods is equivalent to the thermal management baseline because iEGR is disabled during these sections; variability after 600 seconds into the hot start is due to fuel measurement error and run-to-run variance.	56
2.15 With a hypothetical NO _x -Fuel trade-off curve sketched, the marginal reduction in tailpipe NO _x has a higher marginal fuel cost.	57

Figure	Page
3.1 An 8-mode analysis of the HD-FTP reveals that while 43% of time is spent at idle, just 5.84% of fuel is consumed there.	59
3.2 Half-Engine CDA, or 3-cylinder CDA, involves both fuel and valve cut to 3 cylinders.	60
3.3 The half-engine CDA stay-warm strategy (d) involves two after-TDC injections and shows a larger heat release curve due to the engine load being maintained by just 3 of the 6 cylinders.	61
3.4 All thermal strategies involve lower pressure and temperature combustion modes, enabling higher exhaust temperatures by way of either reduced engine efficiency or in-cylinder heat loss.	62
3.5 With 6-cylinder operation as a baseline, half-engine CDA shows the best BTE and therefore best fuel consumption.	64
3.6 As a stay-warm strategy, half-engine CDA allows for 33% reduced fuel consumption over 6-cylinder stay-warm, with temperatures 65°C higher than the 6-cylinder best efficiency point.	65
3.7 Half-engine CDA has the lowest emissions flow rate (g/hr) while also consuming the least amount of fuel.	66
3.8 The cold and hot start HD-FTP speed and torque profiles shown, with red indicating “warm-up”, green indicating “stay-warm” and brown indicating non-idle portions up to 3 bar BMEP where CDA can be applied.	68
3.9 Both CDA strategies and the 6-cylinder thermal management cycles utilize 6-cylinder idle operation until the 600s mark of the hot start, after which they utilize their respective strategies.	69
3.10 Measured engine-out NO _x overlaid with predicted SCR efficiencies and cumulative tailpipe NO _x , all three thermal management strategies have comparable predicted tailpipe NO _x on this scale.	70
3.11 A comparison of fuel consumption for the three strategies, relative to the 6-cylinder thermal management mode reveals that 6-cylinder thermal management diverges from half-engine CDA (middle plot) during the idle sections (green areas) as expected.	71
3.12 HD-FTP Drive-cycle summary, half-engine CDA at idle shifts the NO _x -FC trade-off curve to the left, with CDA up to 3 bar BMEP giving an even better benefit.	73
4.1 Engine airflow measurements over a portion of the HD-FTP detailing negative and oscillatory (surging) airflow after entering 3-cylinder CDA (gray region).	75

Figure	Page
4.2 The surge data from Fig 4.1 plotted on the compressor map, showing rapid fluctuations in airflow, IMP and turbo speed.	75
4.3 Intermittent compressor wheel contact with the compressor housing was caught before catastrophic failure of the blades.	76
4.4 An example of IMP increase upon deactivating from 6-Cylinder to 3-Cylinder operation at 1.2s at 2200RPM and 1.27 bar BMEP.	77
4.5 Intake tract control volume over which conservation of mass is applied. . .	77
4.6 Concept: The increase in IMP triggered by deactivating cylinders may push the future location over the surge line, and thus must be considered.	79
4.7 The algorithm seeks to deactivate the greatest number of cylinders while avoiding surge.	80
4.8 Concept: A staged CDA strategy (6-4-3) reduces the magnitude of the IMP increase and avoids decel surge caused by 6 to 3-cylinder CDA.	81
4.9 The model accurately predicted the IMP increase upon deactivating from 6 to 3 cylinders at 1.2s, which was previously shown in Figure 4.4.	83
4.10 Experimental IMP (1600 RPM/0.44 bar BMEP) when accelerator position snaps from 25% to 0%.	84
4.11 Experimental fresh airflow (1600 RPM/0.44 bar BMEP) when accelerator position snaps from 25% to 0%, staged cylinder deactivation reduces airflow and avoids surge.	85
4.12 Results overlaid on compressor map (1600 RPM/0.44 bar BMEP) when accelerator position snaps from 25% to 0%, staged cylinder deactivation successfully avoids compressor surge.	85
4.13 Experimental IMP (2000 RPM/13.0 bar BMEP) when accelerator position snaps from 71% to 0%, the future IMP prediction model accurately predicts the IMP increase.	86
4.14 Experimental fresh airflow (2000 RPM/13.0 bar BMEP) when accelerator position snaps from 71% to 0%, staged cylinder deactivation reduces airflow while avoiding negative airflow (surge).	87
4.15 Recreating the surge event from Figure 4.2 with the algorithm applied, staged cylinder deactivation was deployed only when surge is not predicted.	87
5.1 Five separate grade datasets are compared for south-bound US 231 near Purdue University in West Lafayette, Indiana	90

Figure	Page
5.2 Elevation for southbound US 231 near Purdue University, acquired from GPS.	91
5.3 Of the grade datasets acquired three methods were used, a) LiDAR from colleagues in Purdue Civil Engineering, b) MTK3339 GPS, and c) IMU pitch, and integrated velocity output.	91
5.4 The GPS unit provides horizontal distance traveled, D , as well as elevation, h , which is used to calculate grade by Equation (5.1)	93
5.5 The IMU pitch is offset due to the mounting configuration on the vehicle, this must be accounted for by subtracting off the offset from the reference LiDAR during a known flat section of road.	94
5.6 The IMU pitch offset was subtracted by finding the difference from the reference LiDAR dataset at a known 0 grade section.	95
5.7 Absolute error in grade for each dataset relative to the reference LiDAR grade, as calculated by Equation (5.5).	96
5.8 The Comm grade dataset (a) provided the best match for the high accuracy LiDAR data, followed by integrating the IMU's velocity output (c) and using the IMU's pitch (d). The economical single antenna GPS without a base station (b) did not provide a good correlation to the reference LiDAR grade.	98
5.9 A limitation of the Comm dataset is that the quality can vary over a route. The Comm grade had missing data for up to 1 km further south on US 231, shown by only two points between the 8,000 and 9,000 m segments, or erroneous data as shown around 9,000 m. That the Comm data was of high fidelity over the same segment where LiDAR grade was available, 0 to 5,432 m, was happenstance.	100
5.10 On another corridor where IMU data was available for comparison, Interstate 69 south of Indianapolis, IN, the Comm dataset is lacking in accuracy and missing points for up to 6 km stretches (particularly around 281-287 km).	100
5.11 Simulation framework for studying the dynamics and fuel consumption of a Class 8 truck with respect to quality of grade data.	101
5.12 A free body diagram of the modeled Class 8 truck, detailing the forces considered: gravity, drag, engine and friction brakes, rolling resistance, and propulsive (motive) force.	102

Figure	Page
5.13 The driver model for all five simulations (from each of the five grade sources) maintained truck speed within 0.67 m/s (1.5 MPH) of the desired speed. The simulation using the GPS grade dataset resulted in a markedly different speed profile as a result of large grade error (up to 6% absolute error).	103
5.14 The simulation performed with the GPS-acquired road grade showed saturation of the engine's braking and propulsive torque, which did not occur with simulations using other road grade datasets.	104
5.15 Simulation of a Class 8 truck, the baseline reference grade obtained by LiDAR with a mean grade of -0.3548% has a normalized fuel consumption of 1.000. Grade acquisition methods that have a higher average grade are predicted to consume more fuel in simulation.	105
5.16 Relative to the LiDAR baseline, the simulation predicted fuel penalty from over estimating average road grade is higher than the fuel benefit from under estimating average road grade.	106
6.1 I-74 is a trucking corridor in Indiana, west-bound I-74 from US 231 to the Illinois border spanning 54.7 km (34 miles) is used as a simulation corridor in this study.	108
6.2 A VectorNav VN-200 IMU is used to obtain grade data for I-74 west-bound in Indiana.	108
6.3 The IMU provides horizontal velocity which is integrated to obtain distance traveled, D, as well as vertical velocity which is integrated to find elevation, h, which is used to calculate grade by Equations (6.1)-(6.3).	109
6.4 Traffic speed data obtained from INDOT for west-bound I-74 at 5PM on a Friday, color code corresponding to traffic speed and the width of the color band demonstrating the percent of an hour spent at that speed.	110
6.5 INDOT traffic speed for west-bound I-74 in Indiana at 5PM on a Friday converted to a reference speed for the simulated Class 8 truck. Due to traffic, the truck is not be able to obtain the posted commercial vehicle speed limit of 29 m/s (65 MPH). Mile Marker 0 (54 km) is at the Illinois state border.	111
6.6 The posted speed limit for north-bound I-69 in Indiana is used as the reference speed for the simulated Class 8 truck. Road grade on I-69 is aggressive, ranging from +/- 5%.	112

Figure	Page
6.7 The single truck simulation framework utilizes a driver model to track a desired speed reference. Unique aspects include: speed reference modified using traffic speed data available from INDOT and road grade for the corridor obtained by the authors with a known quality.	113
6.8 A free body diagram of the modeled Class 8 truck, detailing the modeled forces from aerodynamic drag, engine and friction brakes, rolling resistance, gravity, and propulsive force.	114
6.9 Platooning truck simulation framework: The lead truck utilizes the same driver model to track the speed reference input, while the rear truck is controlled by a commercially available platooning controller. Unique aspects include: speed reference modified using traffic speed data available from INDOT, road grade with a known accuracy for the corridor obtained by the authors, and a commercially available platooning controller automating the rear truck.	115
6.10 Aerodynamic drag coefficient as a function of platoon spacing normalized to that of a single truck, both the lead and rear vehicles have reduced drag in a platoon. [65]	116
6.11 Cumulative fuel consumption from simulation of 11 m (36 ft) spaced platooning Peterbilt 579 trucks traveling at a constant 28.6 m/s (64 MPH) on flat ground, where the lead truck saves 3.61% over a baseline single truck, and the rear truck saves 11.29% for a platoon averaged 7.45% fuel savings.	118
6.12 Traveling at 28.6 m/s (64 MPH) uphill (grade=1%), in steady-state, the platooning trucks with a 16.7 m (54.8 ft) gap save less fuel relative to the single vehicle baseline (4.58% platoon avg. savings) than on flat ground (6.90% platoon avg. savings), but have the same absolute aerodynamic force reduction.	121
6.13 Traveling at 28.6 m/s (64 MPH) downhill (grade=-3%), in steady-state, the platooning controller maintains a gap higher than the setpoint of 16.7 m (54.8 ft) of 16.94 m (55.6 ft). Platooning enabled fuel savings through lower drag forces are not realized downhill as the trucks are engine braking and not consuming fuel.	123
6.14 The single truck baseline and the platooning trucks track the reference speed (set by average traffic speed) throughout the simulation. The rear vehicle in the platoon is able to exceed the reference speed because vehicle cut-ins to the platoon are not considered. The platooning gap set point of 16.7 m is also maintained except during sustained grades of around 2.5% or more.	126

Figure	Page
6.15 Enlargement of Figure 6.14, between 90 and 165 seconds, where a grade of 2.5% caused truck separation to increase to 24 m (78.7 feet). As the lead vehicle performs a down-shift from 12th to 11th gear, its engine torque drops to 0 Nm (despite driver-intended torque being saturated at max torque), the platooning controller matches the drop to 0 Nm such that the rear vehicle does not encroach. The front vehicle, now in a lower gear, is able to out-accelerate the rear vehicle and maintain speed on the grade. The rear vehicle then performs a 12 to 11th gear down-shift and the gap increases to 24 m.	129
6.16 Drag force on the rear truck in the platoon is lower throughout the 57.4 km (34 mile) simulated corridor, and thus requires less engine torque to maintain speed than either the lead truck or the single truck baseline. . .	130
6.17 Cumulative propulsive energy and fueling for the rear truck in the platoon tracks, with some offset, that of the lead and single truck baseline, and results in a lower cumulative propulsive energy and fuel consumption over I-74.	130
6.18 I-69 in Indiana presents challenging road grade for platooning (+/-5%), which results in increased separation distances of up to 34.2 m (112 ft) from the 16.7 m (54.8 ft) setpoint. The reference speed is tracked well throughout the route, except for a section where grade increases to nearly +5% which is not preceded by a downhill (1620 to 1740 s as shown in Figure 6.19).	132
6.19 A zoom-in from Figure 6.18, where the platooning gap increases to 34.2 m (112 ft) due to a limitation of the platooning controller, namely uncoordinated down-shift events where the lead vehicle out-paces the rear vehicle while climbing the hill. The rear vehicle is unable to gain relative speed on the front vehicle until the trucks near the top of the hill (grade=1-2%) and grade decreases.	134
6.20 Although drag forces on both the lead and rear platooning trucks are lower than the single vehicle baseline throughout the 60.0 km (37.3 mile) corridor, engine torque output does not have a noticeable difference as frequent torque saturation is necessary to climb the high (nearly 5%) grades. . .	135
6.21 The simulated platooning Class 8 trucks do not save as much fuel on I-69 as on Indiana's I-74 or the flat-ground highway speed simulations.	136
6.22 The aerodynamic fuel savings on a per-mile basis as calculated per Equation (6.4), normalized to the higher speed I-69 fuel consumption, for high and low average speed platooning on flat ground, I-74 (moderate grade), and I-69 (heavy grade) versus the RMS grade of the route.	138

Figure	Page
6.23 Single vehicle baseline: Composite fuel consumption breakdown (propulsive torque use) for the corridors at both lower and higher average speeds, normalized to the higher speed I-69 fuel consumption. Despite having the same average speed, the velocity profiles are different between the routes (e.g. constant speed for flat ground, non-constant for I-74 per Figure 6.14d), and subsequently have different drag forces and contributions for aerodynamic drag.	139
7.1 All 3 concepts utilize connectivity to enable additional fuel savings, concept 3 involves improved platooning.	146
7.2 The final stage of the NEXTCAR project involves showcasing 20% fuel consumption benefit on two Peterbilt 579 trucks in a platoon on-road in Indiana.	147
A.1 An example LogP-LogV diagram, for in-cylinder pressure and volume.	154

SYMBOLS

$C_{p,-}$	Specific heat constant of fresh air, charge, or exhaust gas
LHV_{fuel}	Lower heating value of the fuel (diesel)
\dot{m}_{air}	Mass flow rate of fresh air entering the engine
$\dot{m}_{charge,-}$	Mass flow rate of charge entering or exiting the cylinders
\dot{m}_{EGR}	Mass flow rate of exhaust gas recirculation
\dot{m}_{exh}	Mass flow rate of exhaust gas leaving from the engine
\dot{m}_{fuel}	Mass flow rate of fuel entering the engine
N	Engine speed (RPM)
$NIMEP$	Net indicated mean effective pressure
$PMEP$	Pumping mean effective pressure
\dot{Q}_{charge}	Rate of heat transfer to the in-cylinder charge
\dot{Q}_{cyl}	Rate of heat loss from the cylinders
\dot{Q}_{EGR}	Rate of heat rejection through the EGR cooler
\dot{Q}_{exh}	Rate of heat transfer to the exhaust stream
\dot{Q}_{other}	Rate of other mechanical/thermal energy loss
T_{amb}	Ambient air temperature
T_{brake}	Brake torque produced by the engine
T_{EM}	Exhaust manifold temperature
T_{IM}	Intake manifold temperature
T_{ref}	Reference temperature, taken as 25°C
$\Delta T_{EGRcooler}$	Temperature drop of the gas across the EGR cooler
TOT	Turbine outlet temperature
V_d	Displaced volume
\dot{W}_{brake}	Brake power developed by the engine
$\dot{W}_{indicated}$	Indicated power developed by the cylinders

ABBREVIATIONS

AFR	Air-Fuel Ratio
AHU	Air Handling Unit
BDC	Bottom Dead Center
BMEP	Brake Mean Effective Pressure
BSFC	Brake Specific Fuel Consumption
BTDC	Before Top Dead Center
BTE	Brake Thermal Efficiency
CAC	Charge Air Cooler
CAD	Crank Angle Degree
CARB	California Air Resources Board
CCE	Closed Cycle Efficiency
CDA	Cylinder Deactivation
CO	Carbon Monoxide
CO ₂	Carbon Dioxide
DOC	Diesel Oxidation Catalyst
DOE	Department of Energy
DPF	Diesel Particulate Filter
ECM	Engine Control Module
ECR	Effective Compression Ratio
EGR	Exhaust Gas Recirculation
EIVC	Early Intake Valve Closing
EPA	Environmental Protection Agency
FE	Fuel Economy
FHA	Federal Highway Administration
GHG	Greenhouse Gas

HD-FTP	Heavy-Duty Federal Test Procedure
HIL	Hardware In the Loop
HSDA	High Speed Data Acquisition
IMP	Intake manifold pressure
ISB	Inline Six B-Series
IVC	Intake Valve Closing
LIVC	Late Intake Valve Closing
LVDT	Linear Variable Differential Transformer
ME	Mechanical Efficiency
MEP	Mean Effective Pressure
NIMEP	Net Indicated Mean Effective Pressure
NO _x	Oxides of Nitrogen
NREL	National Renewable Energy Laboratory
OCE	Open Cycle Efficiency
PM	Particulate Matter
PV	Pressure-Volume
RPM	Rotations per Minute
SCR	Selective Catalytic Reduction
SOI	Start of Injection
TDC	Top Dead Center
TM	Thermal Management
TOT	Turbine Outlet Temperature
UHC	Unburned Hydrocarbons
USDOT	United States Department of Transportation
VGT	Variable Geometry Turbine
VVA	Variable Valve Actuation

GLOSSARY

drive-cycle	transient engine test with a prescribed engine speed and torque over time
dSPACE	data acquisition system for test cell data I/O, manufactured by dSPACE, Inc.
follow / rear	the second truck in a two-truck platoon
GGE	gasoline gallon equivalent - the equivalent volume of gasoline with the same energy content, e.g. a gallon of diesel is 0.88 GGEs
Speedgoat	data acquisition system for test cell data I/O, manufactured by Speedgoat, Inc.
stay-warm	an aftertreatment thermal management mode considering keeping the exhaust aftertreatment components at or above their threshold temperatures
surge	unstable or reverse flow, as in a compressor
tailpipe	the exit of the exhaust system, where emissions leave the system & diffuse into the atmosphere
Test Cell #1	part of the Cummins Power Lab which hosts a Cummins mid-range diesel engine
Test Cell #2	part of the Cummins Power Lab which hosts a Cummins heavy-duty diesel engine
warm-up	an aftertreatment thermal management mode considering warmupping up the exhaust aftertreatment components to their threshold temperatures

ABSTRACT

Taylor, Alexander H. Ph.D., Purdue University, December 2018. Diesel Engine Air Handling Strategies for Fuel Efficient Aftertreatment Thermal Management & Connected and Automated Class 8 Trucks. Major Professor: Gregory M. Shaver, School of Mechanical Engineering.

The United States Environmental Protection Agency (EPA) is charged with protecting human health and the environment. Part of this mission involves regulating heavy-duty trucks that produce particulate matter (PM), unburned hydrocarbons (UHC), carbon dioxide (CO₂), and nitrogen oxides (NO_x). A byproduct of lean burn combustion in diesel engines is NO_x. NO_x output limits from commercial vehicles have been reduced significantly from 10 g/hp-hr in 1979 to 0.2 g/hp-hr in 2010. Additional reductions are expected in the near future.

One pathway to meet future NO_x emissions regulations in a fuel efficient manner is with higher performing exhaust aftertreatment systems through improved engine air handling. As exhaust aftertreatment's capability to convert harmful NO_x into harmless N₂ and H₂O is a function of temperature, a key performance factor is how quickly does the exhaust aftertreatment system heat up (warm-up), and how well does the system stay at elevated temperatures (stay-warm).

When the warm-up strategy of iEGR was implemented over the heavy duty federal test procedure (HD-FTP) drive-cycle, it was able to get the SCR above the critical 250°C peak NO_x conversion threshold 100 seconds earlier than the TM baseline. While iEGR consumed 2.1% more fuel than the TM baseline, it reduced predicted tailpipe NO_x by 7.9%.

CDA implemented as a stay-warm strategy over the idle portions of the HD-FTP successfully kept the SCR above the 250°C threshold for as long as the TM baseline and consumed 3.0% less fuel. Implementing CDA both at idle and from 0 to 3 bar

BMEP consumed an additional 0.4% less fuel, for a total fuel consumption reduction of 3.4%.

A method to predict and avoid compressor surge (which can destroy turbochargers and in fact did so during the HD-FTP experiments) instigated by CDA was developed, as discussed later, and implemented with staged cylinder deactivation to avoid compressor surge.

The literature does not consider the fidelity of road grade data required to adequately predict vehicle fuel consumption and operational behavior. This work addresses this issue for Class 8 trucks by comparing predicted fuel consumption and operation (shifting, engine torque/speed, and braking) of a single Class 8 truck simulated with grade data for the same corridor from different sources. The truth baseline road grade (best fidelity available with LiDAR) was obtained previously. This work compares road grade data to the truth baseline from four other typical methods i) utilizing GPS to record horizontal position and vertical elevation, ii) logging the pitch of a cost effective, commercially available IMU, iii) integrating the horizontal and vertical velocities of the same IMU, and iv) a commercially available dataset (Comm). Comm grade data ($R^2=0.992$) best matches the LiDAR reference over a 5,432 m stretch of US 231 where high quality LiDAR data was available, followed in quality by the integrated IMU velocity road grade ($R^2=0.979$). Limitations of the Comm dataset are shown, namely missing road grade (decreased point density) for up to 1 km spans on other sections of US 231, as well as for Interstate 69. Vehicle simulations show that both the Comm data (where available and accurate) and integrated IMU road grade data result in fuel consumption predictions within 2.5% of those simulated with the truth reference grade data.

The simulation framework described in Chapter 6 combines high fidelity vehicle and powertrain models (from Chapter 5) with a novel production-intent platooning controller. This controller commands propulsive engine torque, engine-braking, or friction-braking to a rear vehicle in a two-truck platoon to maintain a desired following distance. Additional unique features of the framework include high fidelity road grade

and traffic speed data. A comparison to published experimental platooning results is performed through simulation with the platooning trucks traveling at a constant 28.6 m/s (64 MPH) on flat ground and separated by 11 m (36 ft). Simulations of platooning trucks separated by a 16.7 m (54.8 ft) gap are also performed in steady-state operation, at different speeds and on different grades (flat, uphill, and downhill), to demonstrate how platooning affects fuel consumption and torque demand (propulsive and braking) as speed and grade are varied. For instance, while platooning trucks with the same 16.7 m gap at 28.6 m/s save the same absolute quantity of fuel on a 1% grade as on flat ground (1.00 per-mile, normalized), the trucks consume more fuel overall as grade increases, such that relative savings for the platoon average decrease from 6.90% to 4.94% for flat vs. 1% grade, respectively. Furthermore, both absolute and relative fuel savings improve during platooning as speed increases, due to increase in aerodynamic drag force with speed. There are no fuel savings during the downhill operation, regardless of speed, as the trucks are engine braking to maintain reasonable speeds and thus not consuming fuel. Results for a two-truck platoon are also shown for moderately graded I-74 in Indiana, using traffic speed from INDOT for a typical Friday at 5PM. A 16.7 m (54.8 ft) gap two-truck platoon decreases fuel consumption by 6.18% over the baseline without degradation in trip time (average speed of 28.3 m/s (63.3 MPH)). The same platooning trucks operating on aggressively graded I-69 in Indiana shows a lower platoon-average 3.71% fuel savings over baseline at a slower average speed of 24.5 m/s (54.8 MPH). The impact of speed variation over, and grade differences between, these realistic routes (I-74 & I-69) on two-truck platooning is described in detail.

1. INTRODUCTION

1.1 Motivation

1.1.1 Air Handling on a Variable Valve Actuation Enabled Camless Diesel Engine

The transportation sector emits the second largest amount of greenhouse gas (GHG) in the United States, with a contribution of 27% of total GHG emissions. [2]. Heavy-duty trucking is the largest contributor to GHG emissions out of the freight transportation segment. According to the U.S. Department of Transportation (USDOT), heavy-duty trucks account for 64% of all freight transported in the USA in 2015 by weight. [3] Heavy duty trucks transport 16.5 billion tons of freight annually. [4] USDOT forecasts an increase of 44% in the number of tons transported by heavy-duty trucks leading up to 2045.

According to the Federal Highway Administration (FHA), in 2015 a Class 8 truck on average consumed almost 13,000 gasoline-gallon-equivalents (GGEs). [5] A GGE is a unit of fuel volume normalized to the same energy content as a gallon of gasoline which allows both gasoline and diesel engine vehicles to be compared. The average annual fuel use per vehicle type in 2015 is shown in Figure 1.1, with Class 8 trucks consuming the highest volume of fuel.

The FHA also detailed that Class 8 trucks traveled the highest number of miles, on average, at roughly 68,000 miles per vehicle in 2015. [5] A typical Class 8 truck is expected to travel double the next highest annual mileage vehicle, a transit bus, per Figure 1.2, and nearly 6 times more miles than a passenger car.

Per the EPA's report on 'Nitrogen Oxides, Why and How They are Controlled', there are three pathways for NO_x production: i) thermal NO_x, ii) fuel NO_x, and iii) prompt NO_x. [6] Thermal NO_x is generated in high temperature combustion,

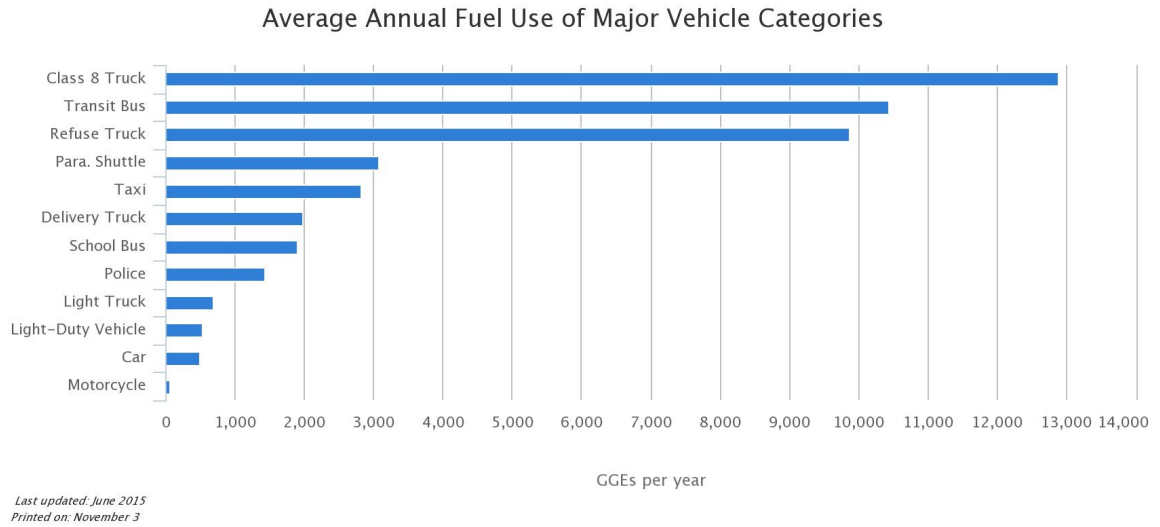


Figure 1.1. A Class 8 truck, on average, consumed the highest volume of fuel per vehicle type in 2015; fuel consumption normalized to the equivalent energy in a gallon of gasoline. [5]

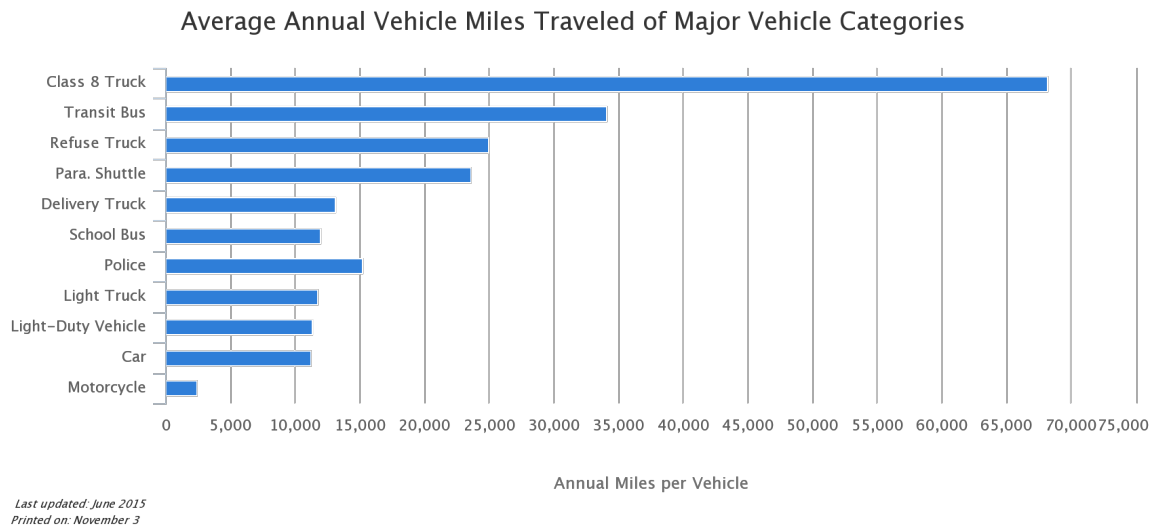


Figure 1.2. A Class 8 truck travels 2 times as many miles as a transit bus, and 6 times more miles than a passenger car per 2015 data. [5]

primarily over 1,300°C via the Zeldovich mechanism, shown in Equations (1.1)-(1.3). This mechanism generates NO_x as a function of both combustion temperature and air-to-fuel ratio (AFR). Air handling strategies can be implemented on diesel engines to either reduce AFR or improve aftertreatment performance, as will be discussed later. The upper limit for NO_x generated is the amount of available oxygen, which is roughly 200,000 ppm in ambient air. The almost always lean operation of the diesel engine lends itself to high engine-out NO_x concentrations due to the lack of a throttle and subsequent high AFR. As much as 90% of NO_x in the atmosphere is as a result of human activity, and ambient NO_x is the primary source for the generation of Ozone. [6]



Figures 1.3 and 1.4 detail atmospheric concentrations of NO_x as viewed by the NASA Aura Climate Research Satellite in 2005 and 2015. The decrease in NO_x concentrations during this time period is attributed to EPA Tier IV emissions regulations by researchers in the NASA Health and Air Quality Applied Science Team (HAQAST). [7] The major industrial and population centers of the midwest and northeast saw reductions in NO_x concentration.

Despite nationwide improvements in atmospheric NO_x concentrations, regions of the United States still struggle to meet air quality standards 365 days a year. Shown in Figure 1.5 are regions which are classified as “nonattainment” zones for any of the six national ambient air quality standards (NAAQS) regulated pollutants: PM, sulfur dioxide, lead, CO, NO_x, and ozone. [8] This figure highlights that emissions are still an issue in major metropolitan areas.

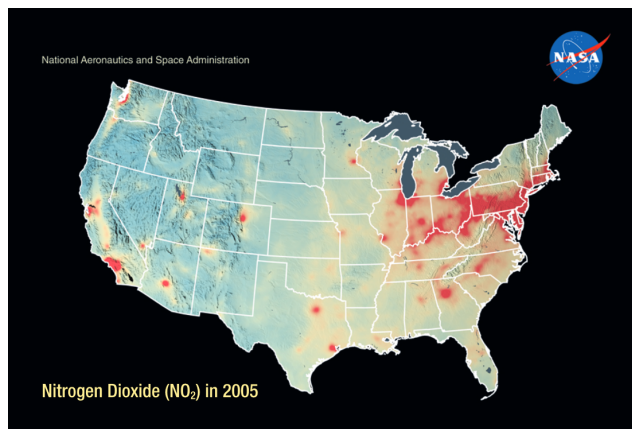


Figure 1.3. Atmospheric NO_x over the USA in 2005 as visualized by the NASA Aura Climate Research Satellite. [7]

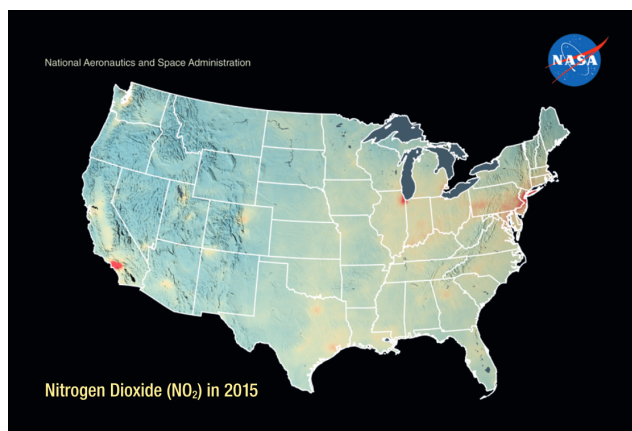
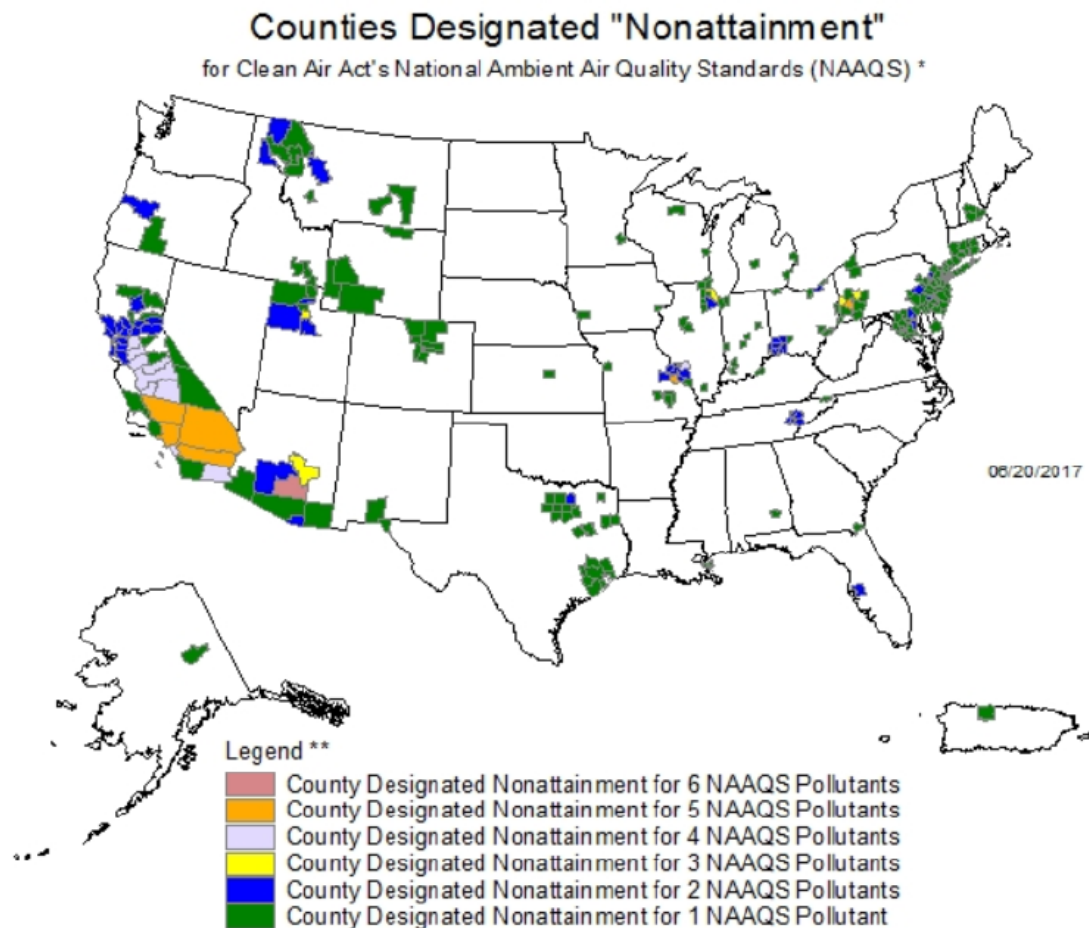


Figure 1.4. Atmospheric NO_x over the USA in 2015 as visualized by the NASA Aura Climate Research Satellite, the decreased concentration is attributed to Tier IV emissions regulations. [7]

Figure 1.6 shows that one of the six NAAQS regulated pollutants, ozone, reaches concentrations up to 9 parts-per-billion. [8] These peak ozone concentrations are located down-wind of both mobile and stationary NO_x emissions sources such as Class 8 trucks and coal-fired power plants.

According to Bruaer, et al., globally in 2010 3.2 million deaths were attributable to ambient particulate matter exposure, namely PM 2.5, with ozone exposure contributing to an additional 152,000 deaths. [9] PM 2.5 is particulate matter with a



Source: US EPA

<https://www3.epa.gov/airquality/greenbook/mapnpoll.html>

Figure 1.5. Atmospheric concentrations of regulated emissions exceed the NAAQS guidelines in major metropolitan areas. [8]

diameter of 2.5 micrometers or smaller. The same study states that while PM and Ozone levels in developed countries dropped in the period from 1990 to 2013, increases in air pollution in South and Southeast Asia drove a 20.4% increase in global population-weighted PM 2.5. Global distribution of ambient PM 2.5 is shown in Figure 1.7, with 87% of the world's population living in areas exceeding the World Health Organization's (WHO) PM 2.5 guideline of 20 micrograms/m³.

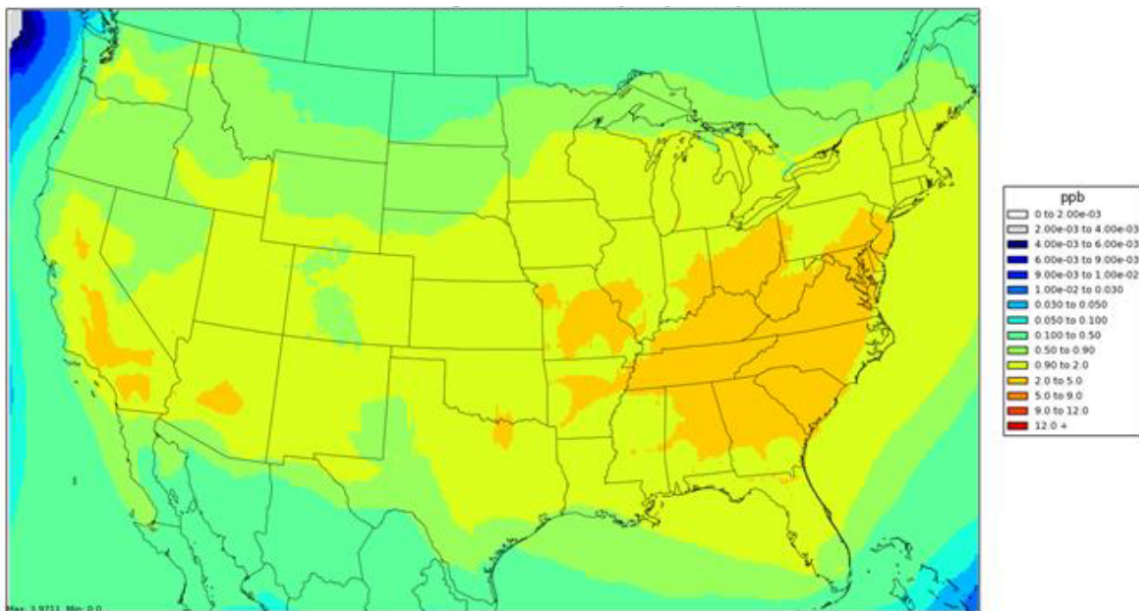


Figure 1.6. Atmospheric concentrations of regulated emissions exceed the NAAQS guidelines in major metropolitan areas. [8]

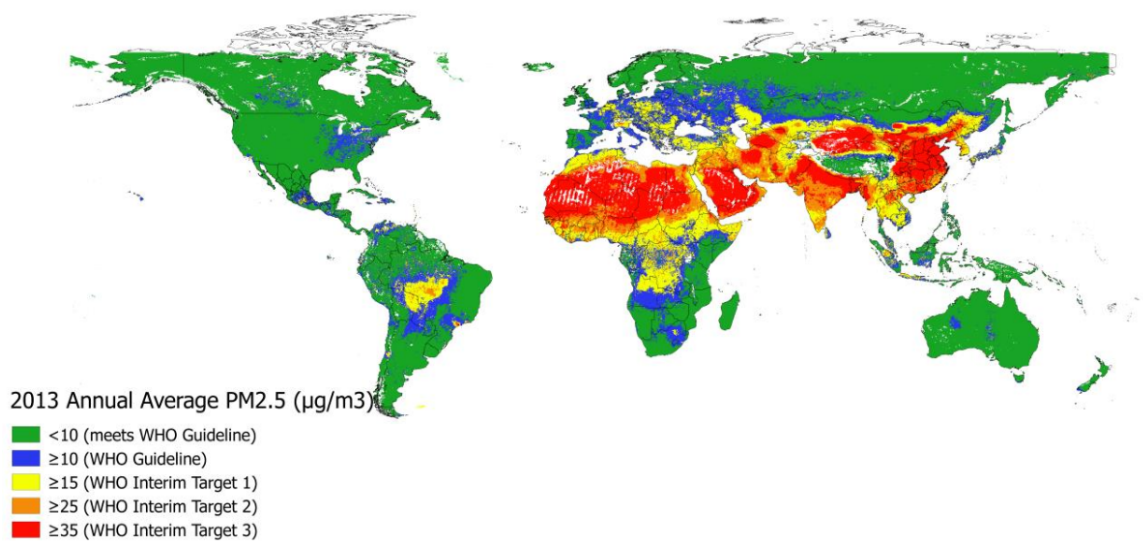


Figure 1.7. 87% of the world population lives in areas which do not meet the WHO guideline for ambient PM 2.5 concentration. [9]

While American cities have improved air quality due to federal regulations, emerging economies in South and Southeast Asia are transitioning through a period of limited regulation and high air pollution. New York City smog in 1966 is shown in Figure 1.8, four years before the 1970 US Clean Air Act. Delhi, India smog from 2016 is shown in Figure 1.9. The Indian government announced in 2016 that it will adopt Euro V emissions standards by 2020, which caps NO_x output to 1.5 g/hp-hr or roughly 7.5 times that of the U.S. EPA's Tier IV standards. Euro VI standards are the equivalent of the U.S. Tier IV standards with an allowable 0.2 g/hp-hr NO_x.



Figure 1.8. A smog covered New York City in 1966, 4 years before the 1970 US Clean Air Act.



Figure 1.9. Delhi, India in 2016 - emerging economies in South and Southeast Asia do not yet have stringent emissions regulations, with India agreeing to implement EURO V emissions standards by 2020.

1.1.2 NEXTCAR: Connected & Automated Class 8 Trucks

Line-haul Class 8 trucks account for approximately two-thirds of greenhouse gas (GHG) emissions of all commercial trucks. Industry leaders have continued to develop and take advantage of new technologies to increase fuel efficiency and reduce GHG emissions by looking at the vehicle as a system. However, the engine and transmission have remained largely isolated from emerging Connected and Automated Vehicle (CAV) applications such as cooperative adaptive cruise control, predictive cruise, speed harmonization, and freight signal priority. In response to this technology void, the ARPA-E sponsored project Next-Generation Energy Technologies for Connected and Automated On-Road Vehicles, or NEXTCAR, aims to develop technology that takes advantage of emerging connectivity infrastructure. A Purdue University-led team includes innovative industry leaders Peloton Technology, Cummins, ZF, and Peterbilt, as well as the National Renewable Energy Laboratory (NREL). The goal is an integrated, connectivity-enabled, vehicle-dynamic and powertrain control system for diesel-powered on-highway Class 8 trucks. Concepts to be studied include (1) remote powertrain calibrations that take into account variables such as application

variation, component aging, terrain, and weather, (2) real-time powertrain control and optimization from the cloud that allows for more sophisticated algorithms to be implemented, and (3) more efficient two-truck platooning using connectivity-enabled shifting coordination and lead truck predictive cruise. The combination of these concepts is hypothesized to reduce fuel consumption by up to 20% from the 2016 Peterbilt 579 baseline.

Connectivity will allow for more sophisticated air handling strategies to be implemented, such as better control of the engine air pathways through EGR and VGT actuators using ‘lookahead’ information. An example, informed by testing performed on the VVA engine, is operating the engine of the follow-truck in the platoon with an open VGT. In general, diesel engines operate with excess airflow and a spooled-up (at higher speed, via squeezed VGT) turbocharger at most operating conditions in preparation for better and faster transient response to requested torque. If the engine controller on the follow-truck had information from the lead-truck such as flat terrain or constant future demand for torque, the controller could open the VGT, slowing down the turbo speed and lowering both exhaust and intake manifold pressures allowing for fuel savings through reduced engine pumping work.

1.2 Literature Review

1.2.1 Commercial Vehicle Regulations

Commercial diesel engines require exhaust aftertreatment systems to meet the EPA's 2010 Tier 4 Final emissions regulations. [10] Aftertreatment systems involve a diesel oxidation catalyst (DOC), diesel particulate filter (DPF), urea injection device also known as a diesel emissions fluid doser (DEF doser), and selective catalytic reduction (SCR) system.

Current NOx regulations in the United States are 0.2 g/hp-hr at the tailpipe as shown in Table 1.1, but future proposals, including from the California Air Resources Board (CARB) propose up to a 90% reduction to 0.02 g/hp-hr. Sharp et al. predicts that a further 90% reduction in allowable NOx emissions will require a significant shift in diesel engine and aftertreatment technology, including i) an engine calibration to increase the warm-up rate of the SCR, ii) low temperature NOx storage, iii) a mini-burner in the exhaust to facilitate faster SCR warm-up, and iv) an advanced SCR catalyst with model-based controls for ammonia slip and coverage. [11] Examples of the technological improvements which were required to meet current NOx and PM regulations are shown in Figure 1.11. The values specified in Table 1.1 are maximum allowable emissions as measured over the HD-FTP, a standardized heavy duty drive-cycle shown in Figure 1.10. The cycle is used for regulatory emissions testing of heavy-duty on-highway engines (40 CFR 86.1333). Per federal regulations, the HD-FTP drive-cycle is performed as two tests: a cold start followed by a 20 minute soak with the engine turned off and a hot start. Emissions and fuel consumptions are reported as a weighted average of the two tests per Equations (1.4) and (1.5).

$$Emissions = \frac{1}{7} \times ColdStart + \frac{6}{7} \times HotStart \quad (1.4)$$

$$FuelConsumption = \frac{1}{7} \times ColdStart + \frac{6}{7} \times HotStart \quad (1.5)$$

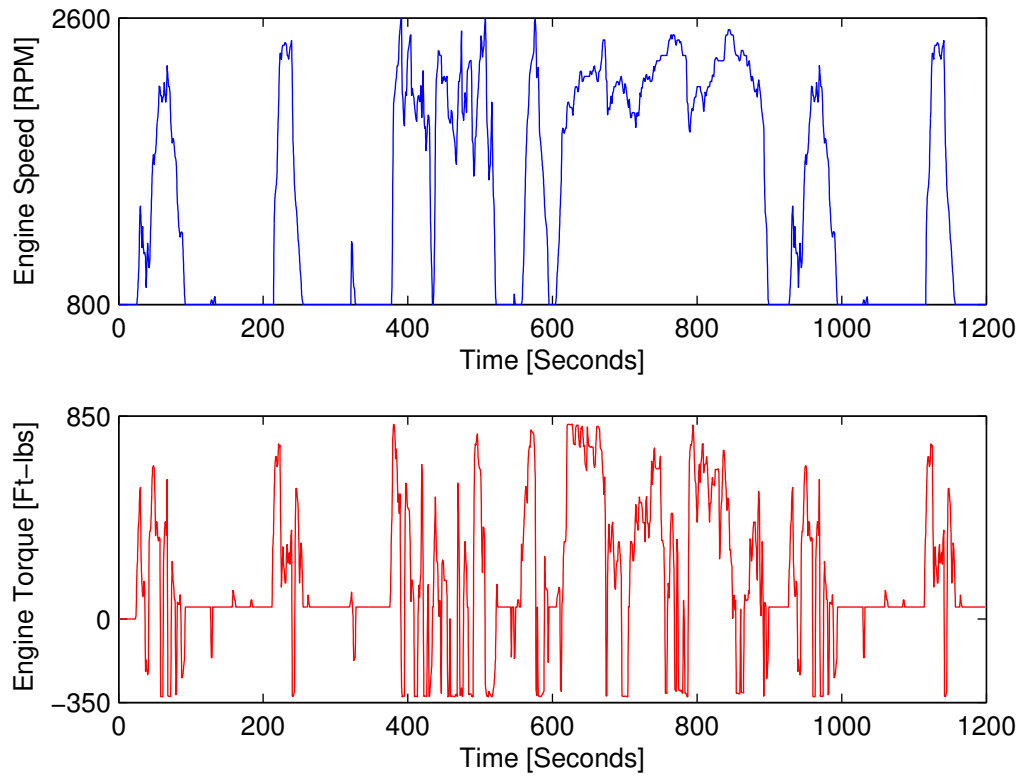


Figure 1.10. The HD-FTP reaches 850 ft-lbs of torque a maximum speed of 2600 RPM over a 1,200 second test period.

Table 1.1. 2010 U.S. EPA 'Tier IV' Emissions Standards for Heavy-Duty On-Road Engines in g/hp-hr.

CO	UHC	NO _x	PM
15.5	0.14	0.20	0.01

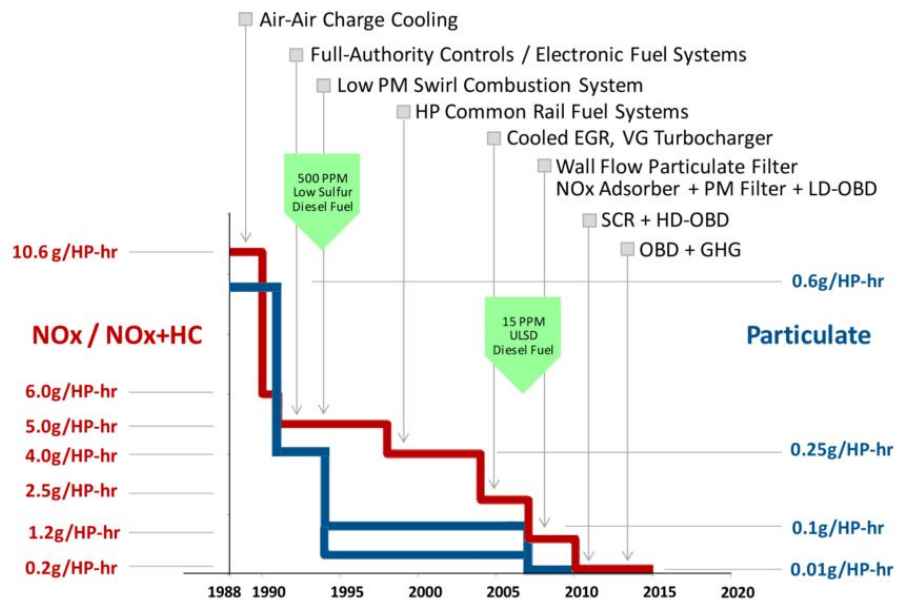


Figure 1.11. Reductions in NOx and PM emissions as a result of diesel engine technology. [12]

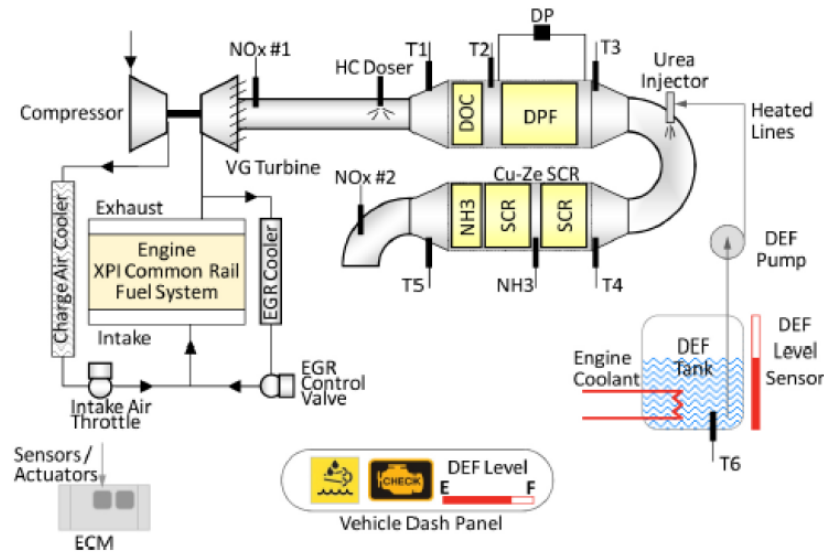


Figure 1.13. The aftertreatment system as configured in Test Cell #1, including a DOC, DPF, Urea Injector, and SCR. [12]

Internal Exhaust Gas Recirculation for Thermal Management

Turning off the external EGR loop allows for higher exhaust flow and temperatures, but higher engine-out NO_x. [14] Closing the EGR valve and preventing the routing of exhaust gas through the EGR loop yields decreased heat loss to the engine coolant due to reduced or no flow through the EGR cooler, shown in the engine air pathways schematic in Figure 1.17. Kim et. al found that iEGR is effective at reducing engine-out NO_x, has a faster response time than the low pressure EGR loop, and correlated NO_x formation to in-cylinder adiabatic flame temperature. [15] When implemented at a loaded idle condition, iEGR is capable of increasing exhaust gas temperatures up to 404°C, compared to the baseline operation of 141°C. [16] Reference [17] used a second exhaust valve event to re-induct exhaust gases into the cylinder, resulting in higher engine-out temperatures.

Early Exhaust Valve Opening as a Thermal Management Tool

The flexible valvetrain enabled air handling strategy of EEVO allows for a reduction of engine efficiency and subsequent lower AFR and higher exhaust temperatures. Reference [18] shows that 30° early EVO used on a variable valve actuation engine at 1500 RPM and 1 bar BMEP raises exhaust temperatures enough for DOC activation (oxidation of unburned hydrocarbons), but increased fuel consumption by 9.6%. Roberts, et. al. predicts a 30 to 90°C increase in exhaust temperatures with 90° early EEVO, enough to allow for peak SCR efficiency at loaded idle. [19] Gosala et al. found that implementing EEVO at loaded idle reached temperatures as high as 346°C, relative to the baseline operation of 141°C. [16]

1.2.3 Cylinder Deactivation

Cylinder deactivation is not used on commercially available diesel engines today, but is found on 27.4% of light duty gasoline trucks and 2.7% of passenger cars for a total market penetration of 13% in light duty vehicles sold in 2015. [20] On the six cylinder engine in Test Cell #1, CDA is implemented as either 4, 3 or 2 cylinders active as shown in Figure 1.14. Operating with either 1 or 5 active cylinders is avoided due to resonance issues which could damage the drive-shaft and dynamometer. [1] CDA reduces engine pumping work (improved volumetric and open-cycle efficiency) through decreased engine airflow and heat loss to the coolant through the cylinder walls (improved closed cycle efficiency), which results in a fuel consumption benefit. [21] A flexible valvetrain capable of closing both the intake and exhaust valves is necessary to implement this air handling technique. The diesel engine air handling strategy of CDA allows for lower airflow through the engine in the same manner that decreasing throttle position would on a spark ignition engine. Schenk, et. al. used a Cummins ISB 6 cylinder engine and found the following benefits of CDA applied at low speeds and loads over the HD-FTP: i) 5.6% reduction in fuel consumption, ii) 76°C higher engine outlet temperatures compared to conventional operation, and iii)

39°C higher SCR inlet temperatures which improved aftertreatment performance. [22] Schenk. et al. also noted that the lower mass flow of CDA resulted in a large temperature delta between the engine-out and SCR-inlet. Barath, et. al. found that CDA allowed for elevated exhaust temperatures (high enough for DOC activation), but with 36.5% better fuel consumption at a condition of 1500 RPM and 1 bar BMEP. [18] Lu, et al. found that CDA implemented at a highway cruise condition raised exhaust temperatures by 170 to 220°C, which allows for passive DPF regeneration. [23]

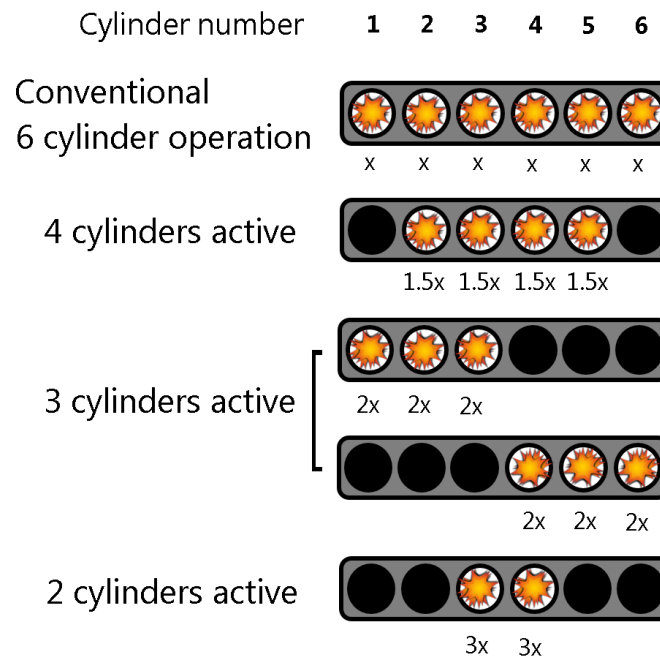


Figure 1.14. Conventional 6 cylinder operation, and three different CDA modes.

Joshi et al. also applied CDA at steady-state idle and found a 4.0% fuel consumption benefit with 65°C higher exhaust temperatures compared to conventional engine operation, and a 25% fuel consumption benefit over the thermal management baseline. When applied to idle and low speeds and loads over the HD-FTP, Joshi et al. recorded a 3.4% fuel consumption benefit over the thermal management baseline. [24]

Operating a 6 cylinder engine with fewer active cylinders brings with it noise, vibration and harshness (NVH) issues, which dynamic skip fire strategies can help to mitigate. [25, 26]

1.2.4 Model-Based Compressor Surge Avoidance Algorithm for IC Engines Utilizing Cylinder Deactivation During Motoring Conditions

CDA can also be implemented on some, or all, cylinders during engine motoring events to reduce the cool-off rate of the aftertreatment components. [24] An undesirable consequence of decreasing demanded chargeflow during the onset of motoring events via cylinder deactivation is a phenomenon known as 'deceleration' compressor surge or 'decel' surge, for short. [27] [28] For example, deactivating 3 of the 6 cylinders during the onset of motoring creates a flow restriction in the system in a manner similar to the impact of sudden throttle closure in a turbo-charged SI engine. The subsequent deceleration of the airflow moving through the intake manifold system will increase the intake manifold pressure (IMP) significantly. The combination of increased IMP (e.g. compressor outlet pressure) and reduction in airflow through the compressor can push the compressor into surge. [29] When this happens, airflow through the compressor flows in reverse (shown in Figure 1.15), halting rotation of the compressor and turbine as the intake tract empties. This severe form of surge is often called deep decel surge. Galindo, et al. studied deep compressor surge, quantifying oscillations in the intake manifold pressure and fresh airflow signals on the order of 5 to 15 Hz or greater. [30] Therefore, to observe surge events, data logging must take place at a higher frequency.

Sudden deceleration of the compressor wheel, combined with the "hammer blow" of high intake pressure can "immediately destroy the thrust bearing section of the turbomachinery", resulting in loss of engine power and a nonfunctional turbocharger. [31]

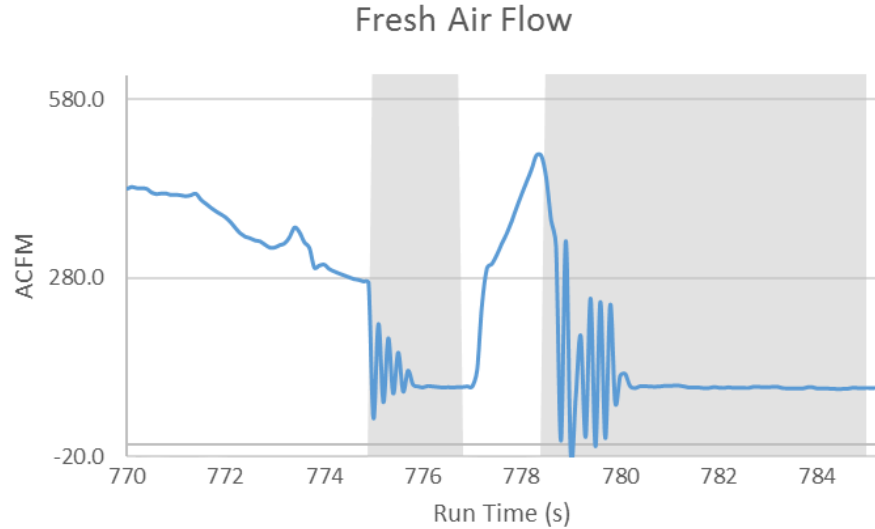


Figure 1.15. An example of compressor surge instigated by transitioning from 6 cylinder operation (white regions) to CDA (gray regions) seen as oscillating and reverse airflow through the compressor.

Current studies into compressor surge on turbo-diesel engines generally consider steady-state operation at or near the surge line of the turbocharger. [32] [33] [34] Kerres, et al. [35] developed a Hurst exponent based mathematical model to detect when airflow and compressor outlet pressure signals become increasingly more oscillatory in nature, a precursor to surge. [36] Similarly, Chen and Dehner studied other algorithms that use oscillations in intake manifold pressure to detect the onset of surge. [37] [38] Anderson et al. determined that the intake system geometry and pulsating fresh airflow from intake valve events impacts the surge limit of a compressor by upwards of 10%. [29] Theotokatos, et al. and Rakopoulos, et al. investigated compressor surge on a turbo-diesel engine during transient events, triggered by a decrease in engine speed while at high boost pressures. [33] [37] This type of compressor surge can damage turbochargers over time, but is fundamentally different from deep compressor surge which is initiated by rapid (as opposed to more gradual) reductions in airflow. Pinsky, et al. studied methods of displacing the compressor surge line via recirculation to allow for more margin to surge. [39] [40] Bozza, et al. used a compressor map to

model surging operation, which motivates the use of the compressor map as a model for compressor mass flow based on turbo speed and IMP. [33]

These prior diesel engine studies do not acknowledge deep decel surge, as this phenomenon is historically only seen on throttle-actuated engines. Throttled, spark-ignition turbocharged engines (common for natural gas and gasoline-fueled applications) typically rely on “blow-off” (e.g., bypass) valves which reduce the mass of air in the intake tract before the compressor has a chance to surge. Such a method could be used on a throttle-less turbo-diesel engine, but would not be necessary if the algorithm outlined in this paper was incorporated.

The study outlined in Chapter 4 presents a physics-based prediction of the IMP increase resulting from CDA during the onset of motoring, as well as an algorithm to reduce the IMP increase through staged cylinder deactivation to avoid compressor surge during the onset of motoring events.

1.2.5 Road Grade Quality Necessary for Accurate Fuel Consumption & Performance Predictions in Class 8 Truck Simulation

Grade information must be incorporated for any reliable model-based prediction of commercial vehicle performance and fuel consumption. This is a result of the significant impact that grade has on the powertrain load required to propel a commercial vehicle. For example, 44.4% of the required powertrain load to maintain a 25 m/s (56 MPH) speed up a 4% incline is due to grade (44.4% & 11.1% are a result of aerodynamic drag and rolling resistance). [41] There are a number of ways to measure or estimate road grade, including i) digital levels, ii) GPS, iii) Inertial Measurement Unit (IMU) pitch, iv) integrating IMU velocity, v) LiDAR, and others, each of which have benefits and challenges. Digital levels, while accurate, require a direct measurement of the road surface that is both time consuming and unsafe on high traffic roads. [42] Zhang et al. showed that GPS data used to calculate road grade without base station correction will not provide a good estimate of road grade. [42] Wood et al. com-

pared road grade obtained by Southwest Research Institute (SwRI) with an inertial measurement unit (IMU) to datasets from the United States Geological Survey and TomTom over a 115 mile stretch of Interstate 10 near San Antonio, TX. [43] Wood found that the TomTom road grade data had an RMSE of 0.3% using SwRI’s IMU data as a reference. IMUs are more expensive than GPS systems, typically selling for \$2,000 to \$12,000 (10-100x more than GPS units). Wood also showed that the commercially available TomTom road grade data varies in quality and availability. [43] Zhang showed that LiDAR provides the best method for estimating road grade. [42] However LiDAR systems are expensive, with pricing up to \$100,000.

Given the above trade-offs in grade measurement/estimate fidelity, availability, expense, and inconvenience, a natural question is, “What level of grade data fidelity is required for model-based prediction of commercial vehicle fuel consumption and, as a result, which grade measurement/estimate methods, if any, are practical?” To the author’s surprise, this answer does not appear in the literature.

1.2.6 Capturing the Impact of Speed, Grade, and Traffic on Class 8 Truck Platooning

A variety of simulation frameworks exist for study of vehicle or powertrain dynamics, fuel consumption, or platooning. [44–54] Most simulation frameworks do not consider traffic, while those that do use a traffic simulator to emulate traffic, such as VISSIM or SUMO. [46, 53, 55] This work fills a gap in existing literature by using real-time, real-world traffic data to augment speed limit data. The impact of real-world road grade, generally not considered in simulation, [46, 48, 49, 53, 54] is included here. The effort described here also provides a new understanding of how grade and speed affect platooning-enabled fuel savings. Real-world road grade for the simulation framework discussed here is obtained by the authors using an inertial measurement unit (IMU) and integrating the velocity output. This method of road grade estimation on another corridor provided an R^2 of 0.979 when compared to a LiDAR system

with 1.42 cm accuracy of the true road elevation. [56] When road grade from an actual corridor has been considered previously in literature, the quality of the grade data is unknown. [44, 45]

Experimental two-truck platooning results have previously demonstrated fuel savings of 2.7-9.7% in Class 8 trucks traveling at highway speeds. [57] Peloton Technology experimentally demonstrated that a production-intent platooning controller is capable of saving 7.25% on flat ground. [58] A comparison of predicted fuel savings from platooning in simulation is made to this experimental data.

1.3 Experimental Setup

1.3.1 Test Cell #1 with a Cummins ISB 6.7L Camless VVA Engine Used for Experiments in Chapters 2-4

Engine Hardware and Dynamometer

The engine testbed in Test Cell #1, used to obtain results for Chapters 2-4, is a 6 cylinder “camless” 2010 Cummins diesel engine. The engine is referred to as camless because the cylinder head was modified such that the intake and exhaust valves are actuated via an electro-hydraulic Variable Valve Actuation (VVA) system instead of the camshaft. The crankshaft, connecting rods, and pistons (i.e., rotating assembly or “bottom end”) of the engine, is unchanged, per Figure 1.16. The cylinder head no longer uses a camshaft and has been modified to incorporate camless operation.

The air handling system of the engine in Test Cell #1 is shown in Figure 1.17, along with the temperature and pressure measurement locations. The engine is equipped with an exhaust gas recirculation (EGR) system, which is coolant-cooled, and a variable geometry turbine (VGT) turbocharger. The ECM controls an electro-actuated valve on the intake manifold which throttles incoming fresh air, coupled with an electro-actuated valve on the EGR system (also ECM controlled) that allows for exhaust flow containing combustion byproducts into the intake manifold when pressure difference between the intake and exhaust manifolds is favorable. Inlet guide vanes on the turbocharger’s exhaust inlet (i.e., VGT) are actuated by the ECM, and direct exhaust flow at or around the turbine wheel to either increase or maintain shaft speed. The VGT is capable of directing 100% of the exhaust flow into the turbine, referred to as “100% squeezed VGT.”

The coolant-cooled engine exchanges heat from its internal engine coolant loop (50% glycol, 50% water) to an external, hydraulically isolated building glycol loop (30% glycol, 70% water) through a water-water heat exchanger. The turbocharged

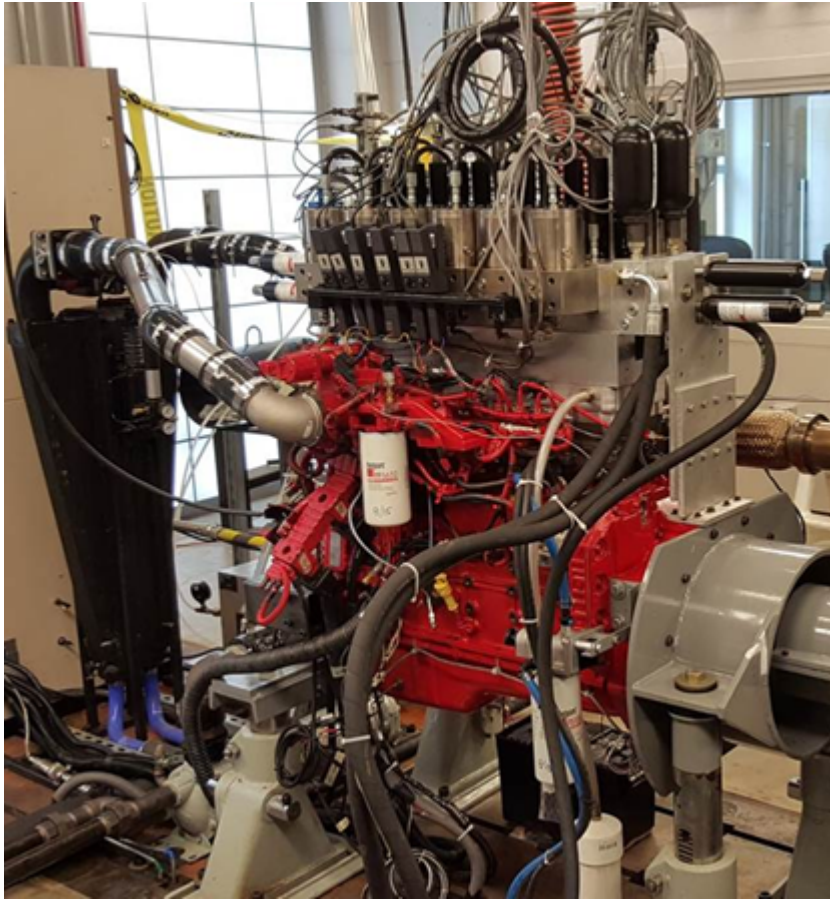


Figure 1.16. The bottom-end (shown in red) of the engine testbed is a stock, mid-range Cummins diesel engine.

air (charge air) exchanges heat through a charge air cooler (CAC) with a chilled water loop, covered later in this section.

A PowerTest AC dynamometer (model # ACR-670) enables HD-FTP and other drive-cycle testing. The AC dynamometer's maximum torque rating is 2,348 ft-lbs at 1,500 RPM (670 horsepower). The dynamometer's maximum speed is 4,200 RPM, at which the torque rating is 837.8 ft-lbs, or 670 horsepower. The dynamometer with air filter (top-left in photo, for the air cooling system) is shown in Figure 1.18. Power from the engine is dissipated by generating electricity and returning it to the electrical grid.

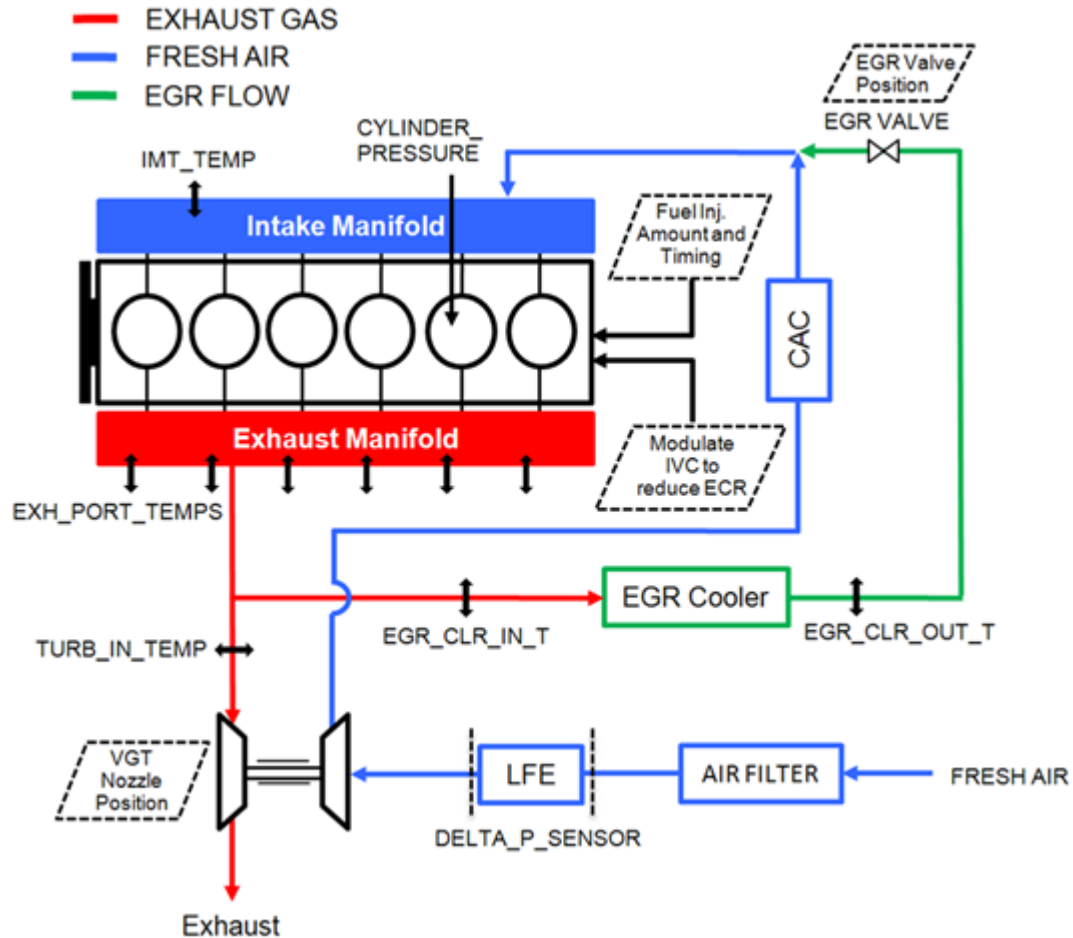


Figure 1.17. The turbocharged Cummins engine allows for variable EGR flow and turbocharger geometry.

The PowerTest software allows for a comma separated variable (.CSV) file to be uploaded which dictates the drive-cycle to be run. The .CSV file has columns for torque, speed, ramp rate and trigger signal voltage inputs at a rate of up to 100 Hz, but 5 Hz (0.2 s intervals) is used for the drive-cycle testing described here. The dynamometer's trigger signal output between 0 and 5V is used to identify sections of the drive-cycle for which to run cylinder deactivation or other air handling strategies, discussed in Chapters 2 & 3. The key FTP drive-cycle which is relevant to the group's diesel engine research is the Heavy Duty Federal Test Procedure (HD-FTP), shown in Figure 1.10.

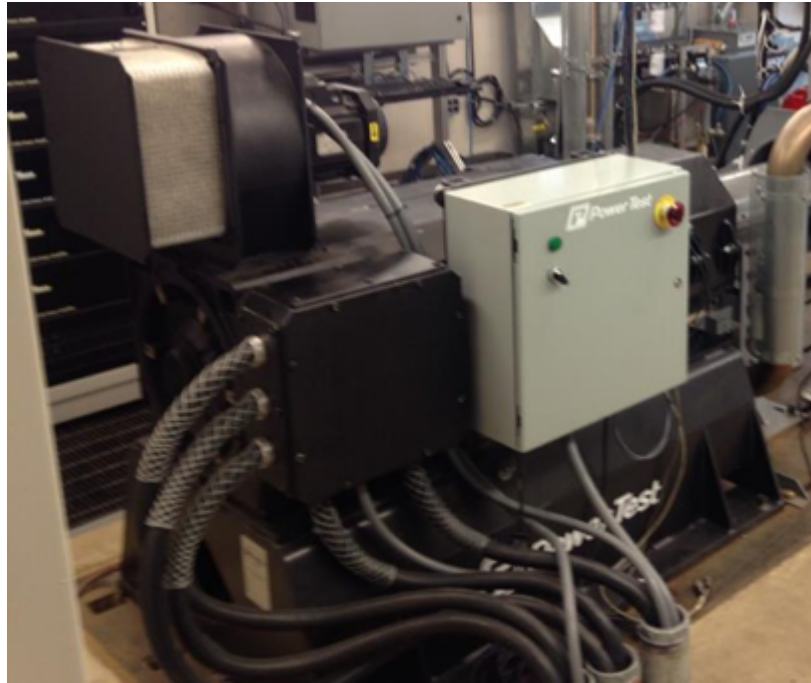


Figure 1.18. The PowerTest AC dynamometer (model # ACR-670) is air-cooled and ingests air via a filter shown on the top-left.

Exhaust Aftertreatment

The design of the exhaust and aftertreatment system is shown in Figure 1.19. There are two potential pathways for exhaust to flow, depending on the type of engine tests being performed. Option #1 is for exhaust to flow through the aftertreatment system (pipes shown in red) as would be performed when performing a steady-state or drive-cycle test where aftertreatment component temperatures are being studied, #2 is for exhaust gas to bypass the aftertreatment system and go downward (gray pipe) before looping back around and out of the test cell. Bypassing of the aftertreatment system is typically performed during engine troubleshooting or tests where aftertreatment component temperatures are not being studied. This extends the lifespan of the DPF which has a limited useful life as it eventually fills with ash from oxidized PM.

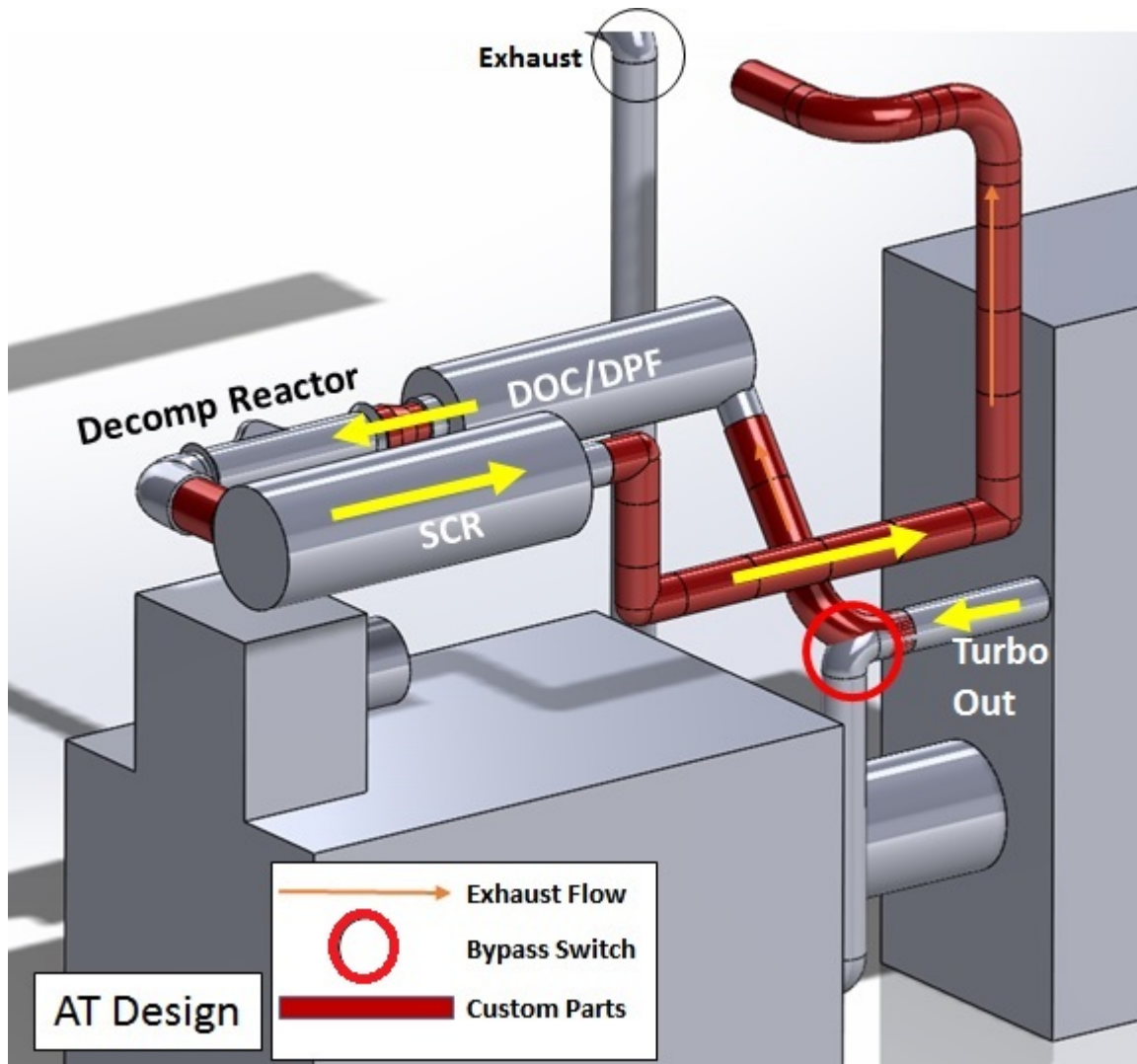


Figure 1.19. A CAD model of the aftertreatment system in Test Cell #1, detailing the layout, was made before installing the system.

The aftertreatment system is composed of three components: i) the combined diesel oxidation catalyst/diesel particulate filter (DOC/DPF), ii) the decomposition reactor where diesel exhaust fluid (DEF) is injected, and iii) the selective catalytic reduction device (SCR). The purpose of the DOC is to capture unburned hydrocarbons and oxidize them, while the DPF is a honeycomb filter which captures particulate matter (soot). The DPF is routinely regenerated, which is a process that involves

oxidation of the captured PM at temperatures above 400°C. Regeneration is triggered when the ECM detects a pressure difference across the DPF beyond a threshold indicating it has trapped a sufficiently large quantity of PM. The DEF injected in the decomp reactor in the form of urea, NH_3 in solution, vaporizes and mixes with the exhaust gas allowing it to catalyze NOx in the SCR - although this function is not enabled for any of the experiments detailed in this document. Temperature measurements at key points of the aftertreatment system are shown in Figure 1.20.

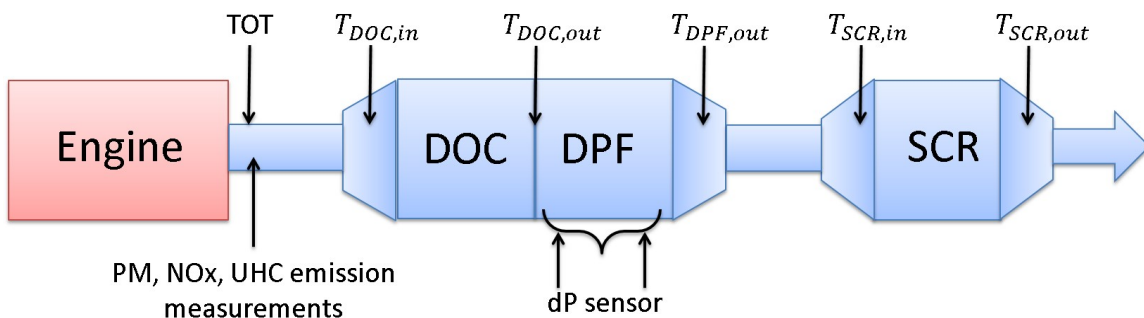


Figure 1.20. Temperature and emissions measurements are made throughout the aftertreatment system, although it is configured to operate in passive (non-dosing) operation, tailpipe emissions are predicted based on measured temperatures and an SCR conversion model.

The aftertreatment system is used in passive operation for the experiments detailed in later sections of this report. Passive operation means that the system does not dose DEF in the decomp reactor, so the quantity of NOx leaving the engine is not converted in the SCR and is equivalent to the NOx leaving the aftertreatment system. Tailpipe NOx is predicted using a model provided by Cummins and an assumed SCR conversion efficiency curve provided by Eaton, shown in Figure 1.21. The DOC/DPF do not require dosing and will capture unburned hydrocarbons and PM, but tailpipe measurements of these reduced emissions are not recorded.

The Cummins aftertreatment model accepts experimental values for exhaust flow rate, engine-out NO_x (PPM), and measured SCR outlet temperature to predict tailpipe NO_x based on the SCR efficiency curve shown. Of the numerous ways to measure SCR catalyst bed temperature (assume it is the SCR inlet temperature, assume an average of the SCR outlet and inlet temperatures, etc), the method chosen was based on input from the engineering team at Cummins, Inc. which is to assume that the SCR catalyst bed temperature is equivalent to the SCR outlet temperature. Since the SCR outlet is downstream of the SCR catalyst bed, using the SCR outlet temperature will always under-predict the actual temperature of the SCR catalyst and thus provides a conservative estimate for actual SCR operation.

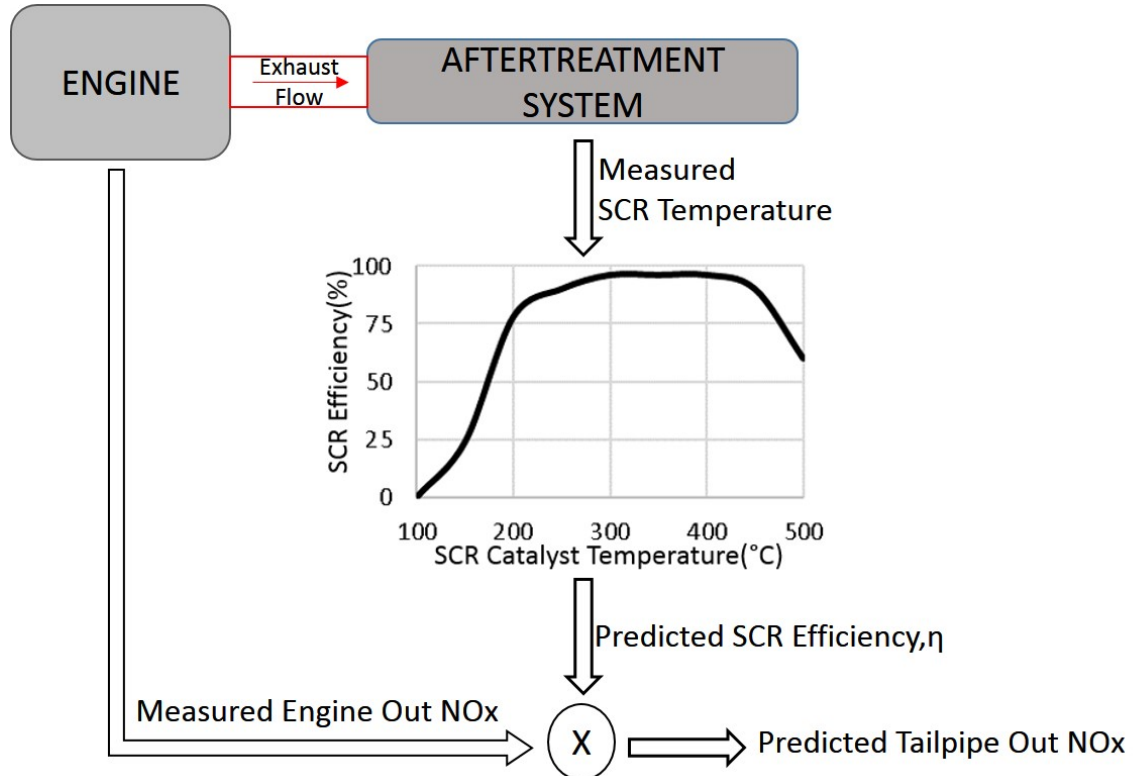


Figure 1.21. Tailpipe NO_x values reported are predicted based on an SCR model provided by Cummins, Inc. and an assumed SCR efficiency curve provided by Eaton.

Variable Valve Actuation System

The intake and exhaust valves of the engine can be actuated independently in pairs (2 intake valves, 2 exhaust valves), and on a cylinder-to-cylinder and cycle-to-cycle basis. The VVA system enables stock valve profile operation, or modified valve operation including different opening and closing timings and lift. Hydraulic fluid at 3,000 PSIG, per Figure 1.22, supplied via a pump in the building's basement provides the motive force for valve operation when electronically signaled by the dSPACE-based controller.

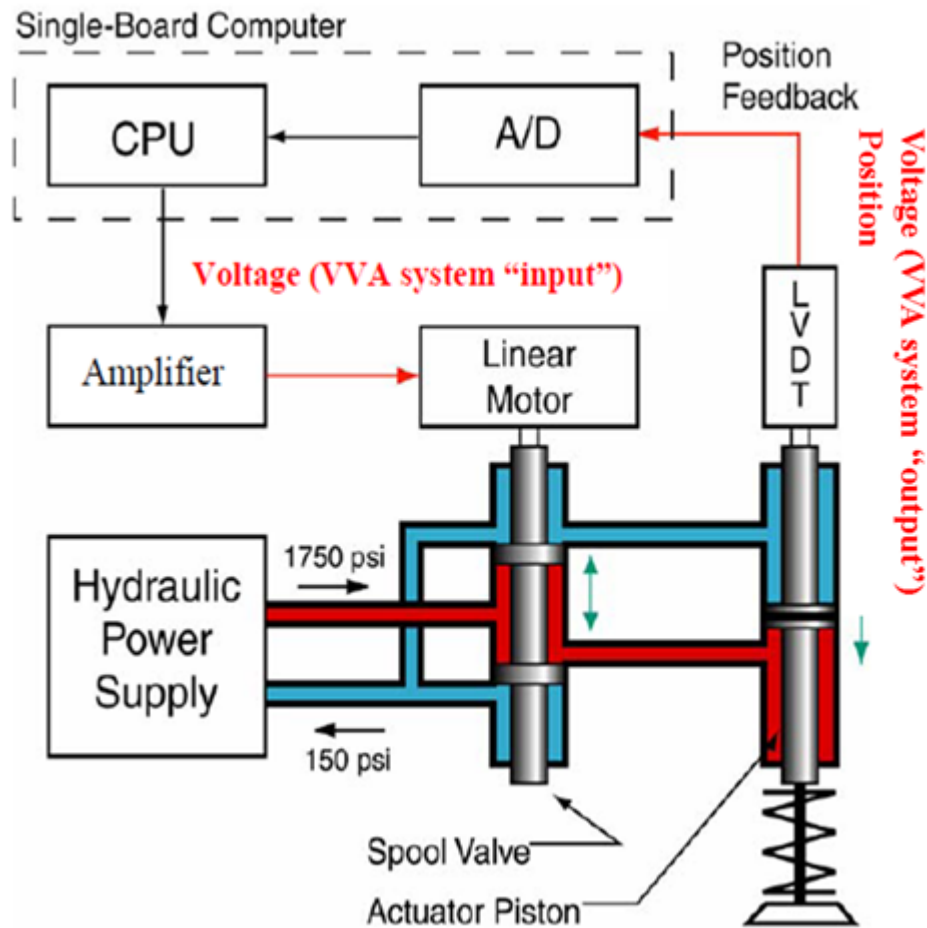


Figure 1.22. Crank angle input to the dSPACE-based controller is used to command valve actuation and avoid piston-valve contact.

Valve position is fed-back via linear variable differential transformers (LVDTs) for both position and health monitoring. The VVA system is equipped with feed-forward control, but a closed-loop controller monitors valve position from the LVDT feedback voltage and adjusts the voltage output in an attempt to make the feedback valve profile match a desired valve profile. The health monitoring (diagnostic) algorithm retracts the valves if the lift varies more than 2.5mm or the opening/closing varies more than 50 degrees from the commanded profile.

An oil-to-water heat exchanger maintains temperature of the hydraulic fluid, which is located next to the hydraulic pump shown in Figure 1.23. Chilled water from a building loop is fed to the oil-to-water heat exchanger to maintain oil temperature at 100°F. The VVA system allows for cylinder deactivation by not only cutting fuel to the cylinders, but also retracting the valves and trapping some mass of air in the cylinders. The trapped mass of air acts as an "air spring", and contracts and expands throughout crank rotation. Cylinder deactivation without valve-cut (not VVA enabled) has pumping losses in the deactivated cylinders as the intake and exhaust valves continue to operate, and the deactivated cylinders continue compressing and pumping air.



Figure 1.23. 3,000 PSIG hydraulic fluid is supplied to the VVA system in Test Cell #1 from a pump in the building's basement.

Conditioned Combustion Air & Charge Air Cooling

Combustion air supplied to the test cell is humidity and temperature controlled. It is recommended that the air handling unit supply twice as much air as is demanded by the engine. [1] The Air Handling Unit (AHU) is a Racan-Carrier design, model # A4D-48/58-DI. The combustion air intake duct has a thermocouple and humidity sensor, which are logged for air mass flow corrections through the LFE.

The recommendation for combustion air systems which are both temperature and humidity controlled is to dump excess conditioned air (via a weighted backdraft damper) into the test cell, as was covered in Reference [1]. The weighted backdraft damper opens when duct pressure exceeds 1 atmosphere. The mechanical damper reacts faster than controlling the supply fan speed (located 120 feet away from the engine inlet in the mezzanine) and prevents supercharging of the engine's compressor inlet. A constant volume flow rate allows for good temperature and humidity control because varying the AHU's flow rate creates dynamic effects between fan speed, the AHU's heat exchangers and steam-injection system as the controller "hunts" for 0 error with the temperature and humidity setpoints.

The engine demands 650 SCFM of airflow at peak torque output, thus the AHU must supply at least 1300 SCFM of flow into Test Cell # 1 per industry standards. An airflow measurement of the combustion air supply duct showed 1,142 SCFM, short of double the engine's demanded airflow. Additional airflow to the test cell could only be provided by increasing system pressures, which the ductwork is not rated to handle.



Figure 1.24. A weighted backdraft damper dumps excess air from the combustion air duct into Test Cell #1.

Data Acquisition System

The VVA system is controlled via simulink code loaded to a dSPACE box. A crankshaft position encoder and LVDTs feed back valve position. dSPACE outputs both intake and exhaust valve profiles, real-time, to amplifiers which then command intake and exhaust valve profiles. The dSPACE system is used for test cell data acquisition at frequencies up to 5,000 Hz.

1.4 Contributions

1.4.1 Test Cell #1 Set-Up & Drive-Cycle Repeatability

As per the author's Masters thesis, test cell set-up and validation of drive-cycle repeatability and data quality were led by the author. [1] A mid-range Cummins cam driven valvetrain engine was used to validate test cell capability and data acquisition before the variable valve actuation camless engine was installed and tested over both the HD-FTP and FTP-72. A fuel consumption and engine-out NO_x repeatability study was performed and repeatability issues were fixed including boundary condition control by installation of conditioned combustion air, CAC water cooling loop, and repair of the fuel measurement system.

Design of the exhaust aftertreatment system was led by the author, although installation and validation was performed with the support of colleagues and the Purdue Research Machine Shop and Herrick Labs Shop staff, including David Meyer and Bob Brown.

1.4.2 Internal Exhaust Gas Recirculation (iEGR)

The air handling strategy of iEGR was first implemented on the VVA engine at steady-state by colleagues, although the precise aftertreatment thermal and fuel consumption impact of variable valvetrain was mixed in with manipulation of conventional engine actuators. The author co-led the task of separating out the impact of conventional engine actuators such as late-injections, EGR position, and VGT position from valvetrain flexibility. This work involved manual screening through experimental steady-state testing of over 50 different combinations of intake and exhaust valve timing and phasing to determine the optimal combination. The author led the testing of this strategy over the HD-FTP both with and without an exhaust aftertreatment system attached, where the former study focused on the impact on

fuel consumption and TOT while the latter focused on aftertreatment temperatures and predicted SCR efficiencies.

1.4.3 Early Exhaust Valve Opening (EEVO)

In the same manner as iEGR, the air handling strategy of EEVO was initially implemented on the VVA engine by both current and former colleagues, but the steady-state results at idle had a mix of conventional engine actuator positions overridden from the base engine calibration. The author led the task of separating out the impact of conventional engine actuators such as late-injections, EGR position, and VGT position from valvetrain flexibility by screening through steady-state testing of early exhaust valve opening from 0° to 100° early. The optimal amount of EEVO was determined by the location which produced the highest exhaust gas temperature but still maintained consistently stable heat release from the fuel injected into the cylinder. Opening the exhaust valve too early yields unstable combustion during the power stroke of the engine. As with iEGR, the author led the activity of testing this strategy over the HD-FTP for comparison with baseline engine operation while colleagues focused on the FTP-72 and drayage cycles.

1.4.4 Cylinder Deactivation (CDA)

CDA had been implemented on the VVA engine at steady-state conditions before moving the engine to the new Test Cell #1. The author led and supported the first transient testing of CDA during idle portions of the HD-FTP in Test Cell #1 without an exhaust aftertreatment attached as covered in the Masters thesis. [1] As with the iEGR and EEVO strategies, support was provided in the activity of separating out the impact of CDA on thermal management at an engine idle condition from the impact of conventional engine actuators such as late fuel injections.

After initial testing of this air handling strategy during idle portions of the HD-FTP without an aftertreatment system, an exhaust aftertreatment system was at-

tached, and again testing of CDA at idle portions over the HD-FTP with a full aftertreatment system was led by the author (while at the time colleagues focused on other drive-cycles such as the FTP-72 and drayage). Drive-cycle testing of CDA at conditions up to 3 bar BMEP over the HD-FTP was led by colleagues but supported by the author.

1.4.5 Compressor Surge

The author identified the root cause of turbocharger failure as compressor surge from implementing CDA during motoring sections of the HD-FTP. Experience rebuilding turbochargers led the author to check for compressor shaft play after noticing i) sluggish engine response to transient events and ii) oil accumulation inside the charge air cooler.

The reduction in demanded air mass flow induced by the transition to CDA while at boosted conditions (high intake manifold pressures) pushes operation at the compressor outlet past the surge line. If operation is sufficiently into the surge region of the compressor map, a phenomenon known as ‘deep surge’ occurs where the intake tract is completely purged of pressurized air via a reversal of flow across the compressor as is discussed in more detail in Chapter 4.

The author informed the team of a method to avoid compressor surge, involving an ad hoc time delay to allow IMP to sufficiently draw down before transitioning to CDA. The concept of future IMP prediction based on conservation of mass and a staged cylinder deactivation algorithm to avoid surge was developed by the author. This algorithm was implemented on the VVA engine with strong support and Simulink model development from Troy Odstrcil. Additional Simulink support and testing was provided with the help of Aswin Ramesh.

1.4.6 Sensitivity Study of Simulation-predicted Fuel Consumption & Performance to Road Grade Data Quality

Commercially available road grade data was found to be lacking both in resolution (number of points) and accuracy. As road grade data is a critical input to a simulation framework used to understand performance and fuel consumption of class 8 trucks, the author took ownership of this problem and found a solution. After scouting vendors at the 2018 Automated Vehicle Symposium, a method that yields high quality road grade data at a reasonable cost was determined through supplier VectorNav, which makes inertial measurement units (IMUs).

Not just believing the VectorNav IMU brochure, the author performed a comparison study of road grade estimation methods for a stretch of US 231 near Purdue University. In comparison to high accuracy LiDAR data (within 1.42 cm of the road's true elevation over 10 m spans) obtained through colleagues in Civil Engineering, integrating the velocity output of the IMU produced a good match for the reference data set ($R^2=0.979$). Five grade estimation methods were considered, and used as input to simulations performed by the author which predicted the performance of a single class 8 truck over the corridor using the various grade sources.

1.4.7 Simulation Tool Development & Baseline Operation Simulation Framework & Platooning Controller

As the lead for the NEXTCAR project's Team 2 (Simulations Team, org chart shown in Figure 1.25), the author created a simulation framework used to study connected and automated class 8 trucks. Revision 0 of the simulation framework used vehicle models that included Newton's 2nd Law based physics (aero drag, rolling resistance, inertia). Through support from project partner Cummins, black box vehicle models which included high fidelity engine and transmission models (as well as their controllers) were integrated into Rev 1 of the simulation framework, as well as a black box variant of a production-intent platooning controller from partner Peloton Tech-

nology. Simulations over real-world corridors (Interstate 74 and 69 in Indiana) were performed by the author, using road grade which was obtained by the author with support from undergraduate researcher Miles Droege. The framework was used to understand the impact of speed and grade on platooning class 8 truck performance and fuel savings.

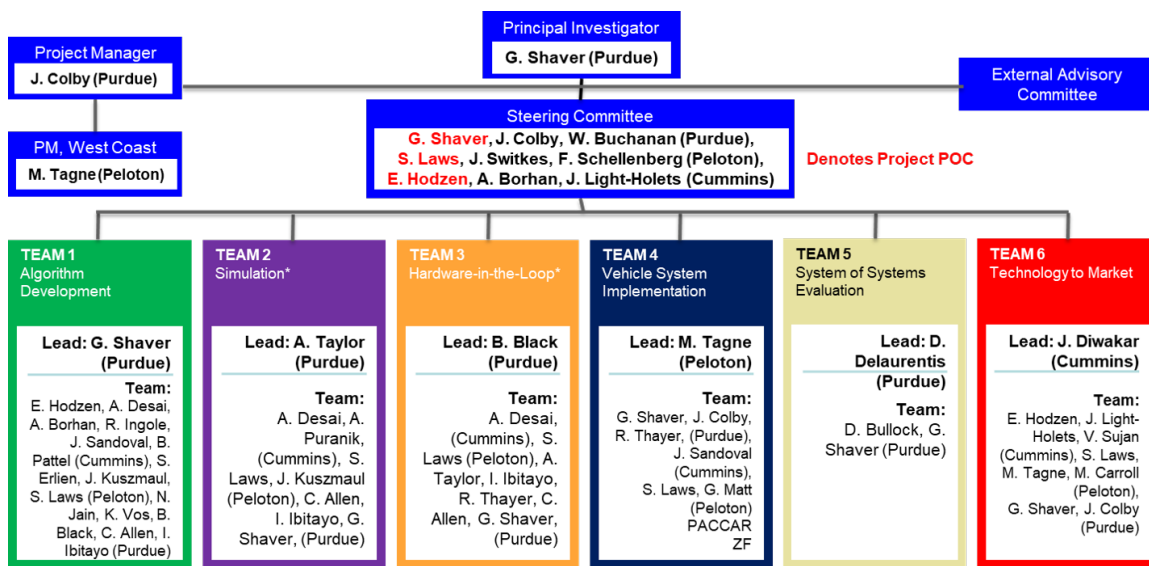


Figure 1.25. Organization chart of the NEXTCAR project, author is lead of Team 2: Simulation.

1.5 Outline

Chapter 2: IEGR & EEVO AS AIR HANDLING STRATEGIES FOR “WARM-UP” AFTERTREATMENT THERMAL MANAGEMENT presents the results of air handling strategies to improve aftertreatment warm-up including early exhaust valve opening (EEVO) and internal exhaust gas recirculation (iEGR). A comparison is made to the state of the art thermal management (TM) baseline.

Chapter 3: CYLINDER DEACTIVATION AS AN AIR HANDLING STRAT-

EGY FOR FUEL EFFICIENT & “STAY-WARM” AFTERTREATMENT THERMAL MANAGEMENT discusses the stay-warm strategy of cylinder deactivation (CDA), which reduces engine airflow and associated air-to-fuel ratio (AFR), the former reducing engine pumping work and the latter yielding higher exhaust temperatures. The current state of the art thermal management engine calibration, thermal management (TM) baseline, does not distinguish between warm-up and stay-warm strategies.

Chapter 4: MODEL-BASED COMPRESSOR SURGE AVOIDANCE ALGORITHM FOR IC ENGINES UTILIZING CYLINDER DEACTIVATION DURING MOTORING CONDITIONS introduces a potential barrier to market for CDA, compressor surge, which was revealed during these experiments that as of this writing is not discussed in literature. Severe compressor surge, known as deep compressor surge, can instantly destroy turbochargers and in fact did so during the HD-FTP experiments described later.

Chapter 5: MAKING THE GRADE: THE SENSITIVITY OF CLASS 8 TRUCK FUEL CONSUMPTION & OPERATIONAL BEHAVIOR PREDICTIONS TO ROAD GRADE DATA QUALITY introduces work began as the Simulations Team Lead developing a simulation framework to study single and platooning class 8 trucks on a new Department of Energy (DOE) Advanced Research Projects Agency - Energy (ARPA-E) sponsored project, Next-Generation Energy Technologies for Connected and Autonomous On-Road Vehicles (NEXTCAR). The scope of the NEXTCAR project is to reduce Class 8 truck fuel consumption by 20% through automated systems (including platooning), connectivity and cloud computing. Connectivity-enabled remote powertrain calibration is expected to improve fuel efficiency by 2.5%, with real-time powertrain control and optimization from the cloud contributing 5%, and finally truck platooning (7.5%) with improved capabilities including coordinated shifting (1%) and predictive cruise incorporation (4%). All three

concepts will first be studied in simulation (the framework developed and described in Chapters 5 & 6), and then ultimately demonstrated on two Peterbilt 579 trucks powered by Cummins heavy-duty engines (covered in the Future Work section).

Chapter 6: CAPTURING THE IMPACT OF SPEED, GRADE, AND TRAFFIC ON CLASS 8 TRUCK PLATOONING extends the work performed as Simulations Team Lead on the NEXTCAR project to a two-truck platoon simulation framework. The current state of the art in two-truck platooning is assessed, using a production-intent platooning controller provided by an industry partner. An understanding of how platooning works, where it saves fuel (and where it doesn't) is provided, leading to next steps for improved platooning discussed in the Future Work section.

2. IEGR & EEVO AS AIR HANDLING STRATEGIES FOR “WARM-UP” AFTERTREATMENT THERMAL MANAGEMENT

2.1 Motivation

The SCR does not reach peak conversion efficiency until temperatures above 250°C, as shown in Figure 2.1. During the cold start segment of the HD-FTP, the SCR is initially at an ambient temperature (25°C in the case of these laboratory experiments), where NO_x conversion efficiency is 0%. This means that NO_x emissions out of the engine are the same as seen at the tailpipe. It is advantageous to warm-up the SCR to peak conversion temperature as quickly as possible so that the engine can switch to a more fuel efficient mode with the trade-off of increased engine-out NO_x.

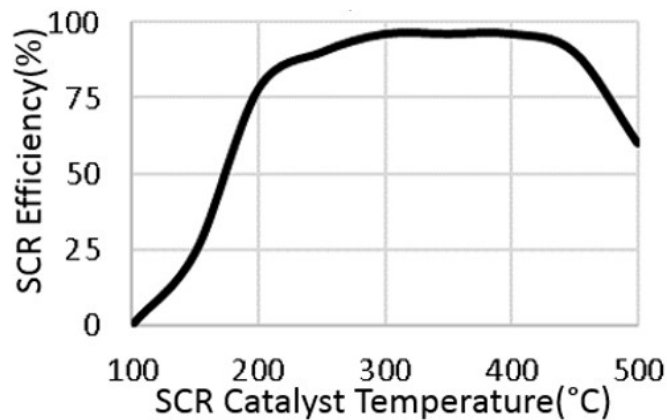


Figure 2.1. An example SCR conversion efficiency curve, where the ability of the SCR to convert NO_x is a function catalyst bed temperature.

Based on the 8-mode time-based fuel analysis of the HD-FTP shown in Figure 2.2, 43% of the 20 minute HD-FTP is spent at idle (800 RPM/1.3 bar BMEP). This

indicates that a sizable portion of the HD-FTP has both low exhaust temperatures and flow rates, neither of which are conducive to a quick warm-up of the SCR.

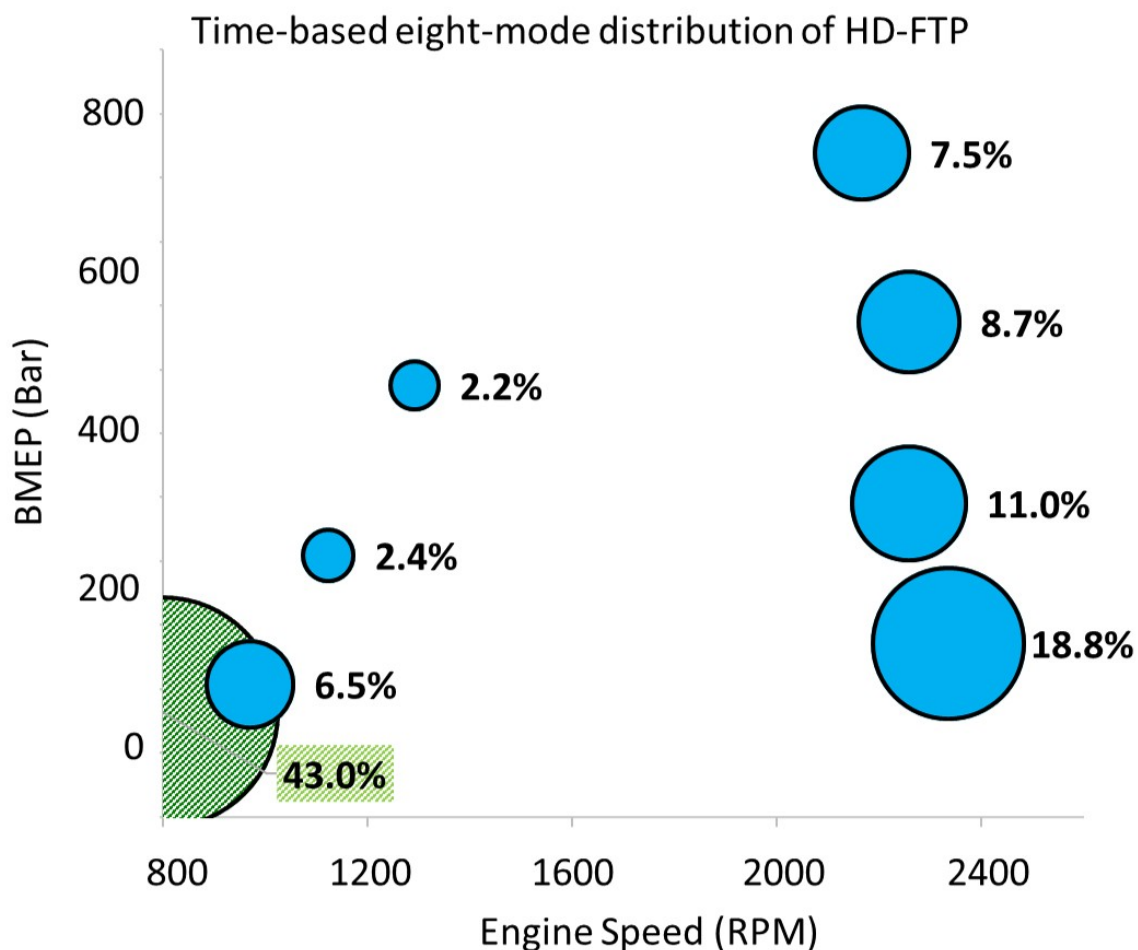


Figure 2.2. Analysis of the percentage of time spent within 8 different regions of the HD-FTP.

At the idle condition, conventional fuel efficient 6 cylinder operation has an engine-out, also known as turbine-out, temperature (TOT) of 145°C, while the state-of-the-art thermal management mode has temperatures of 255°C. An increase in idle TOT, with minimum impact to fuel consumption is ideal for SCR warm-up.

Based on a First Law of Thermodynamics analysis, to enable higher TOTs there are two options: 1) reduce engine efficiency to allow more fuel flow (reduced AFR), 2)

reduce other engine heat losses to increase the amount of energy in the exhaust. Two air handling strategies are proposed and tested in this chapter, iEGR and EEVO, the former which uses a combination of the two options and the latter which relies on just the first option. Previous work described in Section 1.2.2 showed merit to both strategies for increasing TOT at idle.

The valve and fuel injection operations for all four strategies are shown in Figure 2.3: a) 6 cylinder “Fuel Economy” baseline, b) 6 cylinder “Thermal Management (TM)” baseline, c) early exhaust valve opening (EEVO), and d) internal EGR (iEGR). The TM baseline is the industry standard for increasing aftertreatment component temperatures, a “get warm” strategy, currently used by Cummins on the ISB engine platform. The goal of this work was to determine a variable valve actuation enabled strategy which warms up the aftertreatment faster, allowing for the SCR to reach peak NOx conversion efficiency, with the lowest impact on fuel consumption.

The EEVO case involves utilizing the TM baseline injection strategy and opening the exhaust valves an undisclosed amount early. This point was found through screening of exhaust valve opening timing until a peak TOT was found which had stable combustion. Moving the exhaust valve timing any earlier resulted in incomplete and unstable combustion, as was detailed by a shifting and unstable heat release rate. Engine-out NOx and AFR was controlled via modulation of the external EGR valve.

Exhaust gas is trapped in the cylinder with the iEGR case by phasing both the exhaust and intake valves away from TDC (EEVO and EEVC). This allows for combustion byproducts to be trapped in the cylinder and re-combusted with fresh air during the next combustion event. Since exhaust gas is recirculated internally in this manner, the external EGR loop is closed. Closing the external EGR loop prevents heat loss to the coolant through the EGR cooler. Additional dilution is required to maintain engine-out NOx since internal EGR is not cooled. This results in lower AFRs, higher engine-out temperatures, and reduced exhaust flow rates. The two different AFRs shown in the next section are achieved by modulating the amount of combustion byproducts evacuated from the cylinder.

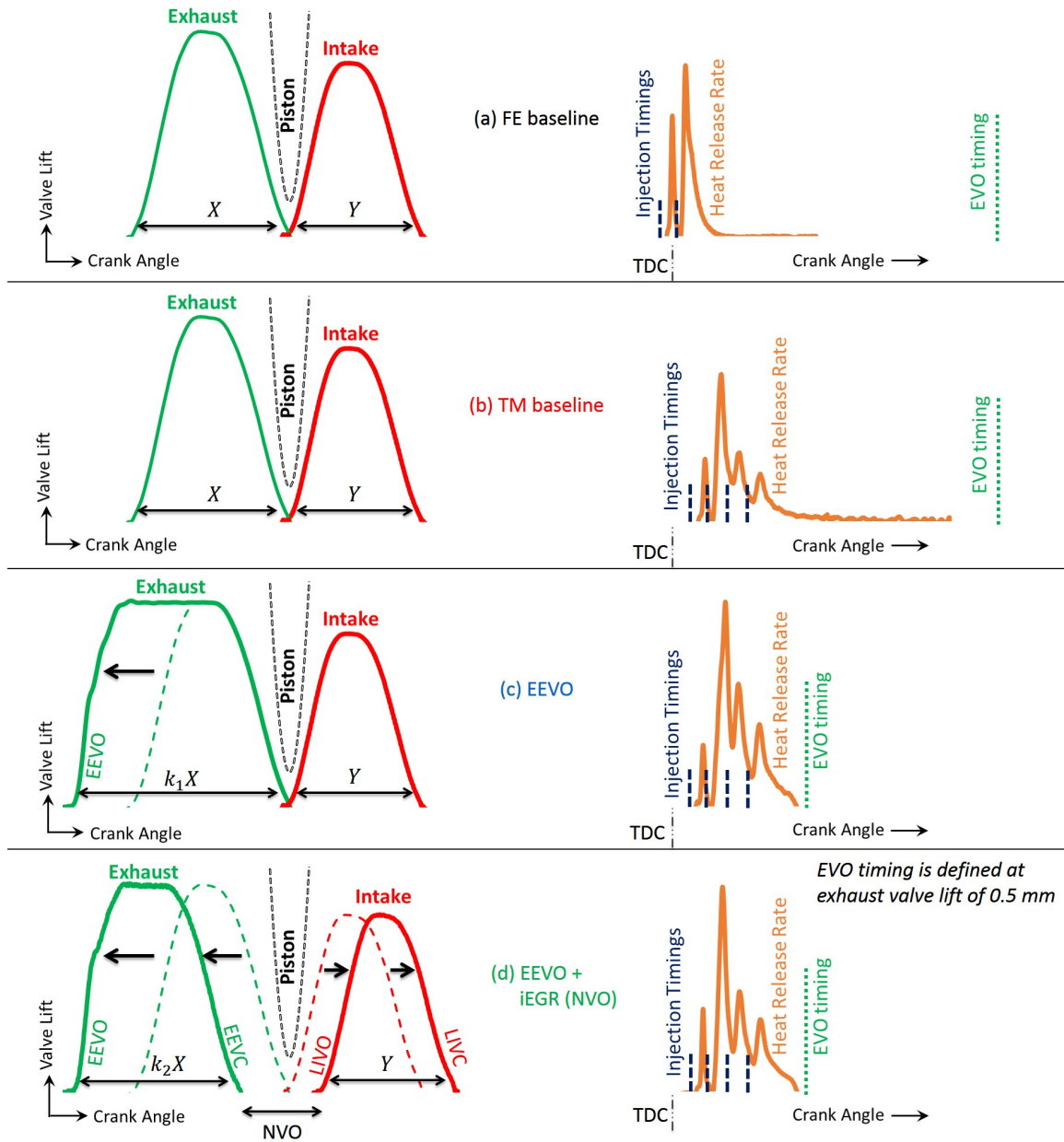


Figure 2.3. The 6 cylinder fuel economy (FE) baseline uses 2 injections, while thermal management (TM) mode uses 4 late injections; both EEVO and iEGR utilize valvetrain flexibility with the 4 late injections of thermal management mode.

2.2 Strategy Descriptions and Steady-State Results at Loaded Idle

Steady-state results were found at an engine condition of 800 RPM and 1.3 bar BMEP, which emulates a loaded idle scenario where the vehicle is in gear but the driver’s foot is on the brake, such as at a stop light. This steady-state condition is relevant because as was mentioned in Section 2.1, 43.0% of the HD-FTP is spent at this condition. The impact of the four strategies, FE baseline, 6 cylinder TM baseline, EEVO, and iEGR, on the LogP-LogV diagram is shown in Figure 2.4. The three thermal management strategies reduce the pressure and temperature at which combustion happens relative to the FE baseline, which in turn reduces CCE, allowing for additional fuel energy to be added to maintain a given engine power output.

The three efficiencies, OCE, CCE, and ME multiply together to find BTE. This is shown in Equation (2.1). Understanding these four efficiencies helps shed light on the dynamics of the four operational modes, as shown in Figure 2.5, where the efficiencies are normalized off of the industry standard “get warm” TM baseline strategy. Utilizing iEGR exhibits an OCE close to the FE baseline because it does not have an over-squeezed VGT and subsequent high exhaust manifold pressure which is needed to drive external EGR flow. Likewise, the charge dilution with hot exhaust gases in the iEGR scenario results in higher in-cylinder temperatures allowing for more heat transfer to the engine block, and ultimately a lower CCE. Both the EEVO and iEGR cases have lower CCE (30% and 50% for AFRs of 22) than the thermal management baseline, as explained by the LogP-LogV diagram in Figure 2.4. The early exhaust valve events release hot combustion gases before the piston cylinder has completed its power stroke which further reduces CCE. ME is consistent across all strategies, as this is a function of the engine platform itself and not the air handling strategies.

$$BTE = CCE \cdot OCE \cdot ME \quad (2.1)$$

As was expected from previous work, and their lower AFRs (22 or 24), EEVO and iEGR both allowed for increased exhaust temperatures at loaded idle over the TM

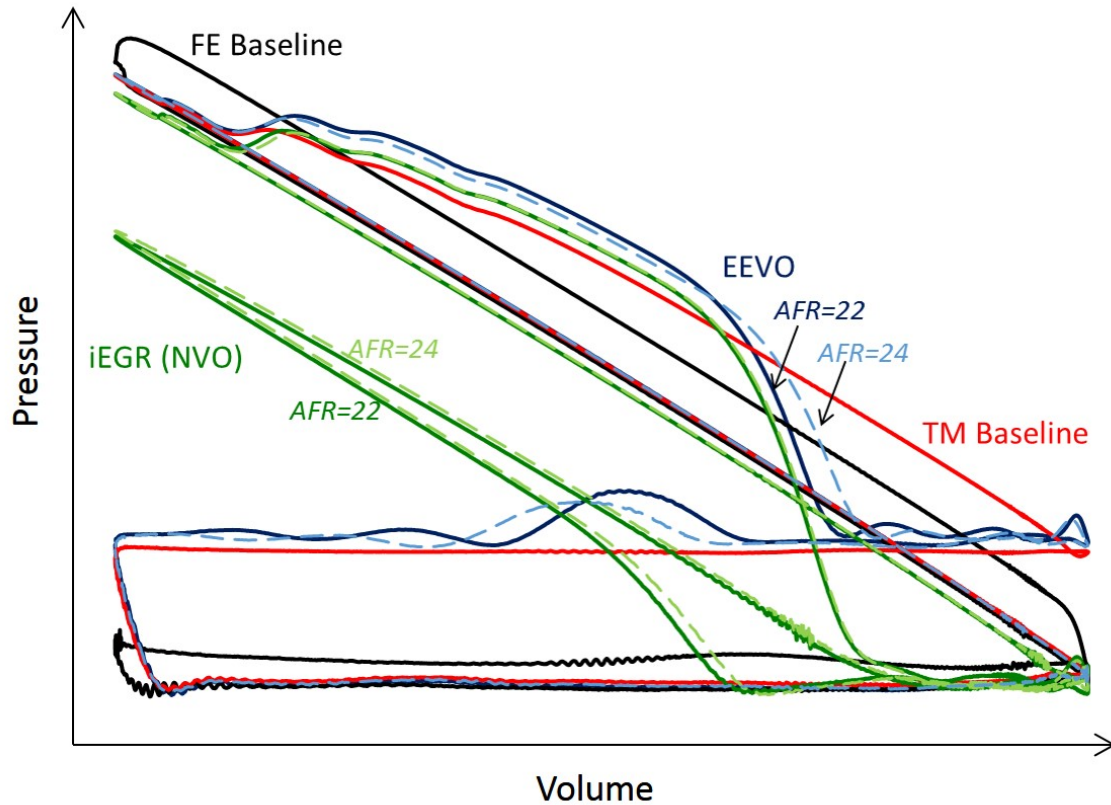


Figure 2.4. Both late injections and valvetrain flexibility manipulate the standard diesel P-V diagram to both decrease engine efficiency and increase exhaust temperatures.

baseline, as shown in Figure 2.6. The FE and TM baselines have AFRs of 40 and 36, respectively. The scenario of iEGR also shows lower exhaust flow than the TM baseline because it requires additional charge dilution to have comparable engine-out NO_x since this EGR is uncooled. Both the EEVO and iEGR strategies require more fuel for the same 1.3 bar BMEP torque output than the TM baseline, as was expected from their decreased BTEs. The additional fuel energy added to the system allows for increased exhaust heat, as calculated by Equation (2.3) and shown in Figure 2.7, which is a 1st Law breakdown of where the fuel energy leaves the system. The other equations used to calculate the values in Figure 2.7 are shown below in Equations

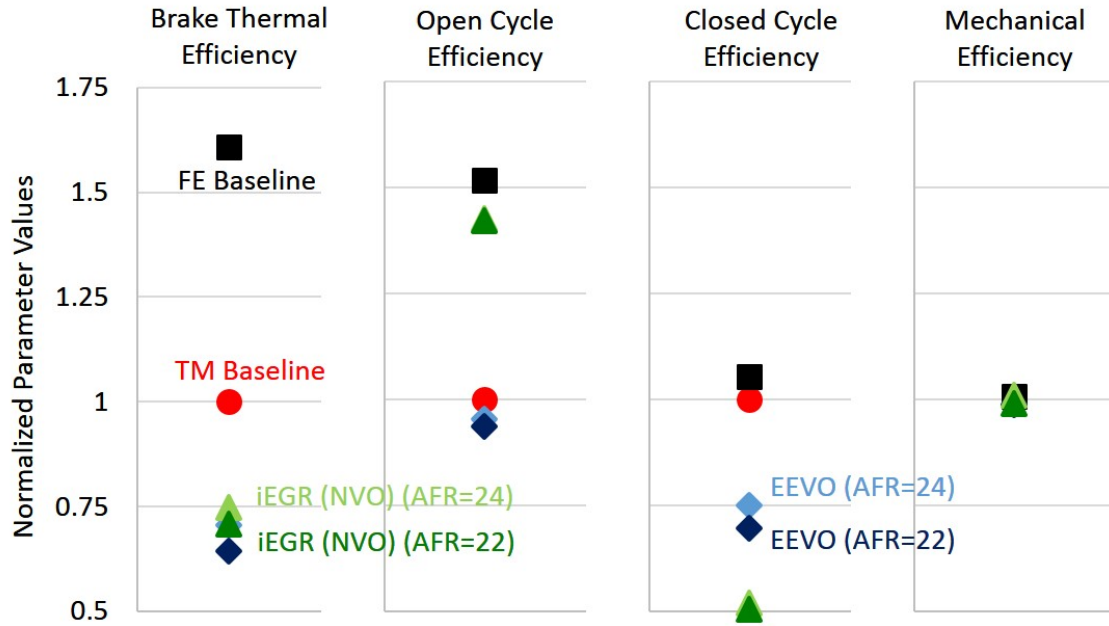


Figure 2.5. Relative to the thermal management mode baseline, both iEGR and EEVO reduce CCE to enable additional fuel energy to the system.

(2.2)-(2.9). The list of variables used in these equations is shown in the Symbols Section at the beginning of this document.

$$\dot{W}_{brake} = T_{brake} \times \frac{2\pi N}{60} \quad (2.2)$$

$$\begin{aligned} \dot{Q}_{exh} = \dot{m}_{exh} \times C_{p,exh} \times (TOT - T_{ref}) \\ - \dot{m}_{air} \times C_{p,air} \times (T_{amb} - T_{ref}) \end{aligned} \quad (2.3)$$

$$\dot{W}_{indicated} = NIMEP \times V_d \times \frac{N}{120} \quad (2.4)$$

$$\dot{W}_{pumping} = PMEP \times V_d \times \frac{N}{120} \quad (2.5)$$

$$\begin{aligned}\dot{Q}_{charge} = & \dot{m}_{charge,out} \times C_{p,charge,out} \times (T_{EM} - T_{ref}) \\ & - \dot{m}_{charge,in} \times C_{p,charge,in} \times (T_{IM} - T_{ref})\end{aligned}\quad (2.6)$$

$$\begin{aligned}\dot{Q}_{cyl} = & \dot{m}_{fuel} \times LHV_{fuel} - \dot{W}_{indicated} \\ & - \dot{W}_{pumping} - \dot{Q}_{charge}\end{aligned}\quad (2.7)$$

$$\dot{Q}_{EGR} = \dot{m}_{EGR} \times C_{p,EGR} \times \Delta T_{EGRcooler}\quad (2.8)$$

$$\begin{aligned}\dot{Q}_{other} = & \dot{m}_{fuel} \times LHV_{fuel} - \dot{W}_{brake} \\ & - \dot{Q}_{cyl} - \dot{Q}_{EGR}\end{aligned}\quad (2.9)$$

Both of the iEGR AFR scenarios have 0 EGR cooler heat loss, as they utilize uncooled, internal EGR for dilution and have a fully closed valve going to the external EGR loop and heat exchanger. The iEGR cases also show the highest in-cylinder heat loss as explained by the trapping and recombustion of already hot exhaust gases. This analysis shows that iEGR allows for the highest amount of exhaust heat rate per unit of fuel consumed, as calculated by multiplying the exhaust mass flow rate by the constant specific heat and temperature of the exhaust gas. The AFR 24 iEGR case has a 34% increase in fuel consumption over the TM baseline, but generates 49% more heat flow through the exhaust which makes it a contender to test at the idle conditions of the HD-FTP. The case of iEGR with an AFR of 22 also generates 49% more exhaust heat, but consumes 42% more fuel at idle.

As shown in Figure 2.8, iEGR with an AFR of 22 has comparable NOx and HC output to the TM baseline, while iEGR with an AFR of 24 has almost 50% more engine-out NOx and HC, making it undesirable as a warm-up strategy. Similarly, iEGR emits 8 and 23 times higher PM than the TM baseline with AFRs of 24 and 22, respectively. The increased mass of the trapped combustion gas in the iEGR case contributes to increased PM. As will be shown later in the drive-cycle results, the increase in PM at loaded idle will result in less pronounced cumulative PM.

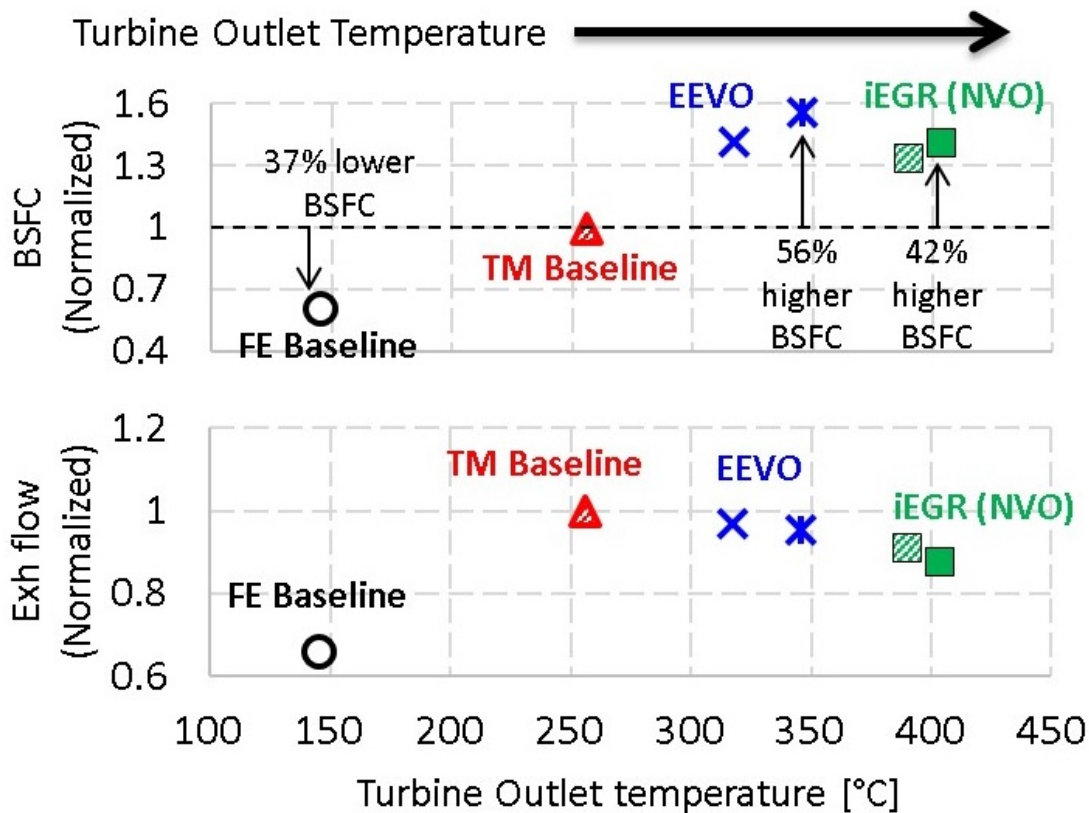


Figure 2.6. Both iEGR and EEVO have elevated exhaust temperatures at idle, relative to the thermal management baseline, with iEGR having the best fuel-to-temperature trade-off.

EEVO allowed for a 20 and 30% reduction in engine-out NO_x for the AFR 24 and 22 cases, respectively. However, both had increased HC in the exhaust, due to the blow-down caused by opening the exhaust valve during the power stroke. The AFR 22 scenario had 12 times higher PM than the TM baseline, while the AFR 24 scenario was 6 times higher.

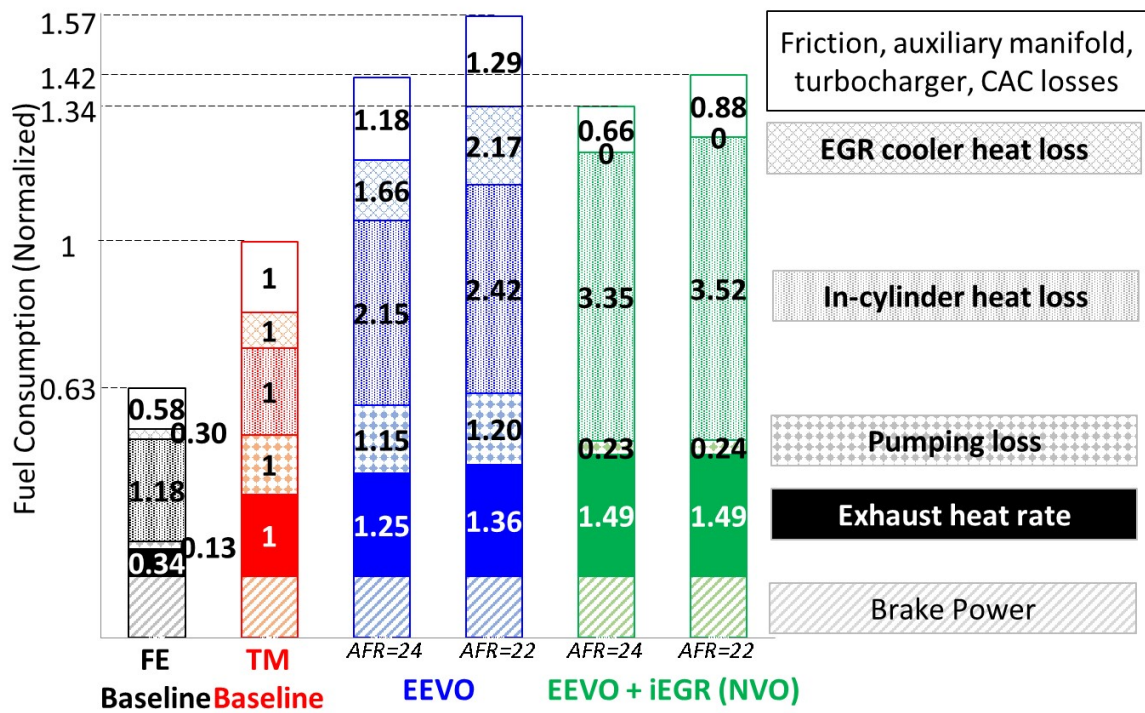


Figure 2.7. iEGR allowed for the highest exhaust heat rate by both reducing EGR cooler loss to 0 (no external EGR) and reducing pumping losses.

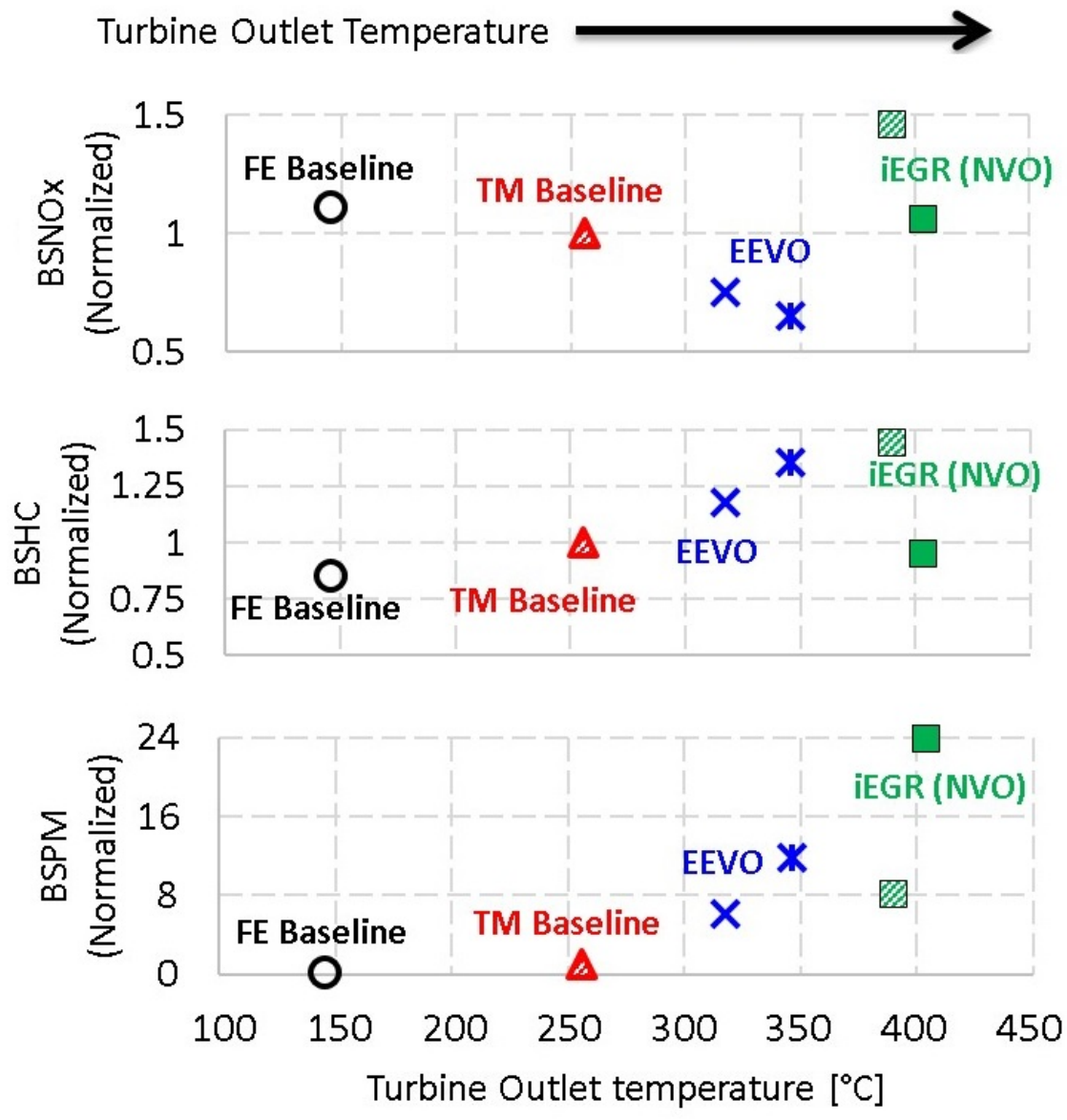


Figure 2.8. The lower AFR iEGR method (dark green, 22AFR) has comparable engine-out NOx and HC as the thermal management baseline, but produces more PM than the higher AFR iEGR method (light green, 24AFR).

2.3 Strategies Applied to Idle Portions of the HD-FTP

As was previously mentioned, 43% of the 20 minute HD-FTP is spent at idle. The idle areas of the cold start and hot start HD-FTPs are shown in Figure 2.9. After the 600 second mark of the hot start HD-FTP, the SCR is routinely at peak efficient NO_x conversion temperatures no matter the strategy applied, so the engine is instead run in the more fuel efficient TM mode beyond this point.

Four idle area “get hot” air handling strategies, iEGR and EEVO at AFRs of 22 and 24, were proposed in the previous section, and compared to the state of the art TM baseline. It was shown that iEGR with an AFR of 22 strategy showed the most promise due to i) highest TOT, ii) emissions on par with the TM baseline, and iii) the best exhaust heat flow to fuel trade-off. Therefore the iEGR with an AFR of 22 strategy’s performance is shown here as applied to the idle regions of the HD-FTP.

The three cases tested over the HD-FTP in this section are:

- **FE Baseline:** Best fuel efficient 6 cylinder throughout both HD-FTP cycles
- **TM Baseline:** State of the art Thermal Management 6 cylinder throughout both HD-FTP cycles
- **iEGR with 22 AFR:** TM Baseline at all non-idle sections, iEGR at all idle sections in the cold start and up to 600s in the hot start HD-FTP; TM Baseline applied thereafter

The turbine outlet temperature and SCR outlet temperatures over both the cold and hot start HD-FTPs are shown in Figure 2.10 for the three cases described above. It is assumed that, once the SCR outlet temperature reaches the 250°C mark, the entirety of the SCR catalyst bed is at or above 250°C. Other methods such as using only the SCR inlet temperature or averaging between the inlet and outlet temperatures were considered but it was found that due to the thermal mass of the aftertreatment system the SCR outlet temperature is a good proxy for the catalyst bed.

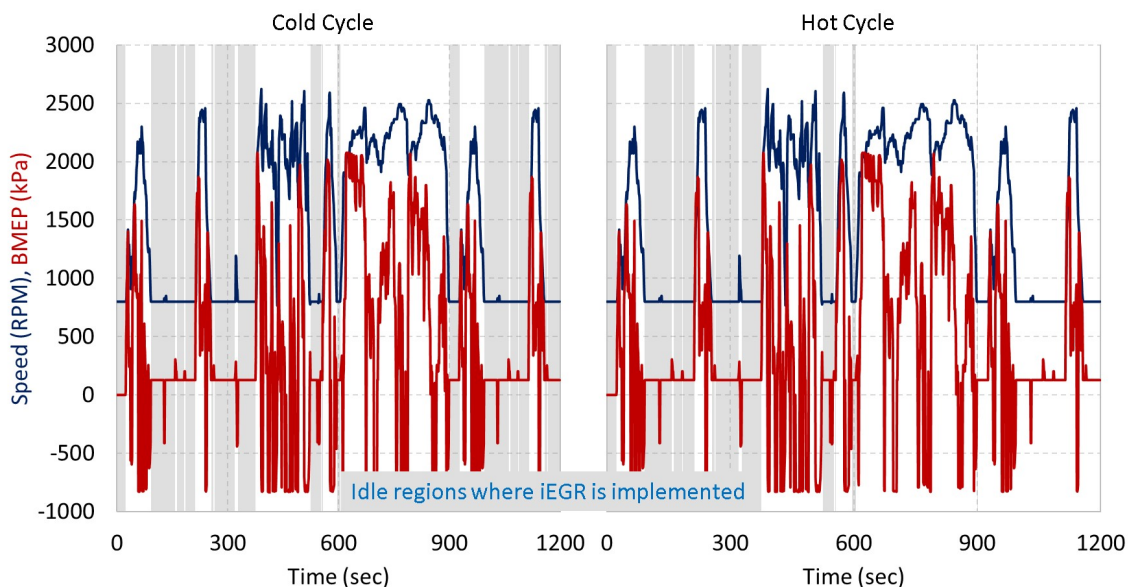


Figure 2.9. The HD-FTP cycle, with candidate iEGR idle application portions highlighted as gray; After 600 seconds into the "hot start" portion, all strategies produce a peak efficiency SCR so instead fuel is conserved.

The FE baseline is the last of the three strategies to reach TOTs sustained above 250°C, with temperatures dipping below the peak NO_x conversion efficiency threshold at the later idle portions of the cold start test. Looking at the SCR outlet temperature, FE baseline has sustained values above 250°C starting around 700 seconds, with TM baseline at 650 seconds, and iEGR with an AFR of 22 meeting the SCR catalyst threshold temperature the fastest at 550 seconds. Temperatures at the SCR outlet all cool off over the 20 minute hot soak, but then quickly rise again at around the 100 second mark before falling again. This is due to latent heat in the aftertreatment system being carried downstream by the cooler exhaust temperatures as shown by the TOTs which start off around 125°C for all cases. The AFR 22 iEGR case shows consistently higher SCR outlet temperatures throughout the hot start HD-FTP, until the 600 second mark where the TM baseline calibration is applied for the remainder of the test and the two strategies, shown by green and red lines, converge.

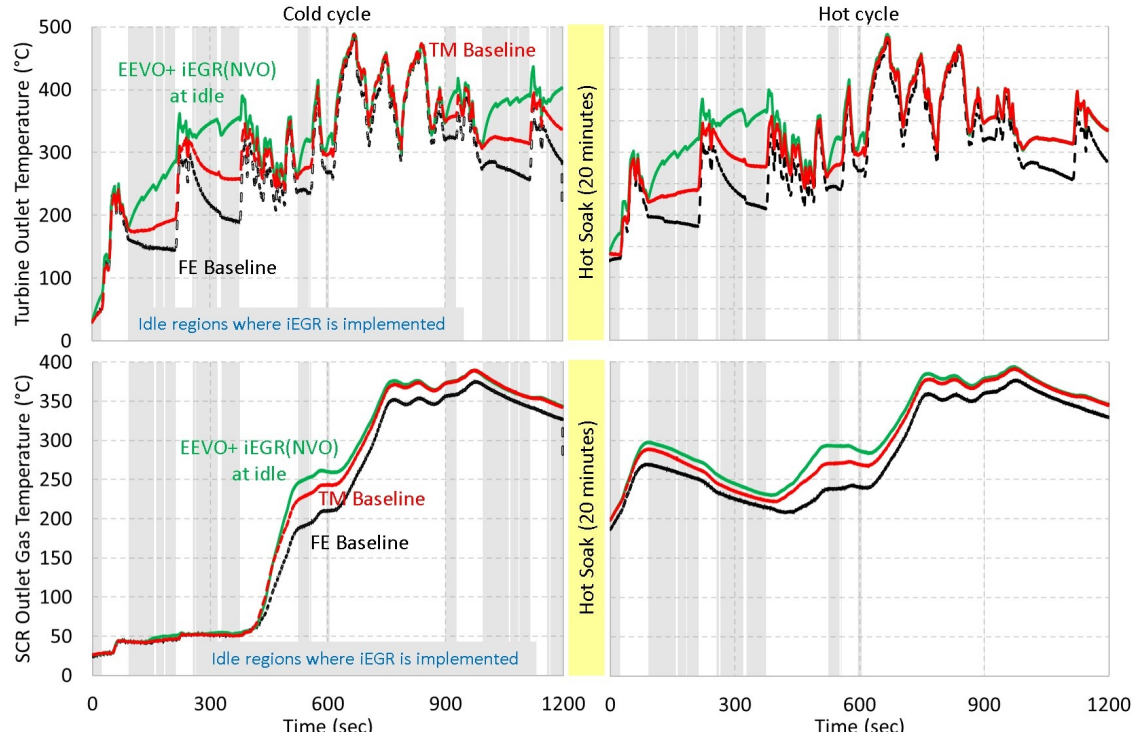


Figure 2.10. iEGR enables SCR outlet temperatures above 250°C faster than the thermal management baseline; after 600 seconds into the hot start, SCR outlet temperatures remain above 250°C , so iEGR is disabled and conventional thermal management operation is enabled.

The SCR NO_x conversion efficiency throughout the HD-FTP is predicted using an SCR efficiency curve provided by Eaton, as described earlier in Experimental Set-up, Section 1.3.1. The model prediction for SCR conversion efficiency is shown in Figure 2.11. The iEGR case reaches 90% efficiency the fastest, followed by TM baseline, and FE baseline. The air handling strategy of iEGR with an AFR of 22 during the idle sections of the cold start HD-FTP allowed for peak SCR NO_x conversion efficiency 100 seconds faster than the TM baseline. Throughout the hot start HD-FTP, iEGR at idle allowed for the highest SCR NO_x conversion efficiency throughout the test, up to the 600 second mark where all three strategies converged.

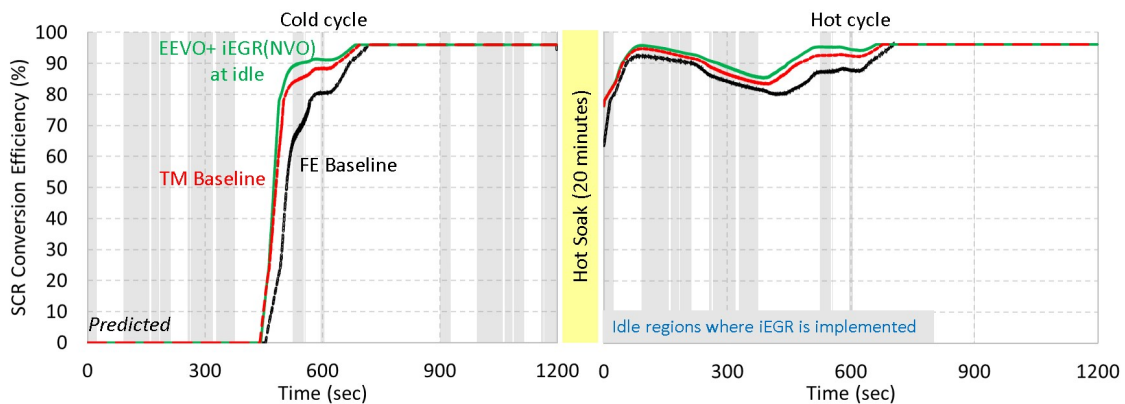


Figure 2.11. iEGR reaches 90% SCR efficiency 100 seconds faster than the thermal management baseline.

Figure 2.12 shows engine-out and predicted tailpipe NO_x overlaid on both the cold and hot start HD-FTP tests. The FE baseline has the highest engine-out and predicted tailpipe NO_x for both the cold and hot starts, the former due to lean combustion (AFR 40) and the latter as a result of lower predicted SCR conversion efficiencies throughout the test. The iEGR air handling strategy produced higher cumulative engine-out NO_x than the TM baseline, but because of consistently higher SCR efficiencies it has the lowest cumulative tailpipe NO_x. Predicted cumulative tailpipe NO_x throughout the hot start HD-FTP is lower than the cold start as a result of the SCR having a high catalyst bed temperature and subsequent high NO_x conversion efficiency throughout the hot start HD-FTP.

Engine-out PM is shown in Figure 2.13. Despite having 12 times higher PM at idle than the TM baseline, iEGR only shows 6.7% higher cumulative PM over the HD-FTP. The impact of high PM at idle is reduced because of the relatively low exhaust flow at idle because cumulative PM is a function of the PM concentration multiplied by the exhaust gas flow rate.

Fuel consumption throughout both the cold and hot start HD-FTPs is shown in Figure 2.14, with values shown as a normalized percent difference relative to the TM

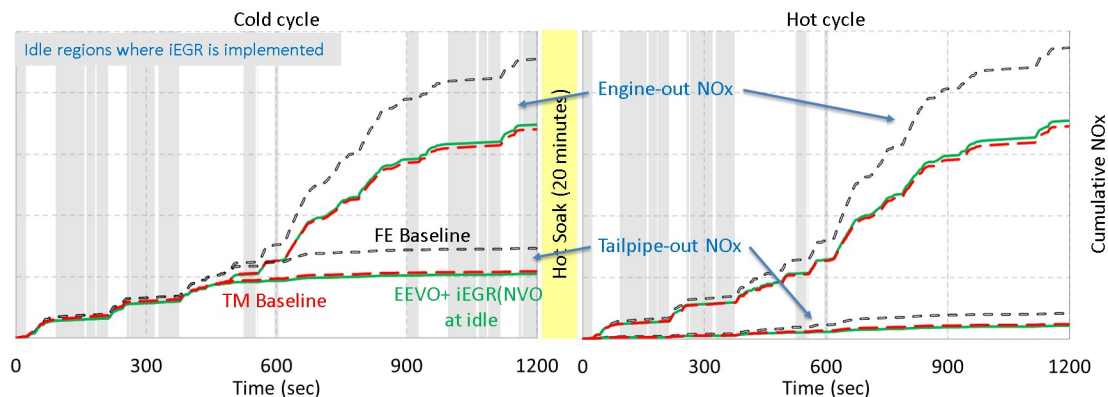


Figure 2.12. FE Baseline has the highest cumulative engine-out and predicted tailpipe NOx, iEGR has higher engine-out NOx than the TM baseline but due to higher SCR conversion efficiencies throughout the HD-FTP it also has the lowest cumulative tailpipe NOx.

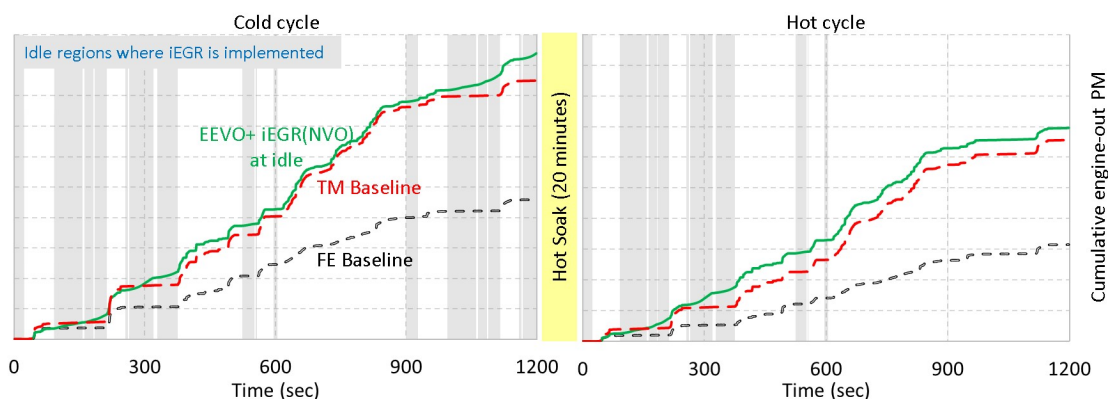


Figure 2.13. Despite having 12 times higher PM than TM baseline at idle, iEGR only has 6.7% higher cumulative PM over the HD-FTP as a result of low exhaust flow rates at idle.

baseline. The iEGR case diverges in fuel consumption from the TM baseline only during idle sections (gray) where iEGR is applied, otherwise the engine operates in the same manner as the TM baseline and therefore has the same fuel consumption. Any divergence at non-idle regions is due to variance in day-to-day engine opera-

tion and repeatability of the fuel consumption measurement system. Relative to the TM baseline, iEGR consumed a weighted average of 2.1% more fuel, with weighting performed per Equations (1.4) and (1.5).

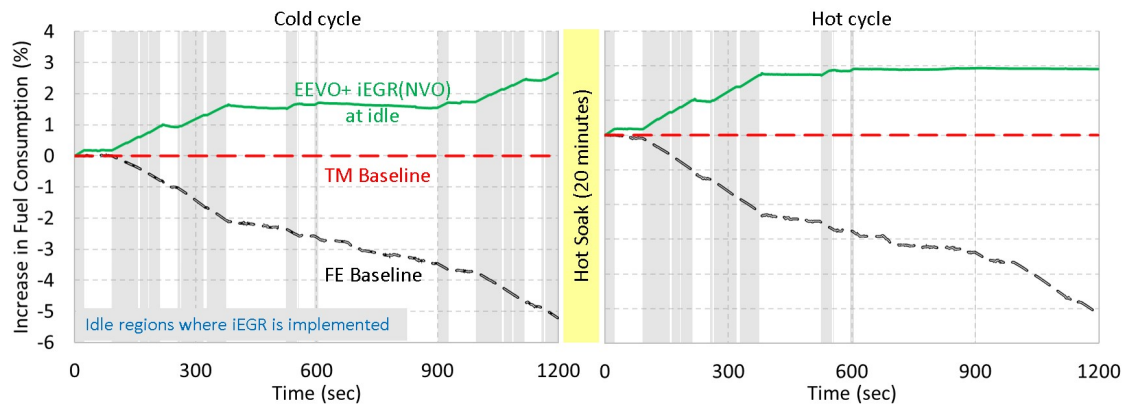


Figure 2.14. iEGR fuel consumption during non-idle periods is equivalent to the thermal management baseline because iEGR is disabled during these sections; variability after 600 seconds into the hot start is due to fuel measurement error and run-to-run variance.

The cumulative predicted tailpipe NO_x versus fuel consumption for all three strategies is shown in Figure 2.15. The TM baseline requires 5.7% more fuel over the FE baseline in order to meet emissions regulations, with iEGR reducing tailpipe NO_x an additional 7.9% with a fuel penalty of 2.1%. In conclusion, iEGR allows for a reduction of tailpipe NO_x that is not achievable with the current state of the art available to engine manufacturers.

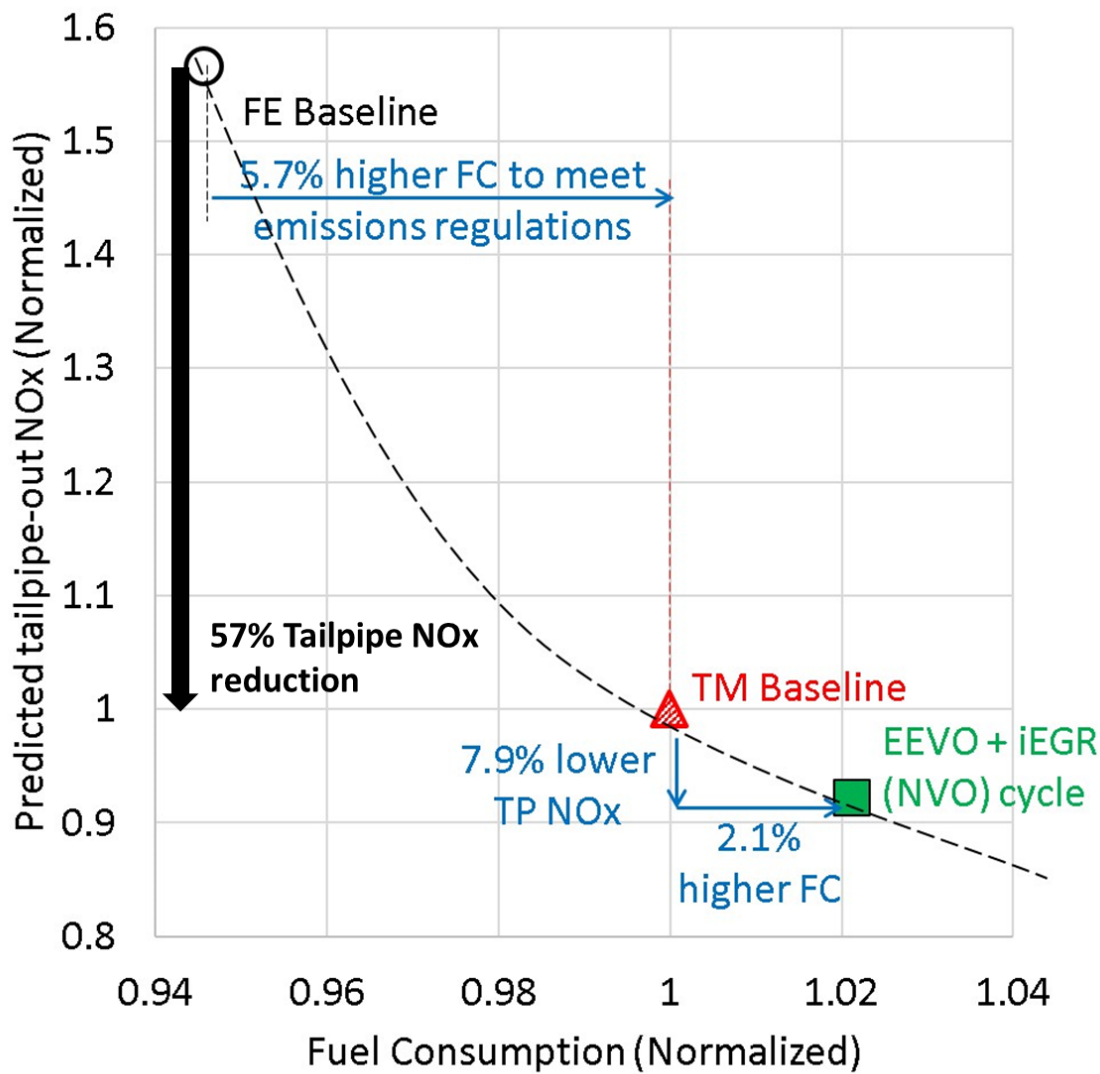


Figure 2.15. With a hypothetical NO_x-Fuel trade-off curve sketched, the marginal reduction in tailpipe NO_x has a higher marginal fuel cost.

3. CYLINDER DEACTIVATION AS AN AIR HANDLING STRATEGY FOR FUEL EFFICIENT & “STAY-WARM” AFTERTREATMENT THERMAL MANAGEMENT

3.1 Motivation

The previous chapter discussed thermal management warm-up strategies, which necessitated burning additional fuel to allow for faster warm-up of the aftertreatment system, namely the SCR. Operating the engine with fewer cylinders reduces the exhaust flow rate, but does provide increased temperatures from the baseline FE strategy albeit lower than those of the TM baseline. CDA is studied here as a stay-warm strategy due to its i) reduced exhaust flow rates and temperatures from the TM baseline eliminating CDA as a potential warm-up strategy and ii) fuel consumption benefits at a loaded idle condition of 800 RPM and 1.3 bar BMEP.

As shown in Figure 3.1, 5.84% of fuel is consumed at idle during the HD-FTP, but 43% of the 20 minute test is spent at idle. The concept studied in this chapter is that CDA could be applied as a fuel efficient air handling strategy once the SCR reaches its threshold temperature of 250°C.

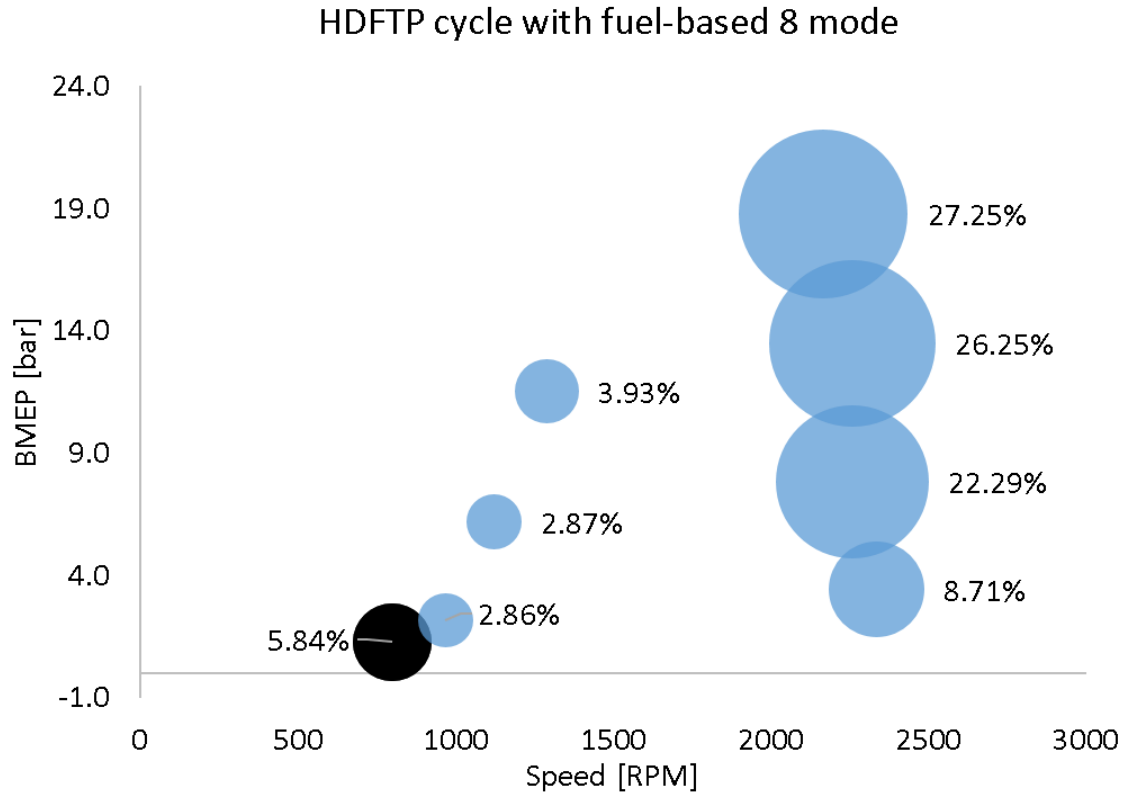


Figure 3.1. An 8-mode analysis of the HD-FTP reveals that while 43% of time is spent at idle, just 5.84% of fuel is consumed there.

3.2 Strategy Description and Steady-State Results at Idle

Before being applied to the transient drive-cycle known as the HD-FTP, the candidate stay-warm air handling strategy of 3-cylinder, also known as half-engine, CDA was studied at a steady-state condition of 800 RPM and 1.3 bar BMEP. As shown in Figure 3.2, half-engine CDA involves cutting fuel to 3 of the 6 cylinders and retracting both the intake and exhaust valves on those same cylinders. This air handling strategy requires roughly double the amount of fuel in the active cylinders to maintain torque at a given speed, while reducing airflow by roughly half. The impact of more fueling per cylinder is a larger heat release rate curve as shown in Figure 3.3.

CDA is compared to the engine's most fuel efficient operating point, 6-cylinder best FE and the current state of the art thermal management modes of 6-cylinder warm-up and 6-cylinder stay-warm. Both of these thermal management modes utilize the same four late injections as shown in Figure 3.3, while half-engine CDA eliminates the last two injections in lieu of a more efficient (from a CCE standpoint) two injection strategy which is described in more detail later.

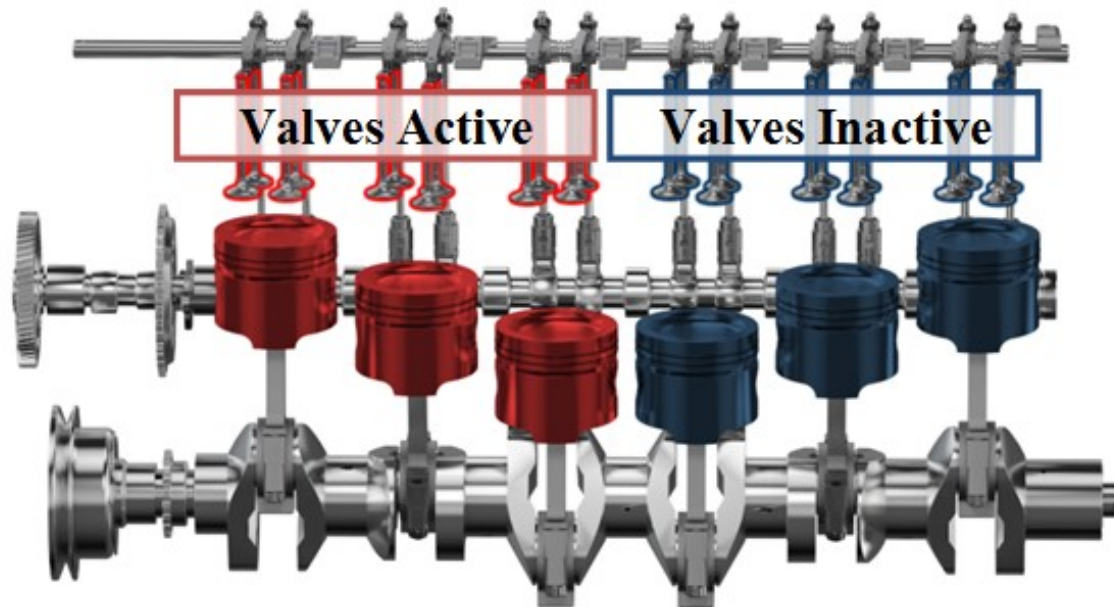


Figure 3.2. Half-Engine CDA, or 3-cylinder CDA, involves both fuel and valve cut to 3 cylinders.

The 6-cylinder warm-up mode has a more oversqueezed VGT to reduce engine efficiencies even further to allow for additional fuel energy to be added to the system to increase TOT. 6-cylinder stay-warm mode relaxes the VGT position to allow for a smaller engine pumping loop as shown in the LogP-LogV plot in Figure 3.4. The 6-cylinder FE baseline's two fuel injections before TDC allow for higher pressure combustion than the other strategies, as shown by the higher peak cylinder pressure. The late (after TDC) injection strategies of both 6-cylinder stay-warm, warm-up and CDA are visible as combustion occurring at lower pressure after TDC was reached

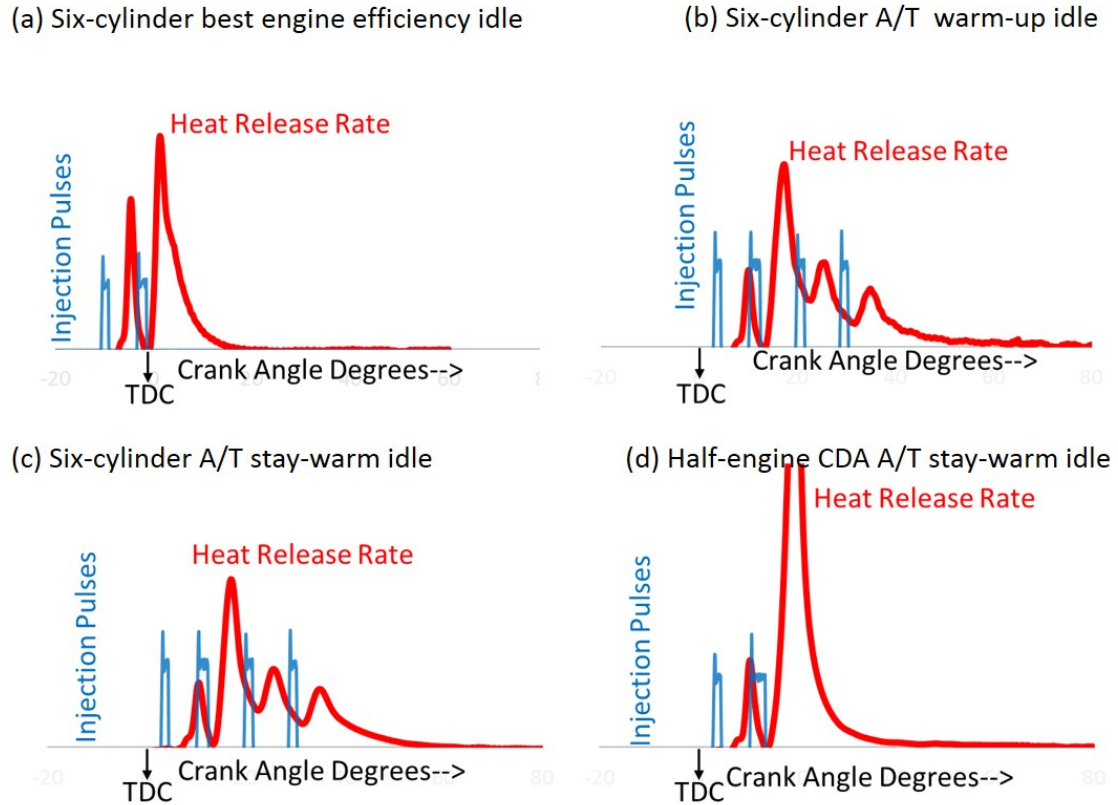


Figure 3.3. The half-engine CDA stay-warm strategy (d) involves two after-TDC injections and shows a larger heat release curve due to the engine load being maintained by just 3 of the 6 cylinders.

in the LogP-LogV diagram, the impact of this on heat transfer to the cylinder walls is discussed later. The reduced airflow of CDA results in a smaller pumping loop than the other three strategies since a smaller mass flow of air is pumped through the engine.

A summary of the four scenarios detailed in Figures 3.3 and 3.4 is below:

- 6-Cylinder Best Engine Efficiency:** The conventional 6-cylinder operation with the best BSFC, utilizing fuel efficient, near TDC injections. Characterized by lower exhaust gas temperatures and a high AFR of 40.

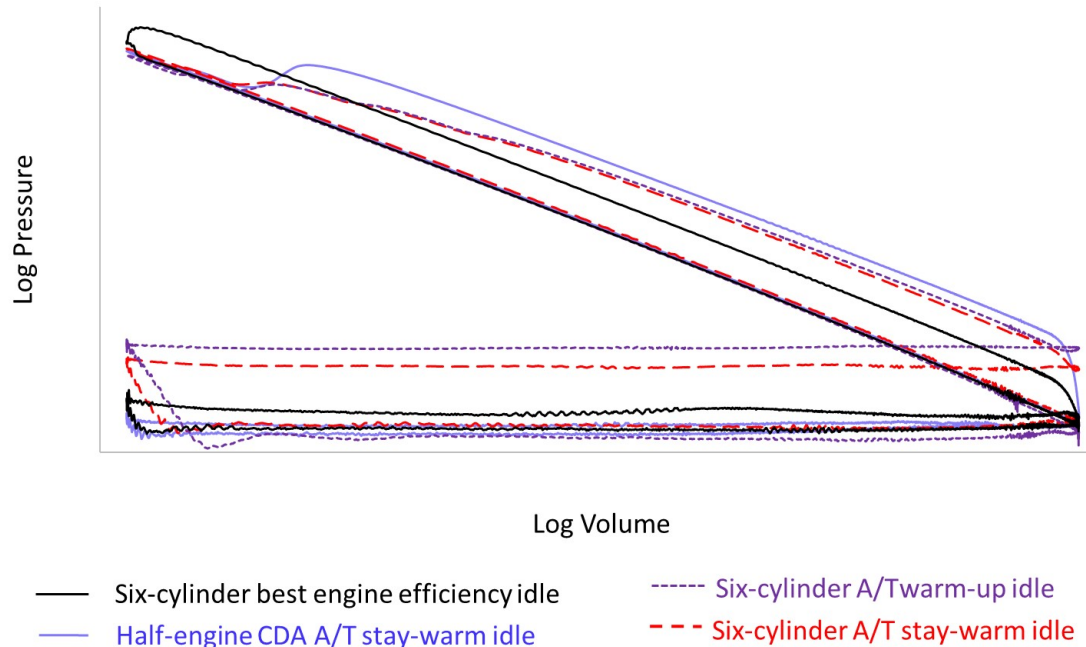


Figure 3.4. All thermal strategies involve lower pressure and temperature combustion modes, enabling higher exhaust temperatures by way of either reduced engine efficiency or in-cylinder heat loss.

- **6-Cylinder Warm-Up** 6-cylinder operation designed to warm-up the aftertreatment system utilizing an over-squeezed VGT and four injections after TDC to reduce fuel efficiency and increase exhaust flow and temperature. This is the state of the art for aftertreatment thermal management, referred to as the TM Baseline in Section 2.2.
- **6-Cylinder Stay-Warm:** 6-cylinder operation which splits the difference between fuel efficiency and elevated exhaust gas temperatures. This strategy implements the same 4 delayed injections as 6-Cylinder Warm-Up, but operates with a more open VGT to reduce the exhaust restriction and improve fuel efficiency by reduced pumping loop. EGR valve and rail pressure are modified to keep NO_x, UHC and PM within bounds of the previous two strategies.

- **Half-Engine CDA Stay-Warm:** 3-cylinder operation with 2 late injections and decreased airflow which results in less parasitic pumping work from the engine. The combination of elevated exhaust temperatures and decreased exhaust flow rates mitigates aftertreatment cool-down.

Figure 3.5 details the efficiencies of the engine, OCE, CCE, ME as calculated in Equations (2.2)-(2.9), and the subsequent fuel consumption at idle. Both 6-cylinder stay-warm and warm-up strategies have the highest exhaust manifold pressures which result in a larger pumping loop and the lowest OCEs. The impact of the reduced airflow of CDA is a higher OCE than the 6-cylinder best efficiency baseline. Mechanical efficiencies are roughly the same for all scenarios, except for CDA where the deactivated 3 cylinders “air spring” work is captured by reduced ME. BTE is a multiplication of OCE, CCE, and ME per Equation (2.1), a lower BTE results in less efficient use of the fuel at a given power output, and thus increased fuel consumption. At loaded idle, 6-cylinder warm-up consumes 60% more fuel than the FE baseline, 6-cylinder stay-warm consumes 40% more fuel, while half-engine CDA consumes 4% less fuel.

The trade-off between fuel consumption, exhaust flow rate and exhaust temperature at idle is shown in Figure 3.5. With FE baseline normalized to 1, 6-cylinder warm-up consumes 60% more fuel but has 120°C higher exhaust temperature and 40% higher exhaust flow, both of which are ideal for aftertreatment warm-up. CDA allows for a 65°C increase in exhaust temperature over the FE baseline, while consuming 4% less fuel. While its temperatures are not as high as 6-cylinder stay-warm at 230°C, CDA consumes 33% less fuel which makes it competitive as a stay-warm strategy.

The emissions for all four strategies are shown in Figure 3.7, with the FE strategy as the baseline. CDA exhibits better NO_x, HC and PM emissions than the FE baseline. This is because the emissions flow rate is a function of both the PPM and the exhaust flow. The late injection strategies of both 6-cylinder warm-up and 6-

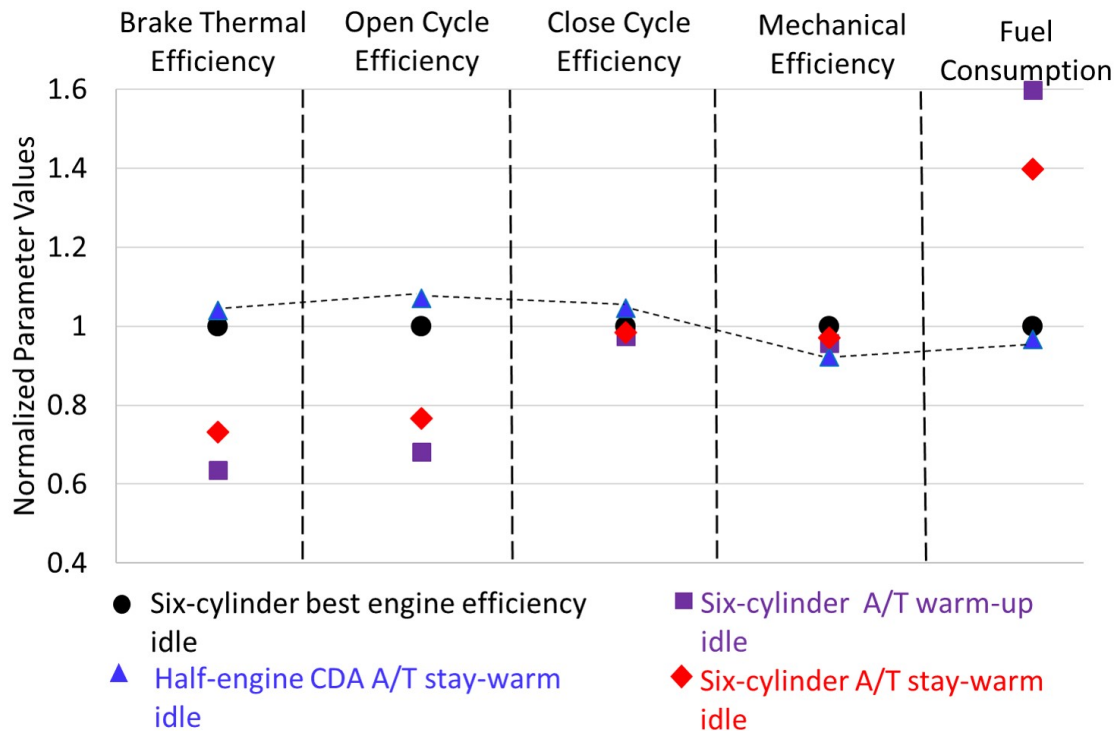


Figure 3.5. With 6-cylinder operation as a baseline, half-engine CDA shows the best BTE and therefore best fuel consumption.

cylinder stay-warm result in higher concentrations of unoxidized carbon in the form of PM. The PM flow rate is exacerbated by the high exhaust flow rate of these strategies.

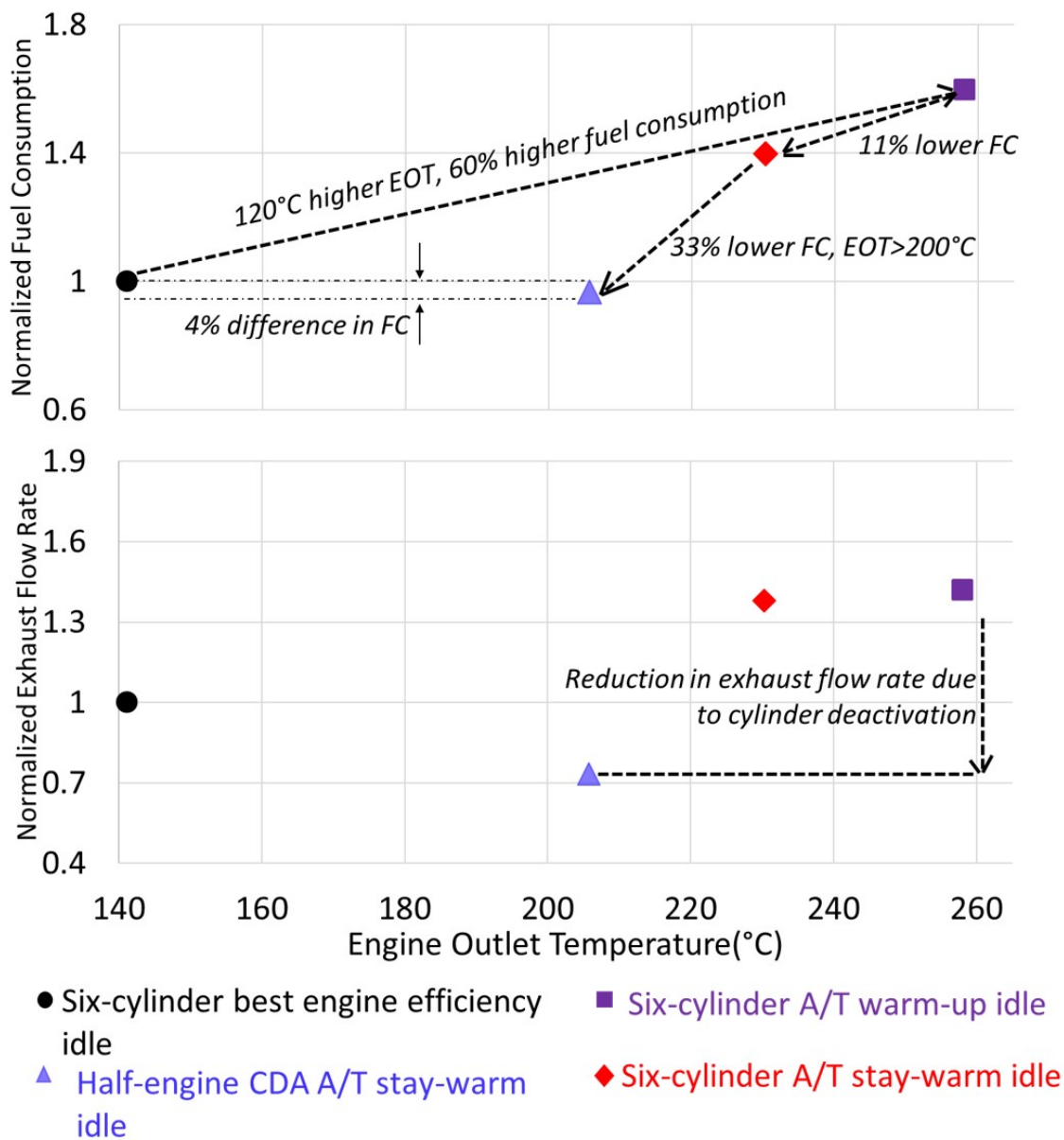
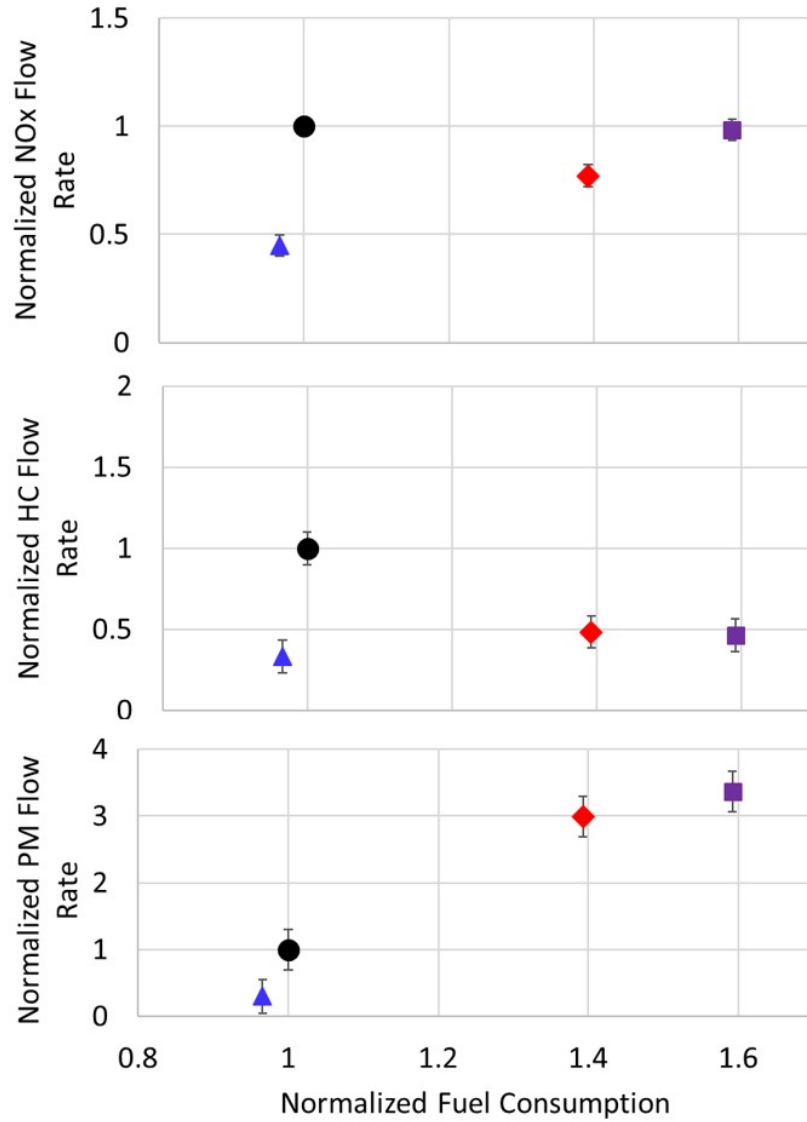


Figure 3.6. As a stay-warm strategy, half-engine CDA allows for 33% reduced fuel consumption over 6-cylinder stay-warm, with temperatures 65°C higher than the 6-cylinder best efficiency point.



- Six-cylinder best engine efficiency idle
- ▲ Half-engine CDA A/T stay-warm idle
- Six-cylinder A/T warm-up idle
- ◆ Six-cylinder A/T stay-warm idle

Figure 3.7. Half-engine CDA has the lowest emissions flow rate (g/hr) while also consuming the least amount of fuel.

3.3 Strategy Applied to both Idle and 0-3 bar BMEP Portions of the HD-FTP

The strategy of CDA at loaded idle showed fuel consumption benefit over 6-cylinder stay-warm as a thermal management stay-warm technique at steady-state idle. The third case studied is CDA applied during the idle regions of the HD-FTP and compared to both the 6-cylinder FE baseline and 6-cylinder thermal management modes. A fourth case is also considered to attempt to gain additional fuel consumption benefit by applying CDA at all idle regions and up to 3 bar BMEP, shown as brown highlights in Figure 3.8. This 0 to 3 bar BMEP CDA strategy also attempts to reduce the cool down of the SCR during engine motoring events, by deactivating cylinders to decrease cool air flow. All cases tested over the HD-FTP drive-cycle use the same 6-cylinder thermal management at non-idle sections of the HD-FTP shown as white in Figure 3.8.

The four strategies tested over the HD-FTP are:

- **6-Cylinder Best Engine Efficiency:** The conventional 6-cylinder operation with the best BSFC, utilizing fuel efficient near TDC injections. Characterized by lower exhaust gas temperatures and a high AFR of 40.
- **6-Cylinder Thermal Management** 6-cylinder operation throughout the drive-cycle utilizing: i) the aforementioned 6-cylinder warm-up idle recipe up to 600s into the hot start and ii) 6-cylinder stay-warm strategy at idle sections thereafter.
- **Half-Engine CDA at Idle** The same operation as above, except that 3-cylinder CDA is implemented at all idle regions after 600s into the hot start HD-FTP
- **Half-Engine CDA 0-3 bar BMEP:** The same as Half-Engine CDA at Idle, except CDA is also implemented during both motoring regions and up to 3 bar BMEP, to further save fuel and reduce the amount of cool air flow to the aftertreatment during engine motoring

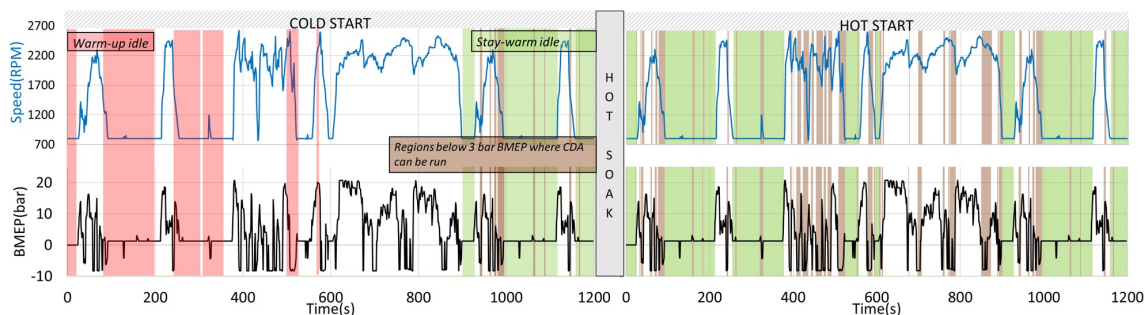


Figure 3.8. The cold and hot start HD-FTP speed and torque profiles shown, with red indicating “warm-up”, green indicating “stay-warm” and brown indicating non-idle portions up to 3 bar BMEP where CDA can be applied.

Detailed in Figure 3.9 are the measured exhaust and SCR outlet temperatures throughout the two HD-FTP drive-cycles. As was explained in Section 1.3.1, SCR outlet temperature is used as a proxy for the catalyst bed temperature. The SCR is modeled as having peak NO_x conversion efficiency at temperatures above 250°C. Throughout both the cold and hot start tests, 6-cylinder FE has the lowest engine exhaust and SCR outlet temperatures as was predicted from the steady-state results. The other three strategies have the same engine calibration at idle up to the 600 second mark and therefore have the same engine outlet and SCR outlet temperatures. During the end of the cold start HD-FTP the divergence in strategies is shown, where CDA at both idle and non-idle portions has the highest engine outlet temperature due to heat retention in the exhaust manifold and turbomachinery because of reduced airflow during motoring sections around the 900 second mark. During these motoring sections, cool air is flowing through the nonfired cylinders and exhaust system, but the cool down effect is reduced by reduction in airflow.

For the entirety of the hot start cycle, CDA at idle/non-idle maintains consistently higher engine outlet temperatures, although all strategies converge during the heavy transient events between 600-700 seconds. SCR outlet temperatures for CDA at

idle/non-idle is the highest throughout the tests after roughly 1000 seconds into the cold start.

Despite the CDA stay-warm idle cycle having comparable engine outlet temperatures to the 6-cylinder TM throughout both the cold and hot tests, the impact of reduced airflow at idle allows for thermal energy stored in the aftertreatment system from previous transients to stay there. This effect on the SCR outlet temperature is noticeable between 100 and 400 seconds in the hot start HD-FTP.

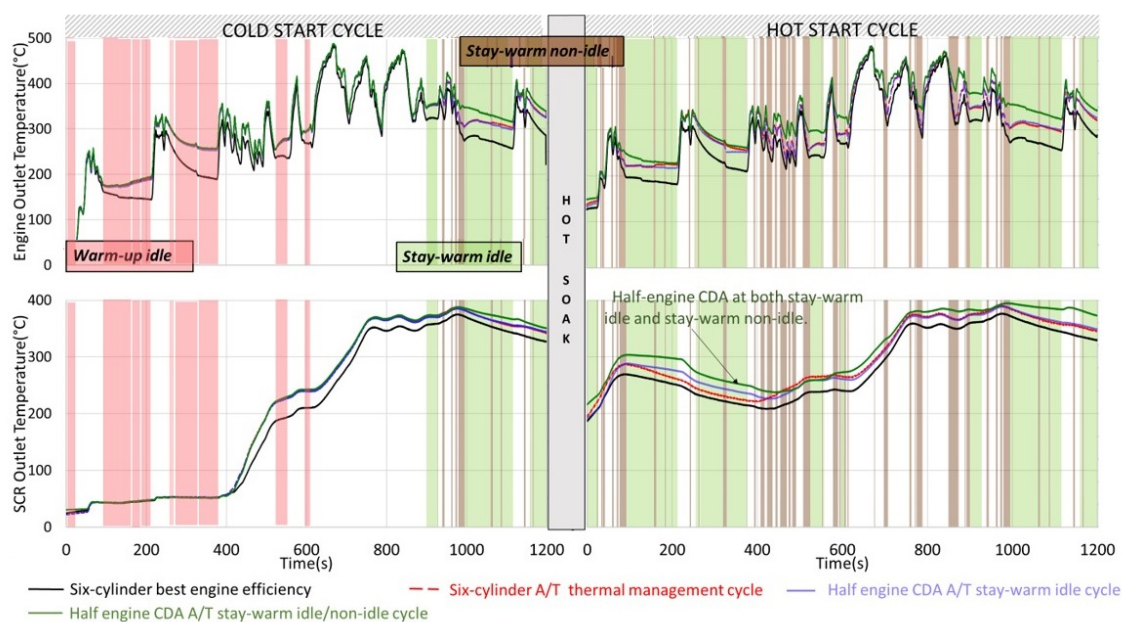


Figure 3.9. Both CDA strategies and the 6-cylinder thermal management cycles utilize 6-cylinder idle operation until the 600s mark of the hot start, after which they utilize their respective strategies.

The measured engine-out NO_x data is overlaid with predicted SCR efficiencies and tailpipe NO_x values in Figure 3.10. The three thermal management strategies reach above 80% efficiency simultaneously at 500 seconds, as would be expected because these strategies all use the same engine calibration up to the 600 second point of the cold start cycle. Beyond the 500 second point of the cold start, model-

predicted tailpipe out NO_x emissions for the TM cases are insensitive to the increased cumulative engine-out NO_x because of the high NO_x conversion efficiency of the SCR. The FE baseline has the same correlation between SCR efficiency and reduced addition to cumulative tailpipe NO_x after the 700 second mark.

Following the 20 minute soak period, the four strategies' predicted SCR efficiencies diverge until around 700 seconds into the hot start cycle. The impact of the air handling strategy of CDA from 0-3 bar BMEP sections is shown at the 100 second mark, as the CDA idle/non-idle cycle has the highest SCR efficiency until 500 seconds into the hot start. All three thermal management strategies end the hot start with comparable predicted cumulative tailpipe NO_x, despite diverging cumulative engine-out NO_x due to sustained high efficiency operation of the SCR.

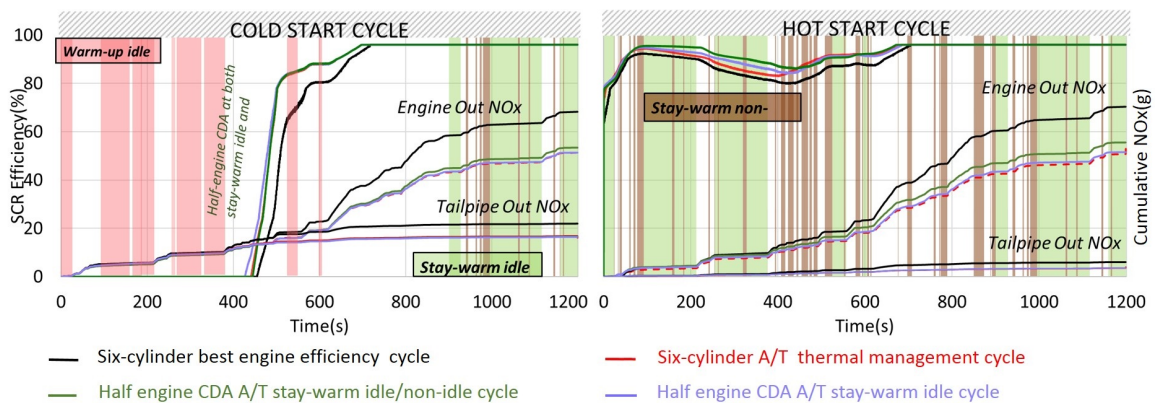


Figure 3.10. Measured engine-out NO_x overlaid with predicted SCR efficiencies and cumulative tailpipe NO_x, all three thermal management strategies have comparable predicted tailpipe NO_x on this scale.

Fuel consumption is shown as a delta from the 6-cylinder thermal management cycle in Figure 3.11. The intent is to detail that while 6-cylinder thermal management mode is necessary over the HD-FTP to meet emissions regulations, there is fuel consumption benefit that could be gained by operating with a different engine calibration or air handling strategy such as CDA. 6-cylinder FE shows the best fuel

consumption benefit over the 6-cylinder TM cycle, but is not a viable option over the HD-FTP due to increased engine-out and tailpipe NO_x. Both the idle CDA and idle/non-idle CDA cycles have no difference in fuel consumption from 6-cylinder TM until the CDA is implemented at idle 900 seconds into the cold start (green region). Any variance in fuel consumption up to the 900 second mark is due to test-to-test variability. The CDA idle/non-idle case ends the hot start with the most favorable delta in fuel consumption due to the additional regions up to 3 bar BMEP where CDA saves fuel over the CDA at idle only cycle.

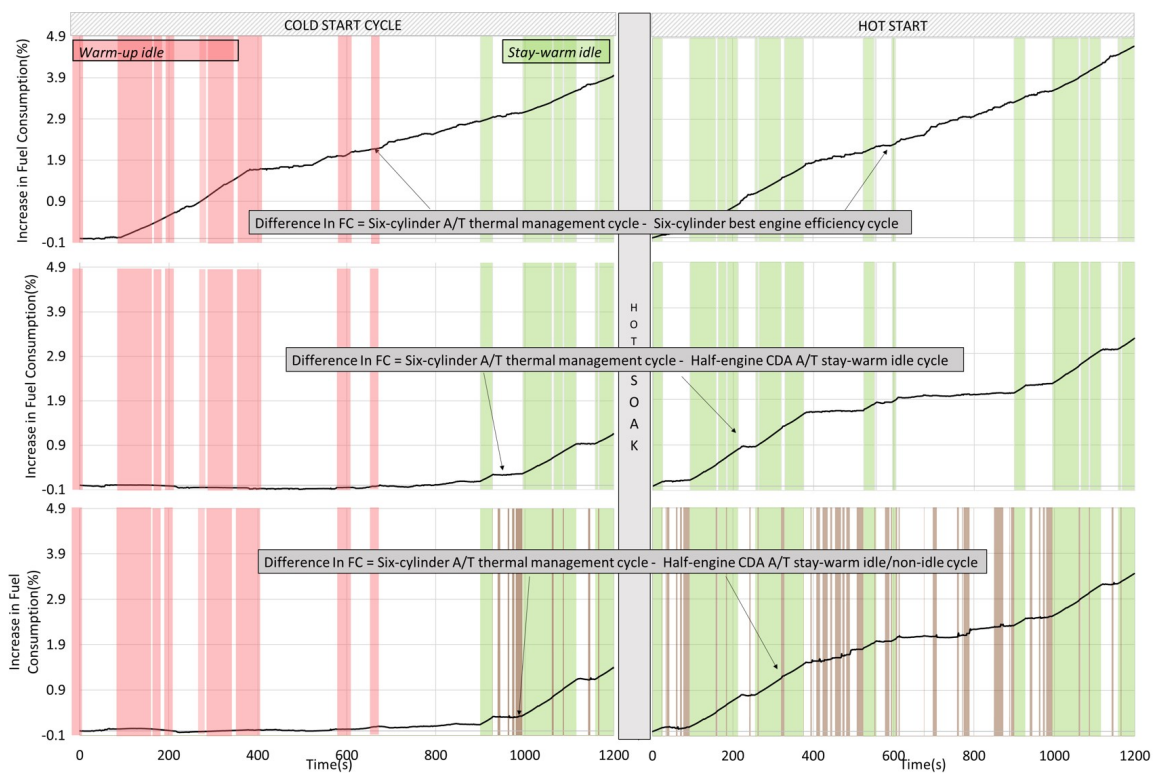


Figure 3.11. A comparison of fuel consumption for the three strategies, relative to the 6-cylinder thermal management mode reveals that 6-cylinder thermal management diverges from half-engine CDA (middle plot) during the idle sections (green areas) as expected.

A summary of the HD-FTP tests performed in this section is shown in Figure 3.12. Both predicted tailpipe NO_x and fuel consumption benefit are normalized to

the 6-cylinder best fuel efficiency cycle. Half-engine CDA applied at idle regions after 600 seconds into the cold start HD-FTP reduced fuel consumption from the thermal management cycle by 3.0%. An additional 0.4% fuel benefit comes from deactivating cylinders at loads up to 3 bar BMEP for a total of 3.4% fuel savings. The strategy of CDA applied from 0 up to 3 bar BMEP is an effective thermal management stay-warm tool, and outperforms the state of the art 6-cylinder thermal management cycle from a fuel consumption standpoint.

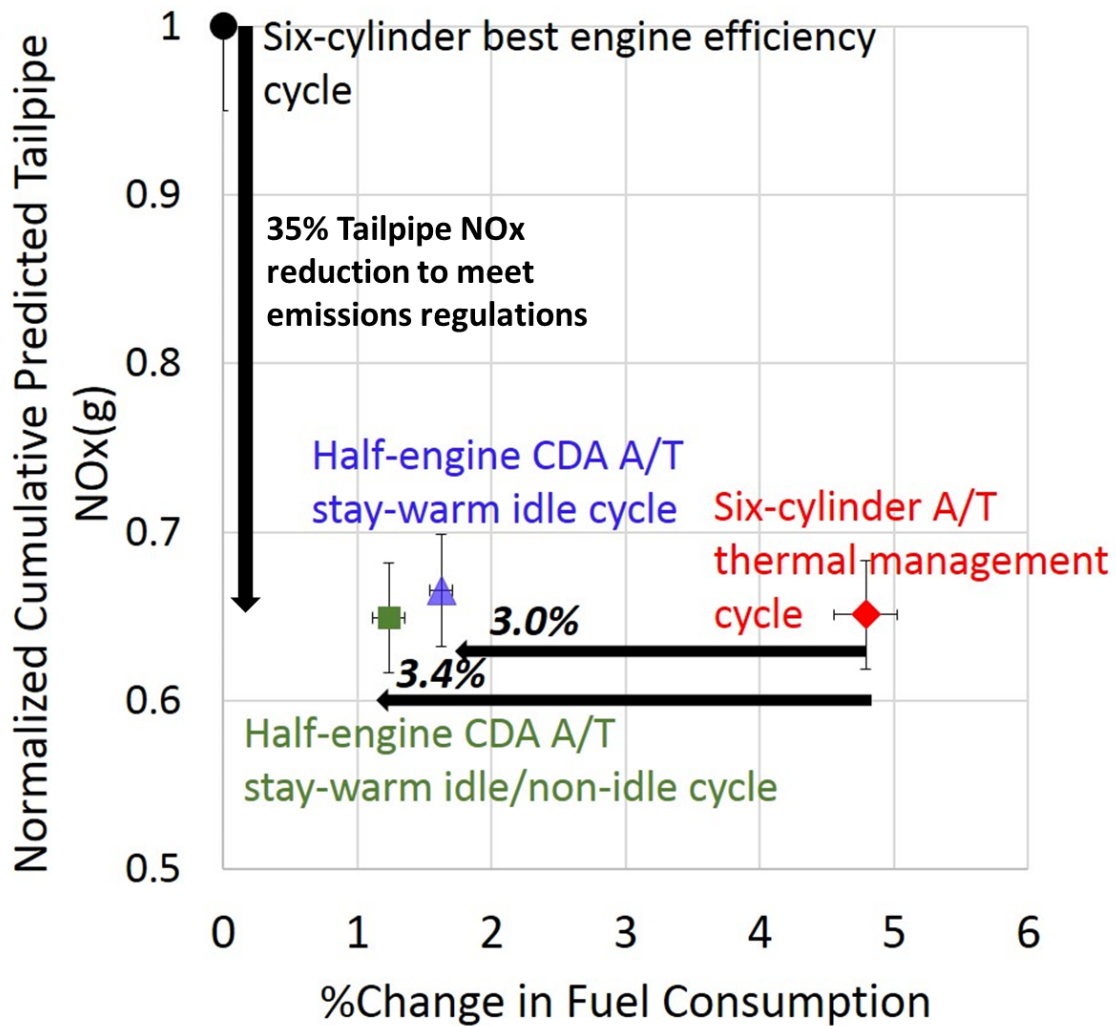


Figure 3.12. HD-FTP Drive-cycle summary, half-engine CDA at idle shifts the NOx-FC trade-off curve to the left, with CDA up to 3 bar BMEP giving an even better benefit.

4. MODEL-BASED COMPRESSOR SURGE AVOIDANCE ALGORITHM FOR IC ENGINES UTILIZING CYLINDER DEACTIVATION DURING MOTORING CONDITIONS

4.1 Motivation

Operating with fewer active cylinders during motoring events reduces the amount of low temperature airflow through the aftertreatment system, improving thermal management. However, compressor surge can result from the sudden subsequent increase in compressor outlet pressure and decrease in compressor flow. As an example, consider the experimental air flow data plotted in Figure 4.1. In this figure, the gray region indicates a motoring section of the drive-cycle, during which 3-cylinder CDA is implemented following high engine load operation. The sudden reduction in displaced cylinder volume resulting from cylinder deactivation results in compressor operation past the surge line as shown in Figure 4.2, whereby compressor flow reverses and oscillates. The compressor shaft speed went from 95,000 to 0 RPM within 0.1 seconds and air flow reversed through the LFE, as shown via the negative airflow at the 774 second mark.

Multiple instances of this deep compressor surge phenomenon damaged the thrust section of the turbomachinery allowing for excessive shaft-play, whereby the compressor wheel could intermittently make contact with the compressor housing resulting in i) increased turbo lag and ii) damage to the oil seal integrity and oil blowby. Continued operation of the turbocharger and interference with the compressor housing likely would have led to catastrophic failure, whereby broken pieces of the compressor wheel could potentially be ingested by the engine. The damaged compressor wheel exhibiting housing contact is shown in Figure 4.3.

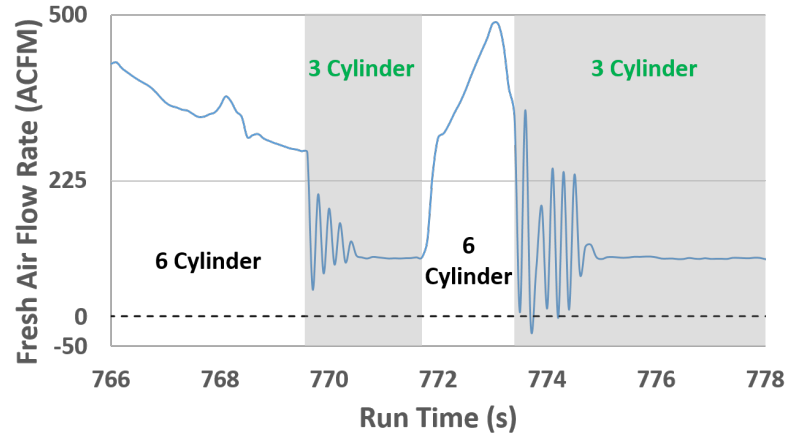


Figure 4.1. Engine airflow measurements over a portion of the HD-FTP detailing negative and oscillatory (surging) airflow after entering 3-cylinder CDA (gray region).

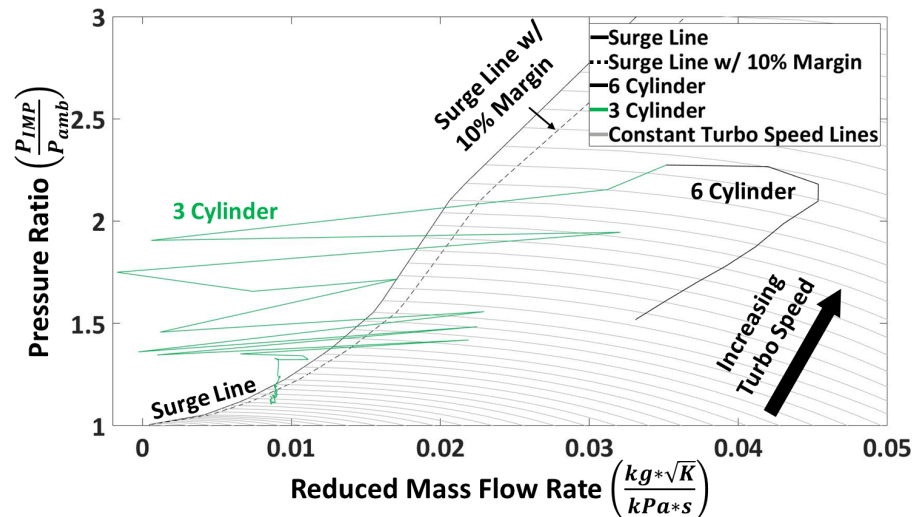


Figure 4.2. The surge data from Fig 4.1 plotted on the compressor map, showing rapid fluctuations in airflow, IMP and turbo speed.

One method to avoid deep decel surge would be to wait a fixed amount of time for IMP to decrease to near atmospheric conditions before transitioning to 3-cylinder CDA. When IMP is at or near atmospheric pressure, there is no favorable pressure delta for surge. A fixed, calibratable delay could work, but would be inherently



Figure 4.3. Intermittent compressor wheel contact with the compressor housing was caught before catastrophic failure of the blades.

conservative, resulting in at least several seconds of unnecessary SCR cooling via full-engine high-speed motoring.

An improved method to avoid unnecessary all-cylinder high-speed motoring, described in detail in the following, would be to deactivate cylinders as soon as it was predicted that surge would be avoided. To accomplish this, three variables require prediction: i) the future IMP increase resulting from the reduction in engine charge flow into the reduced number of active cylinders (Figure 4.4), ii) future engine air flow, and iii) location of the predicted IMP and mass flow relative to the compressor surge line.

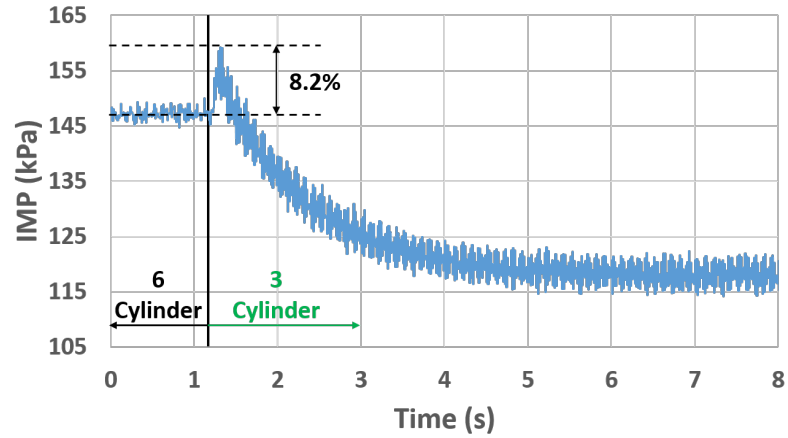


Figure 4.4. An example of IMP increase upon deactivating from 6-Cylinder to 3-Cylinder operation at 1.2s at 2200RPM and 1.27 bar BMEP.

4.2 Methodology

In order to predict the IMP increase triggered by CDA, a physics-based model was developed by invoking conservation of mass on a control volume of the intake tract bounded on one side by the compressor outlet and on the engine-side by the intake portion of the cylinder head. Although the EGR loop is shown in this control volume, EGR flow is always zero during motoring events. This control volume is shown in Figure 4.5, and the conservation of mass equations are shown in Equations (4.1), (4.2), and (4.3).

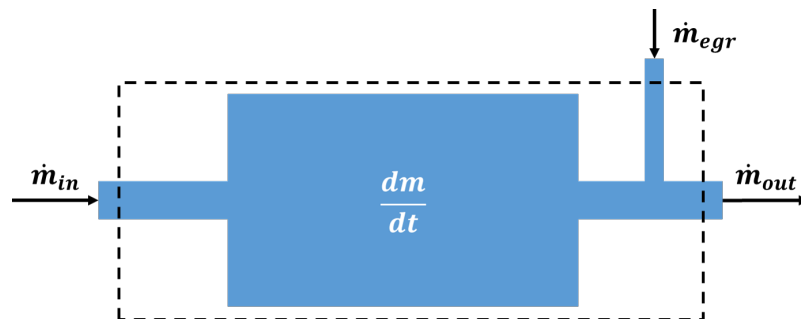


Figure 4.5. Intake tract control volume over which conservation of mass is applied.

Future engine-side mass air flow, \dot{m}_{out} , is predicted using the engine airflow model, given by Equation (4.2), from Ferguson. [59] The future compressor mass air flow, \dot{m}_{in} , is predicted iteratively via the compressor map. With the inputs of turbo speed (assumed constant) and predicted future IMP, the output from the compressor map lookup table is future compressor mass flow. Turbo speed will decrease slightly during motoring events, but is assumed to be constant because this simplifies the model and provides margin by slightly over-predicting the IMP increase. Rearranging the conservation of mass equations, Equations (4.1) and (4.3), a pressure prediction can be made via Equation (4.4). Future compressor outlet pressure is determined iteratively via Equation (4.4) with a 0.1s time step up to 1s into the future.

$$\dot{m}_{in} - \dot{m}_{out} = \frac{dm_{intake}}{dt} \quad (4.1)$$

$$\dot{m}_{out} = \frac{P_i V_{disp} num_{cyl} \eta_{vol} RPM (1 - EGR_{frac})}{120 R T} \quad (4.2)$$

$$\frac{dm_{intake}}{dt} = \frac{P_i V_{intake}}{R T} \quad (4.3)$$

$$P_{i+1} = \frac{\dot{m}_{in} + \frac{P_i V_{intake}}{R T \Delta t}}{\frac{V_{disp} num_{cyl} \eta_{vol} RPM (1 - EGR_{frac})}{120 R T} + \frac{V_{intake}}{R T \Delta t}} \quad (4.4)$$

Future engine mass airflow, \dot{m}_{out} , is predicted using the engine mass flow equation (Equation (4.2)) with the predicted IMP and planned number of activated cylinders. The future predictions of engine air flow and IMP are then plotted on the compressor map, shown in Figure 4.6, and the distance from the surge line is determined via a square root of the sum of the squares. The algorithm follows the logic in the flow chart below, in Figure 4.7.

The IMP increase following the onset of CDA during motoring must be considered because the higher pressure will push the future compressor map location closer to or over the surge line. Assuming that IMP remains constant (no increase) after

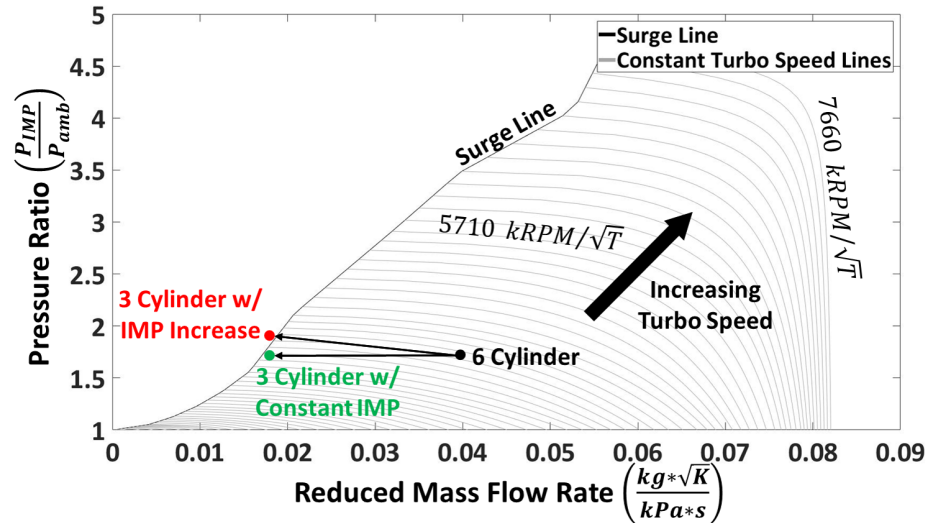


Figure 4.6. Concept: The increase in IMP triggered by deactivating cylinders may push the future location over the surge line, and thus must be considered.

deactivating cylinders does not accurately predict the onset of surge. This is shown in Figure 4.6.

Based on the recommendation of Anderson, et al. a surge margin of 10% was used to account for both the pulsating nature of fresh airflow as a result of the opening and closing of the intake valves. [29] The surge and “margin added” surge lines are shown in Figure 4.8. This figure also illustrates how the proposed algorithm avoids surge. The magnitude of the IMP increase generally scales with the percentage reduction in airflow, thus stepping from 6 active cylinders to 4 active cylinders reduces airflow by 1/3rd, while stepping from 6 to 3 active cylinders reduces airflow by 1/2. Larger stepped reductions in airflow yield a larger IMP increase, which could result in compressor surge.

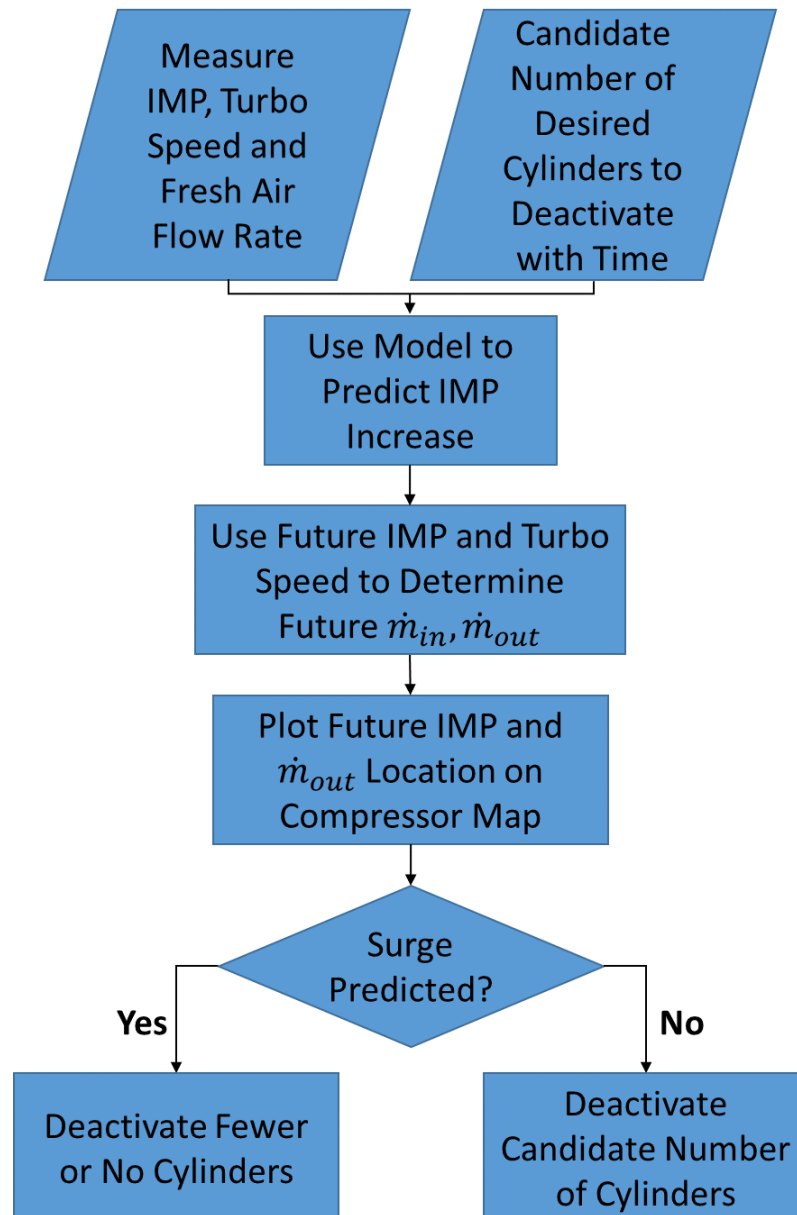


Figure 4.7. The algorithm seeks to deactivate the greatest number of cylinders while avoiding surge.

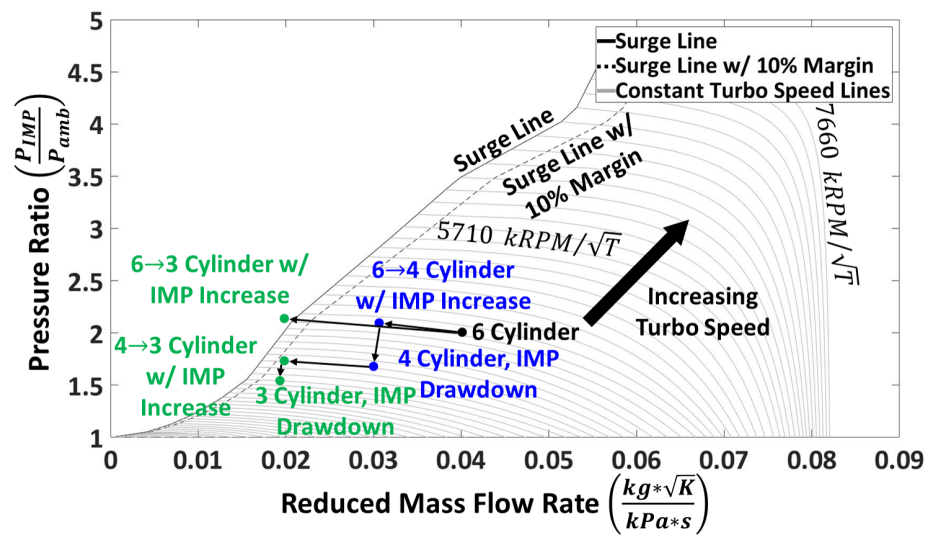


Figure 4.8. Concept: A staged CDA strategy (6-4-3) reduces the magnitude of the IMP increase and avoids decel surge caused by 6 to 3-cylinder CDA.

Table 4.1. Definition and description of variables used in Equations (4.1)- (4.4).

Symbol	Description
\dot{m}_{in}	Mass flow rate of fresh air leaving the compressor
\dot{m}_{out}	Mass flow rate of fresh air entering the engine
$\frac{dm_{intake}}{dt}$	Rate of Change of Intake Manifold Mass
P_i	Intake Manifold Pressure at instant i
V_{disp}	Displacement of the Engine
num_{cyl}	Future Number of Active Cylinders
η_{vol}	Volumetric Efficiency
RPM	Engine Speed
EGR_{frac}	EGR Fraction (0 when motoring)
R	Universal Gas Constant
T	Intake Manifold Temperature
V_{intake}	Volume of the Intake Tract
Δ_t	Change in Time (0.1s)

4.3 Surge Avoidance Algorithm Applied to Transient Results

4.3.1 Model Validation

The IMP increase prediction method was verified using experimental data corresponding to a variety of initial conditions and number of deactivated cylinders. One such case is shown in Figure 4.4, and the model-predicted result is shown in Figure 4.9. The model accurately captures the physics of the IMP increase. After validating the model, it was applied with staged cylinder deactivation to prevent compressor surge in two different cases: i) 1600RPM/25% accelerator position and ii) 2000RPM/71% accelerator position. The former was used to confirm transient application of the algorithm at a lower engine speed and load, and the latter to emulate a section of the HD-FTP where deep decel surge was previously seen (and resulted in the damage shown in Figure 4.3).

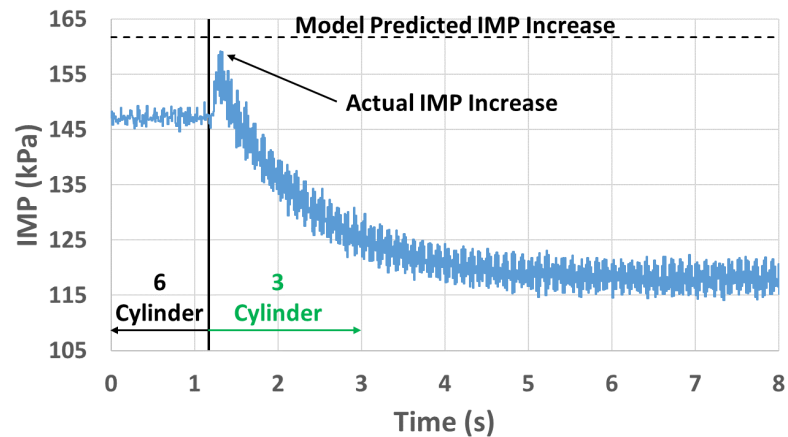


Figure 4.9. The model accurately predicted the IMP increase upon deactivating from 6 to 3 cylinders at 1.2s, which was previously shown in Figure 4.4.

4.3.2 Low Load Results

Transient testing was performed at a condition of 1600 RPM and 25% accelerator position, where the engine is loaded at 0.44 bar BMEP. In this test, accelerator position is held constant at 25% until IMP and engine mass flow (as measured by the LFE) stabilize. At this point, the accelerator position changes to 0% (motoring) and the algorithm is applied to deactivate cylinders and avoid surge as was described in Figure 4.7. Engine speed is held constant throughout the experiment. The measured IMP, fresh airflow, and number of deactivated cylinders are shown in Figures 4.10, 4.11, and 4.12.

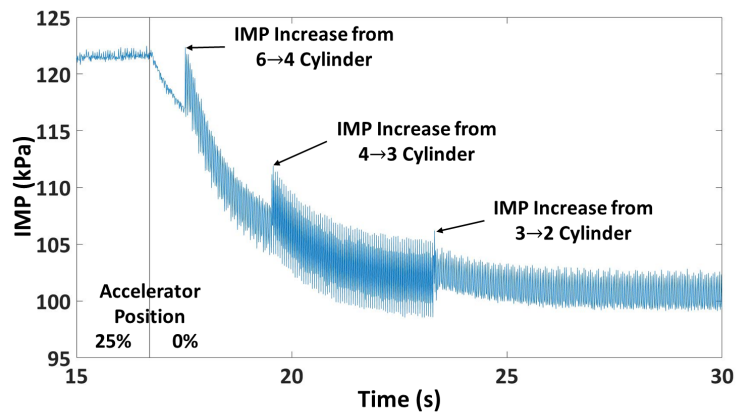


Figure 4.10. Experimental IMP (1600 RPM/0.44 bar BMEP) when accelerator position snaps from 25% to 0%.

Surge is avoided, as desired. The control strategy maintained 6-cylinder operation for roughly 0.5 seconds before transitioning to 4-cylinder operation for about 1 second, then into 3-cylinder operation for 2 seconds. As described previously, the delay in cylinder deactivation, and staging from 6 to 4 to 3 activated cylinders, was necessary to allow for the algorithm-predicted IMP increase to reduce enough to avoid compressor surge.

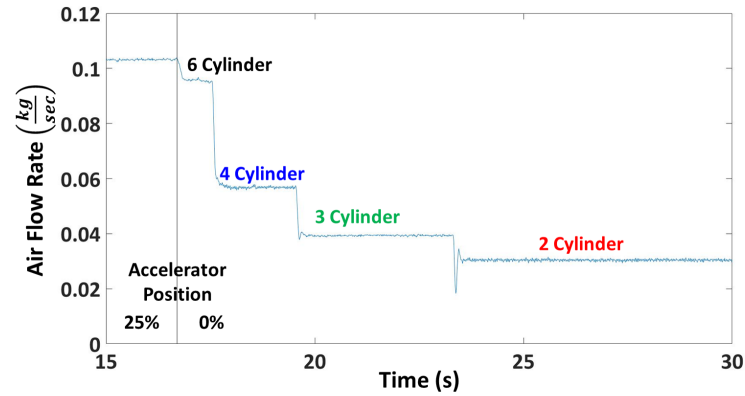


Figure 4.11. Experimental fresh airflow (1600 RPM/0.44 bar BMEP) when accelerator position snaps from 25% to 0%, staged cylinder deactivation reduces airflow and avoids surge.

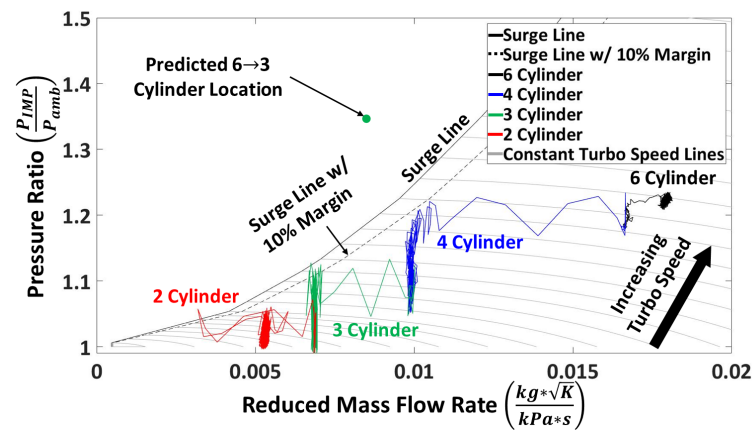


Figure 4.12. Results overlaid on compressor map (1600 RPM/0.44 bar BMEP) when accelerator position snaps from 25% to 0%, staged cylinder deactivation successfully avoids compressor surge.

4.3.3 High Load Results

Transient testing of the developed algorithm was also performed at a condition of 2000 RPM and 71% accelerator position, where the engine is loaded at 13.0 bar BMEP. In this test, accelerator position is held constant at 71% until IMP and engine mass flow (as measured by the LFE) stabilized. At this point, the accelerator

position changes to 0% (motoring) and the algorithm is applied to deactivate cylinders and avoid surge in the same manner as before. This test reproduces a segment of the HD-FTP shown in Figure 4.1 where deep decel surge had damaged the turbocharger previously. The existing data where decel surge occurred and damaged the turbocharger is overlaid on the new data where the surge avoidance algorithm was applied for comparison.

The measured IMP, fresh airflow, and number of deactivated cylinders are shown in Figures 4.13 and 4.14. The model accurately predicted the IMP increase associated with cylinder deactivation, and also held constant the number of active cylinders for the appropriate amount of time to avoid compressor surge. The controller did not allow for deactivation down to the minimum capability of 2 active cylinders because it predicted a location to the left of the surge line at these engine operating conditions.

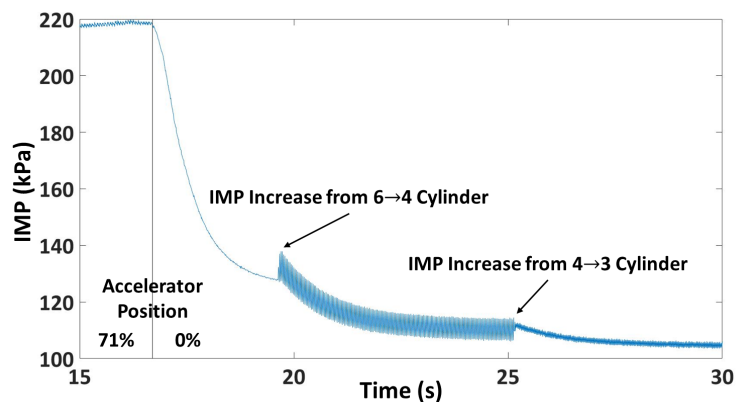


Figure 4.13. Experimental IMP (2000 RPM/13.0 bar BMEP) when accelerator position snaps from 71% to 0%, the future IMP prediction model accurately predicts the IMP increase.

Figure 4.15 shows the surge avoidance algorithm implemented at 2000 RPM and 71 to 0% accelerator position snap overlaid on the compressor map. The algorithm predicted that a transition directly from 6 to 3 active cylinders would have instigated compressor surge as shown in Figures 4.1 and 4.2. The algorithm determined it was necessary to remain in 6-cylinder operation until IMP decreased sufficiently, then it

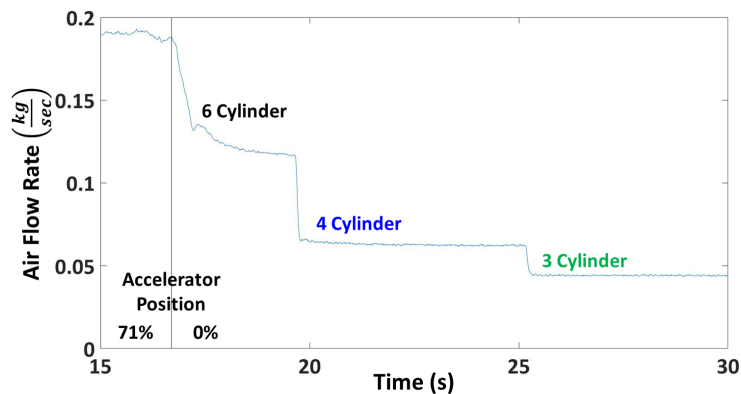


Figure 4.14. Experimental fresh airflow (2000 RPM/13.0 bar BMEP) when accelerator position snaps from 71% to 0%, staged cylinder deactivation reduces airflow while avoiding negative airflow (surge).

switched to 4 cylinders and eventually 3. In this case, 2-cylinder operation was never reached because it would have been to the left of the surge line, albeit at atmospheric pressure. When the intake manifold pressure is at or near ambient pressure, operating to the left of the surge line does not damage the turbocharger due to the lack of a ΔP or reverse airflow across the compressor wheel.

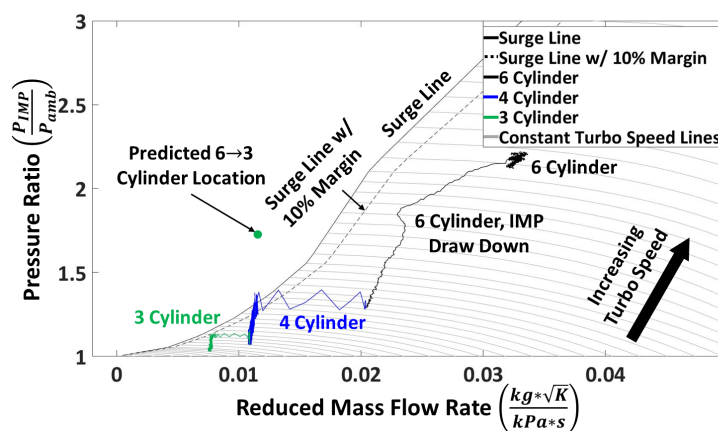


Figure 4.15. Recreating the surge event from Figure 4.2 with the algorithm applied, staged cylinder deactivation was deployed only when surge is not predicted.

The surge avoidance algorithm with staged cylinder deactivation successfully avoided surge during this motoring segment of the HD-FTP, and in so doing allowed for the fastest possible deactivation of cylinders without compromising the turbomachinery.

5. MAKING THE GRADE: THE SENSITIVITY OF CLASS 8 TRUCK FUEL CONSUMPTION & OPERATIONAL BEHAVIOR PREDICTIONS TO ROAD GRADE DATA QUALITY

5.1 Motivation

This work compares road grade for a 5,432 m segment of US 231 near West Lafayette, Indiana obtained by methods i) utilizing a GPS to record horizontal position and vertical elevation, ii) logging the pitch of an IMU, iii) integrating the horizontal and vertical velocities of an IMU, and iv) commercially available grade data (labeled Comm) to grade obtained with a high fidelity LiDAR based system. A statistical regression analysis of road grade from these five sources was performed. A Class 8 truck was simulated driving on the corridor to show the sensitivity of predicted fuel consumption to road grade quality. Simulated vehicle speed and engine torque are also reviewed to determine the sensitivity of predicted vehicle operating characteristics to road grade quality.

5.2 Grade Determination Methods & Example Results for a Specific Corridor

5.2.1 Grade Data Acquisition

Grade data was obtained via five methods for the 5,432 m stretch of southbound US 231 shown in Figure 5.1, through university colleagues (LiDAR), purchase (Comm), and self-acquired (GPS, $IMU_{Int.Vel}$, and IMU_{Pitch}). Table 5.1 summarizes each method. The LiDAR road grade was provided by colleagues in Purdue's Civil Engineering over a 5,432 m stretch of US 231, with a published elevation accuracy

of ≤ 1.42 cm of the true road surface, over 10 m intervals, using a LiDAR system informed by RTK (real-time kinematic positioning). [60].

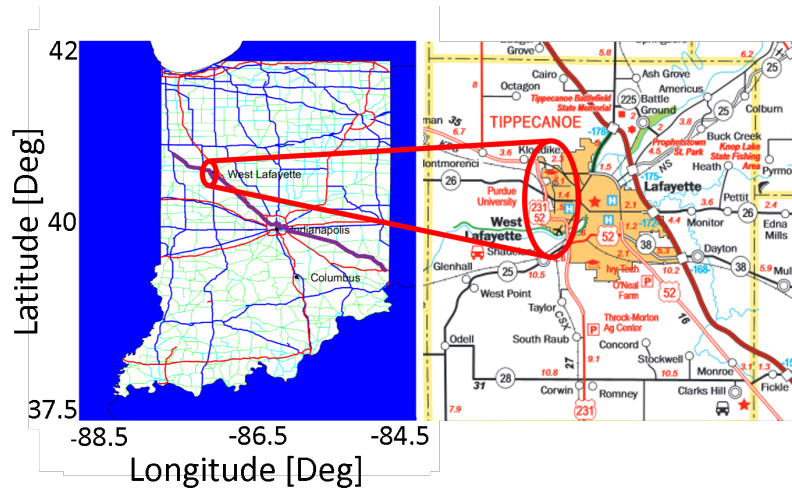


Figure 5.1. Five separate grade datasets are compared for south-bound US 231 near Purdue University in West Lafayette, Indiana

The LiDAR dataset’s accuracy had been confirmed by surveying this stretch of US 231, [60] and as such was used as a ground truth reference for the analysis outlined in this paper. The dataset labeled GPS was obtained by the authors with a cost-effective (\$10) single antenna GPS transponder attached to a vehicle driven at approximately 55 MPH. Both $IMU_{Int.Vel}$ and IMU_{Pitch} datasets were obtained from a cost-effective (\$2,720) VectorNav VN-200 inertial measurement system in the same vehicle. The Comm road grade dataset was purchased, and accessed through the road gradient layer in the supplier’s Advanced Driving Attributes product (release: 2014 Q3). The supplier states that road grade was collected by mobile mapping vans which use undefined “high end mapping and positioning equipment.” [61]

The elevation profile obtained by GPS for the south-bound lane of US 231 is shown in Figure 5.2. A general decrease in elevation occurs over this corridor as the highway enters the Wabash River Valley. The LiDAR system (a), MTK3339 single antenna GPS sensor (b), and VectorNav VN-200 IMU (c) are shown in Figure 5.3.

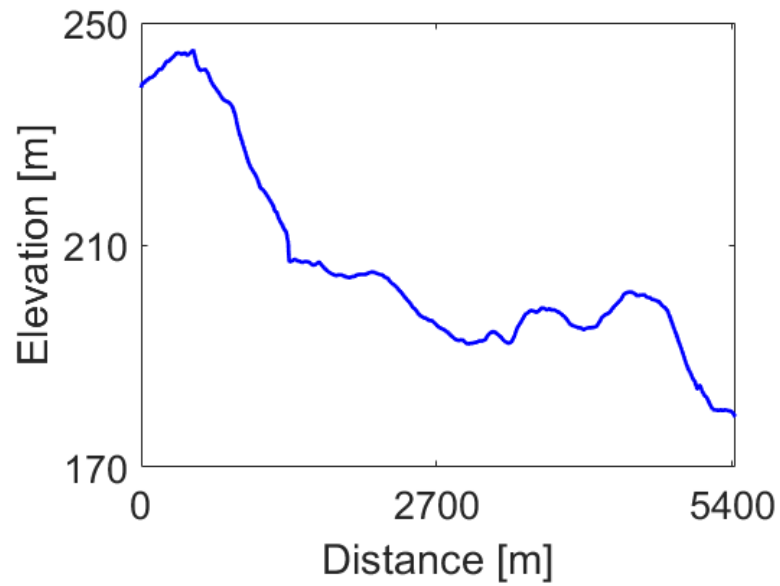


Figure 5.2. Elevation for southbound US 231 near Purdue University, acquired from GPS.

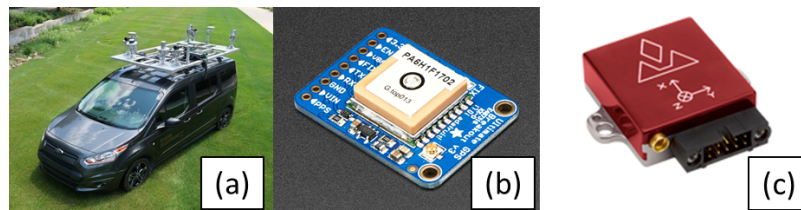


Figure 5.3. Of the grade datasets acquired three methods were used, a) LiDAR from colleagues in Purdue Civil Engineering, b) MTK3339 GPS, and c) IMU pitch, and integrated velocity output.

Table 5.1. Grade data types available for 5,432 meters of south-bound US 231 in West Lafayette, Indiana, with labels and definitions.

Grade Label	Description
<i>LiDAR</i>	High quality grade data obtained in cooperation with colleagues in Purdue Civil Engineering, [60] with stated elevation accuracy ≤ 1.42 cm of true road surface over 10 m, sampled at 0.5 m intervals
<i>GPS</i>	Elevation and position data obtained by authors from an MTK3339 single antenna GPS receiver, with up to 22 satellites, sampled at 10 Hz
<i>IMU_{Int.Vel}</i>	Grade from a VectorNav VN-200 IMU, with single GPS antenna, obtained by integrating horizontal and vertical velocity, sampled at 100 Hz
<i>IMU_{Pitch}</i>	Grade from a VectorNav VN-200 IMU, with single GPS antenna, obtained from pitch of the unit, sampled at 100 Hz
<i>Comm</i>	Commercially available road grade dataset, accuracy varies over the corridor, with some sections missing, sampling is variable down to 15 m intervals

Grade was calculated as rise, h , divided by run, D , per Equation (5.1), and yielded road surface slope as illustrated in Figure 5.4. Data obtained from the GPS sensor was already given in a horizontal distance, D , versus elevation, h , format.

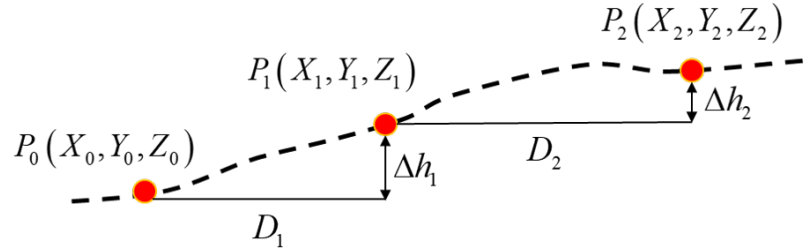


Figure 5.4. The GPS unit provides horizontal distance traveled, D , as well as elevation, h , which is used to calculate grade by Equation (5.1)

$$Grade(\%) = \frac{\Delta h_n}{D_n} \times 100 \quad (5.1)$$

The IMU was used to calculate grade two different ways, from i) a time integration of the velocity output and ii) calculating the tangent of the IMU pitch, ϕ . It is not often feasible to align the IMU's $\phi = 0^\circ$ axis with the longitudinal axis of the vehicle, so the pitch offset is removed during post processing. The calculation for grade as a function of IMU pitch is shown in Equation (5.2).

$$Grade(\%) = \tan(\phi) \times 100 \quad (5.2)$$

Determining grade from the IMU's x , y , and z velocities is accomplished via Equations (5.1), (5.3), & (5.4). Velocity on the horizontal x - y plane is denoted as V_x and V_y , and the z or elevation axis is V_z . The subscript n is sample number.

$$D_n = \int \sqrt{V_x^2 + V_y^2} dt \quad (5.3)$$

$$\Delta h_n = \int V_z dt \quad (5.4)$$

All acquired data was filtered with a 150 point moving average, a form of low pass filtering. Zhang et al. showed that low pass filtering is appropriate for road grade

data since noise introduced by suspension movement and other vibrations occur at much higher frequencies than changes in road grade. [42]

5.2.2 Grade Post-processing

The five grade datasets are shown in Figure 5.5. It is typical for the IMU mounting offset to be calibrated by subtracting off the grade difference over a known 0% grade, such as a flat parking lot. Since high quality LiDAR grade data was available in this work, the mounting offset was subtracted from a segment where the LiDAR indicated 0% road grade, shown in Figure 5.6.

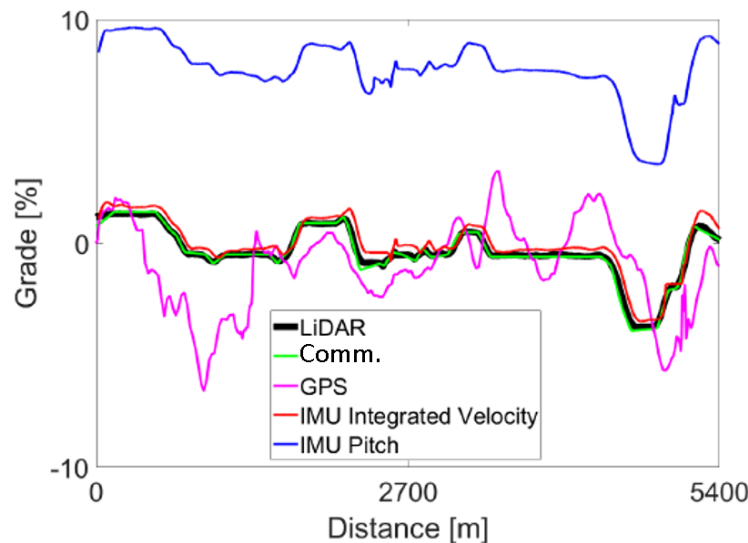


Figure 5.5. The IMU pitch is offset due to the mounting configuration on the vehicle, this must be accounted for by subtracting off the offset from the reference LiDAR during a known flat section of road.

The road grade datasets for LiDAR, $IMU_{Int.Vel}$, IMU_{Pitch} , and Comm follow a similar trend. The GPS grade dataset did not agree well with the other four datasets. The reasons for this include a large relative error in both measured position and elevation and a changing number of satellites during data acquisition. The absolute error in percent grade, calculated by Equation (5.5), is shown in Figure 5.7. The

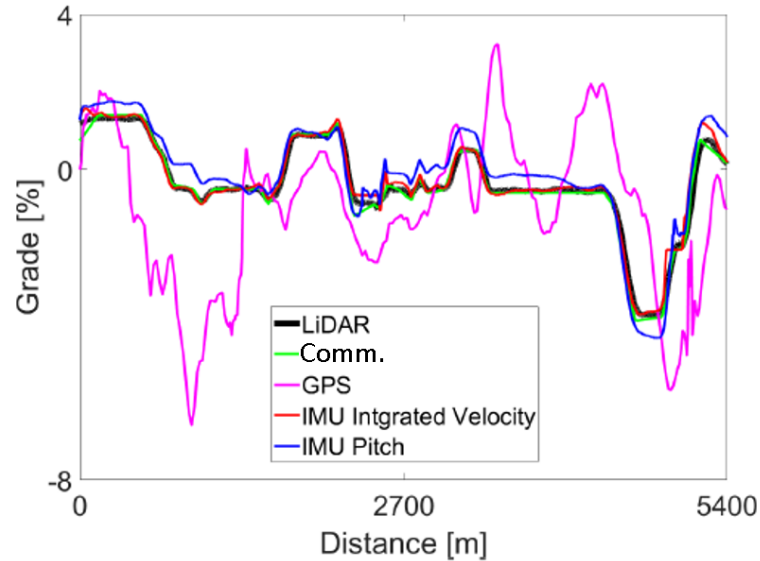


Figure 5.6. The IMU pitch offset was subtracted by finding the difference from the reference LiDAR dataset at a known 0 grade section.

resulting poor quality grade from GPS shown here agrees with the findings from Zhang et al., that calculating road grade without base station correction does not provide a good grade estimate. [42]

The magnitude of error in the IMU_{Pitch} dataset varied throughout the corridor, as the IMU moved with vehicle suspension travel, namely “squat” as the vehicle accelerated or climbed hills and “dive” during both braking and hill descent events. Suspension movement accounts for why the IMU_{Pitch} sometimes over-estimates grade during the initial segment as the logging vehicle was accelerating from a stop, and under-estimated (around 4,500 m) during a slow-down to a traffic signal. It is possible to account for suspension travel through back calculation with dynamics equations with knowledge of the suspension components, vehicle center of mass, engine torque, and vehicle acceleration. This was not done in this study as engine torque was not logged and suspension information for the logging vehicle is unknown.

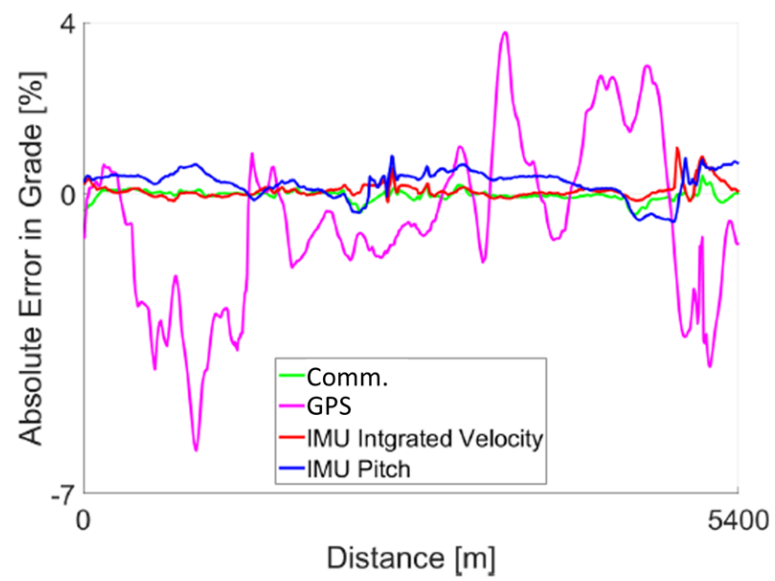


Figure 5.7. Absolute error in grade for each dataset relative to the reference LiDAR grade, as calculated by Equation (5.5).

$$\text{Absolute \% Grade Error} = \text{Grade} - \text{LiDAR} \quad (5.5)$$

5.2.3 Grade Regression Analysis

All five grade datasets were linearly interpolated into equally spaced 10 m segments over the 5,432 m corridor, to prevent over-sampling from skewing the regression analysis. The grade data from GPS, $\text{IMU}_{\text{Int.Vel}}$, $\text{IMU}_{\text{Pitch}}$, and Comm were then compared to the reference LiDAR with a linear regression detailed in Figure 5.8.

The commercially available dataset, Comm in Figure 5.8a, was not recorded by the authors. It was the best match to the LiDAR reference data over this corridor, with an R^2 value of 0.992, slope of 1.04 and small y-intercept of -.022. As will be described later, Comm did not fare nearly as well on other corridors. Per Figure 5.8b, the GPS system alone without a base station did not do a good job of determining the road grade. The R^2 value of 0.12, coupled with a non-unity slope (.6) and large y-intercept (-.799) shows a poor fit. Figure 5.8c shows that integrating the IMU's velocity produced a good approximation of the road's true grade. The regression slope for $\text{IMU}_{\text{Int.Vel}}$ of 0.999 coupled with a small y-intercept of .069, and high R^2 of 0.979 demonstrates that integrating the IMU's velocity is an adequate method to estimate the road grade, with any error generally being an over-estimate of road grade (regression points above the line). The regression analysis of the IMU's pitch as a proxy for road grade fared better than the GPS dataset, as shown in Figure 5.8d. The $\text{IMU}_{\text{Pitch}}$ dataset both over-predicted and under-predicted road grade. This is most likely due to unmodeled disturbances introduced by vehicle suspension travel, as discussed previously.

A summary of the regression analysis is shown in Table 5.2. Of the self-acquired grade data, integrating the IMU's velocity yielded the best match to the LiDAR grade reference set followed by the IMU's Pitch, and lastly the GPS data. The Comm dataset was the best match overall for the LiDAR road grade data.

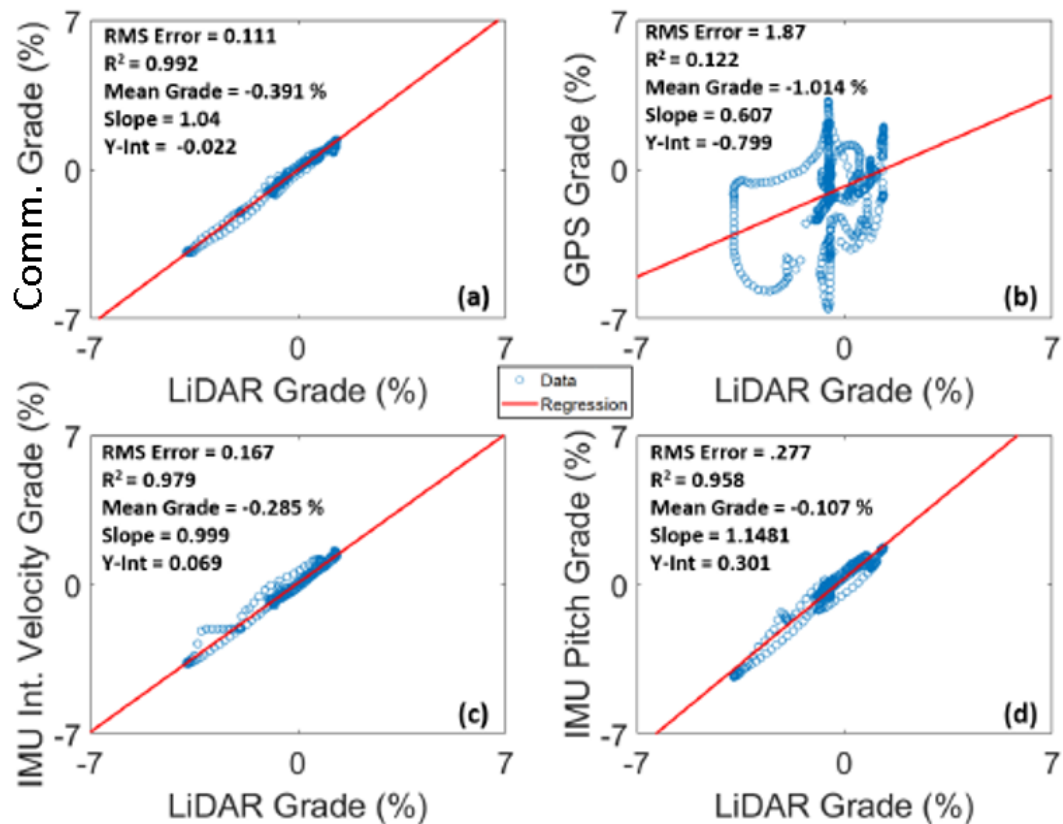


Figure 5.8. The Comm grade dataset (a) provided the best match for the high accuracy LiDAR data, followed by integrating the IMU's velocity output (c) and using the IMU's pitch (d). The economical single antenna GPS without a base station (b) did not provide a good correlation to the reference LiDAR grade.

Comm grade data was, however, problematic over other corridors. For example, Figure 5.9 shows that continuing south-bound on US 231, where high quality LiDAR data was not available, but where IMU and Comm grade were available, the Comm grade data quality decreased significantly. Specifically, at around the 8,000 to 9,000 m segment, there are only two Comm data points for 1 km. The accuracy of the available data points diminished as well. Apparently, it was by coincidence that the

Table 5.2. Summary of grade data regression analysis compared to the LiDAR reference, where $\text{Grade}_{\text{AVG}}$ is the average grade, Grade Error is the error in average grade from as calculated by Equation (5.6), and $\text{Grade}_{\text{RMS}}$ is the root mean square (RMS) grade.

Grade Label	$\text{Grade}_{\text{AVG}}$	Grade Error	$\text{Grade}_{\text{RMS}}$	\mathbf{R}^2
<i>LiDAR</i>	-.3548%	-	1.20	-
<i>GPS</i>	-1.014%	-185.9%	2.24	0.122
<i>IMU_{Int.Vel}</i>	-0.285%	19.7%	1.19	0.979
<i>IMU_{Pitch}</i>	-0.107%	69.9%	1.35	0.958
<i>Comm</i>	-.391%	-10.1%	1.26	0.992

Comm grade data was of high quality over the same section of US 231 where accurate LiDAR grade data was also available.

The limitations of the Comm grade dataset are also shown in Figure 5.10 for another route in Indiana, Interstate 69 near Indianapolis. Again the Comm dataset showed varying accuracy and resolution over the route.

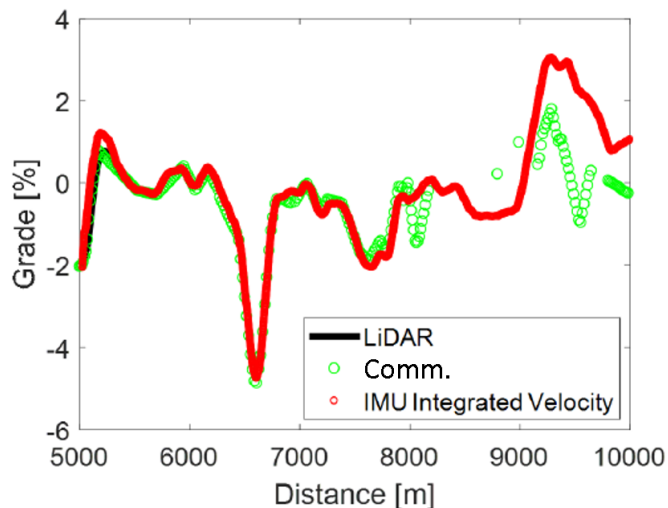


Figure 5.9. A limitation of the Comm dataset is that the quality can vary over a route. The Comm grade had missing data for up to 1 km further south on US 231, shown by only two points between the 8,000 and 9,000 m segments, or erroneous data as shown around 9,000 m. That the Comm data was of high fidelity over the same segment where LiDAR grade was available, 0 to 5,432 m, was happenstance.

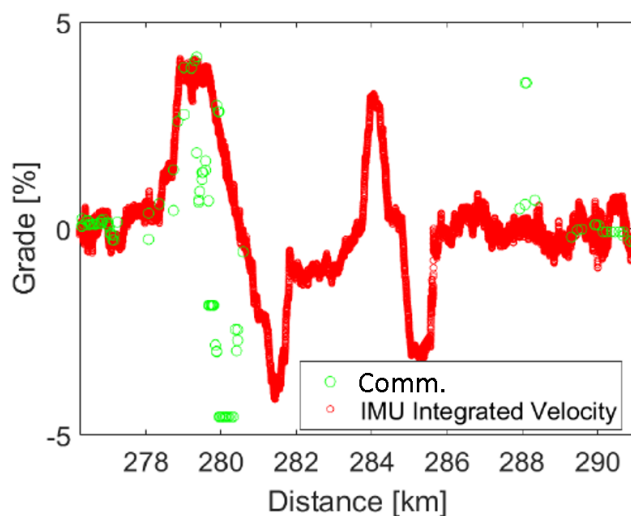


Figure 5.10. On another corridor where IMU data was available for comparison, Interstate 69 south of Indianapolis, IN, the Comm dataset is lacking in accuracy and missing points for up to 6 km stretches (particularly around 281-287 km).

5.3 Simulation Model Framework

A Peterbilt 579 Class 8 truck weighing 29,484 kg (65,000 lbs) equipped with a Cummins X15 Efficiency Series engine, and Eaton Endurant 12 speed automated manual transmission was simulated. The details of the vehicle model (red box in Figure 5.11 are confidential). The engine and transmission controllers were included as well as the effect of aerodynamic drag, rolling resistance, grade, and shift events. A drag coefficient, C_D , of 0.63 was used. [62, 63] A free body diagram of the truck is shown in Figure 6.8

The simulation framework, per Figure 5.11, includes the Class 8 truck model, as well as a driver model to realistically track a given desired speed input. Outputs from the simulation included vehicle speed, acceleration, and jerk, as well as engine speed, torque, fuel consumption and gear shift events.

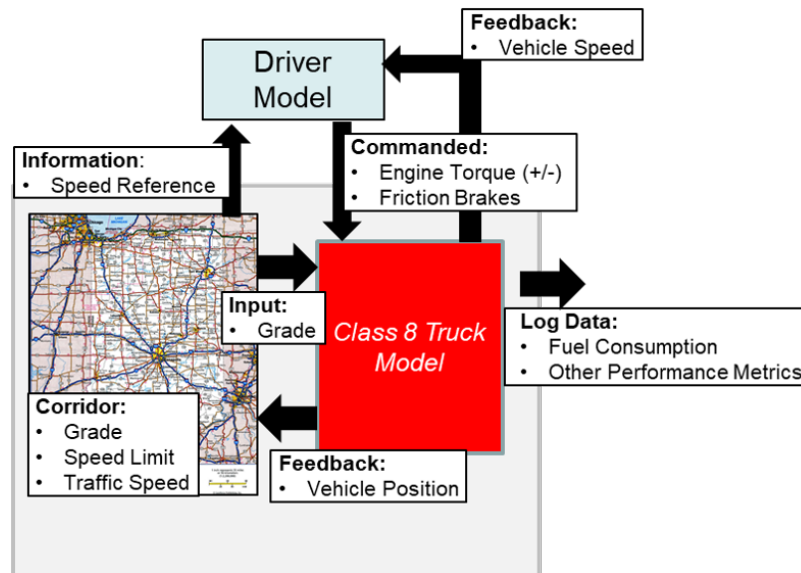


Figure 5.11. Simulation framework for studying the dynamics and fuel consumption of a Class 8 truck with respect to quality of grade data.

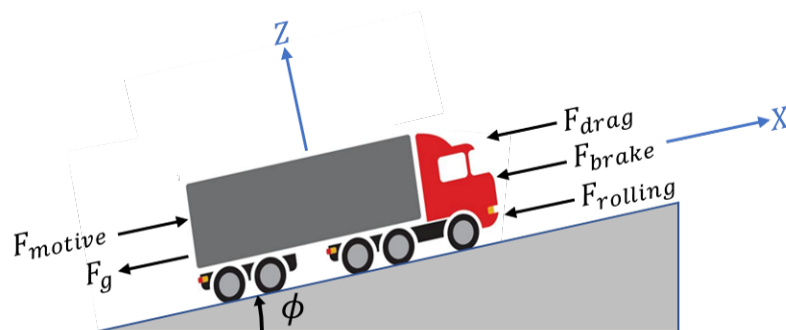


Figure 5.12. A free body diagram of the modeled Class 8 truck, detailing the forces considered: gravity, drag, engine and friction brakes, rolling resistance, and propulsive (motive) force.

5.4 Sensitivity of Model-based Fuel Consumption Predictions to Estimated Grade Error

A summary of the simulation initial conditions and parameters is shown in Table 5.3.

Table 5.3. Simulation parameters and initial conditions.

Simulation	Initial Desired Speed	C_D	Truck Mass
Single Class 8 Truck	24.6 m/s (55 MPH)	0.63	29,484 kg

The simulated truck speed, engine torque, and fuel consumption when each of the five grade datasets (defined per Table 5.1) are used are shown in Figures 5.13 and 5.14. Truck speed was maintained within 0.67 m/s (1.5 MPH) of the desired speed for all five simulations, though had a markedly different speed profile result when the GPS grade data was used. The transmission controller kept the truck in 11th gear (of 12 total gears) throughout the corridor for all five simulations. Friction brakes were not requested by the driver model to track the reference speed trace. The simulation using GPS-acquired grade data as an input shows a significantly different trend for engine

torque and cumulative fuel consumed, markedly where engine braking is saturated at 40s and 200s and engine torque is saturated at 130s. These saturated engine braking sections are where the GPS acquired road grade had negative grade as low as -7% , an absolute error of 6% below the other grade acquisition methods. The grade dataset with the highest average grade, IMU_{Pitch} , required more engine torque throughout the corridor and subsequently consumed the most fuel.

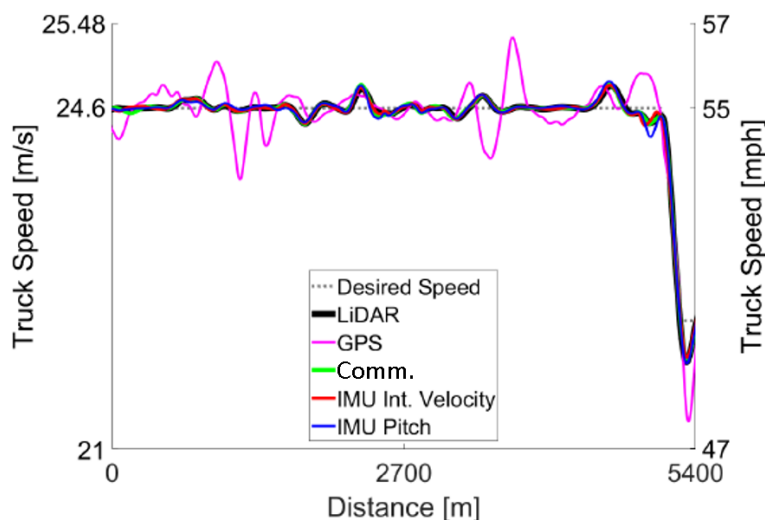


Figure 5.13. The driver model for all five simulations (from each of the five grade sources) maintained truck speed within 0.67 m/s (1.5 MPH) of the desired speed. The simulation using the GPS grade dataset resulted in a markedly different speed profile as a result of large grade error (up to 6% absolute error).

As expected, there was a trade-off between the quality of the road grade data used for simulation, and the predicted cumulative fuel consumption accuracy as shown in Figures 5.15 and 5.16. The GPS method for acquiring road grade under-estimated the average corridor road grade as -1.014% compared to the reference LiDAR average grade of $-.3558\%$. Using the GPS road grade in simulation predicted the lowest fuel consumption (normalized to the LiDAR baseline), 0.962 , for the corridor of the five datasets as compared to the LiDAR baseline normalized fuel consumption of 1.000 . The dataset IMU_{Pitch} over-estimated road grade on average, produced the highest

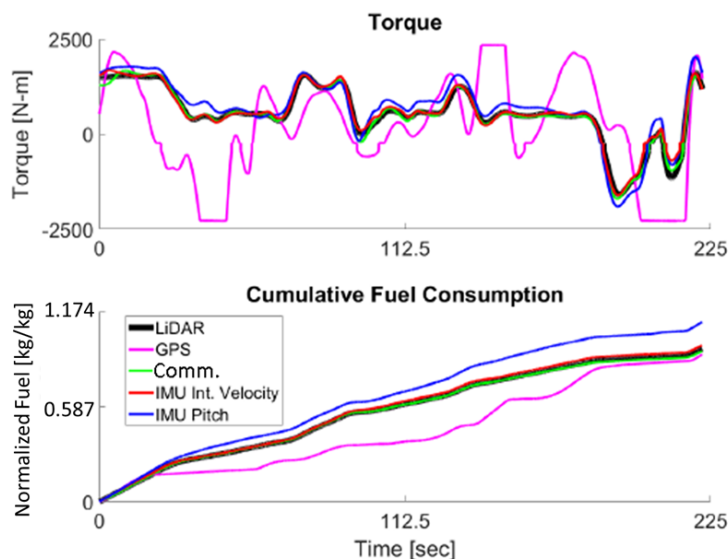


Figure 5.14. The simulation performed with the GPS-acquired road grade showed saturation of the engine’s braking and propulsive torque, which did not occur with simulations using other road grade datasets.

average grade of -0.1068% , and predicted the highest normalized fuel consumption of 1.174.

The $IMU_{Int.Vel}$ data had a higher than LiDAR average road grade of -0.285% , while Comm had a lower than LiDAR average road grade of -0.391% . These two datasets continued the trend in simulation predicted fuel consumption with $IMU_{Int.Vel}$ having a higher than baseline (LiDAR) fuel consumption of 1.022 and Comm with a lower than baseline fuel consumption of 0.984.

Figure 5.16 shows the fuel consumption to grade quality trade-off in relative percentages to the baseline LiDAR grade dataset. It is shown that an average measurement error above the actual road grade predicted higher than baseline fuel consumption in simulation. Likewise, if the average road grade measurement was below that of the actual road grade then the simulation predicted lower than baseline fuel consumption. This is the result of a large relative fuel penalty for a Class 8 truck when climbing a grade, versus the marginally smaller fuel benefit of descending a

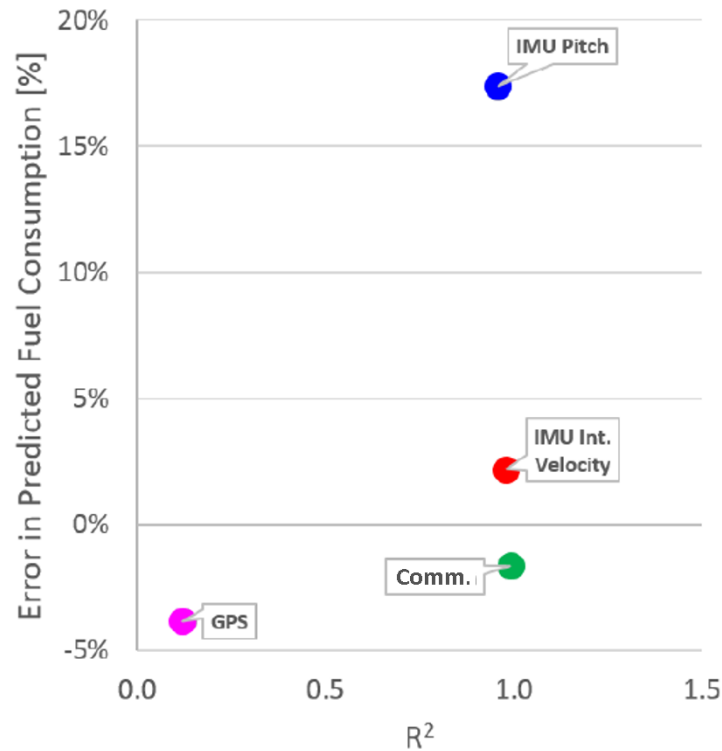


Figure 5.15. Simulation of a Class 8 truck, the baseline reference grade obtained by LiDAR with a mean grade of -0.3548% has a normalized fuel consumption of 1.000. Grade acquisition methods that have a higher average grade are predicted to consume more fuel in simulation.

grade. The IMU_{Pitch} dataset over-estimated average grade by 69.9%, as calculated by Equation (5.6), and as a result the simulation over-predicted fuel consumption by 17.4%. Using the GPS dataset as a simulation input for road grade under-estimated average grade by -185.9% and also predicted fuel consumption to be just -3.8% lower than the reference simulation using LiDAR grade.

$$Grade\ Error = \frac{mean(Grade) - mean(LiDAR)}{mean(LiDAR)} \quad (5.6)$$

A summary of the simulation results is shown in Table 5.4. For this corridor, grade data from Comm had the closest fuel consumption prediction to the LiDAR baseline followed by $IMU_{Int.Vel}$, GPS and IMU_{Pitch} .

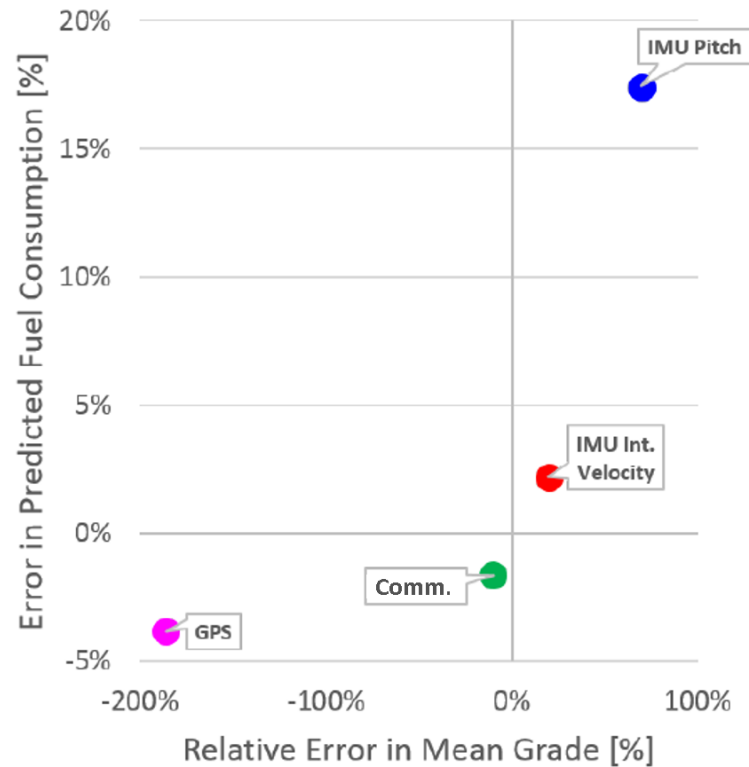


Figure 5.16. Relative to the LiDAR baseline, the simulation predicted fuel penalty from over estimating average road grade is higher than the fuel benefit from under estimating average road grade.

Table 5.4. Summary of fuel consumption (normalized to the LiDAR baseline) and grade data regression analysis compared to the LiDAR reference, grade error calculated per Equation (5.6).

Grade Label	Grade _{AVG}	Grade Error	Normalized Fuel Cons. (kg/kg)	Cumul. Energy
<i>LiDAR</i>	-0.3548%	-	1.000	6.78 MJ
<i>GPS</i>	-1.014%	-185.9%	0.962	6.36 MJ
<i>IMU_{Int.Vel}</i>	-0.285%	19.7%	1.022	6.99 MJ
<i>IMU_{Pitch}</i>	-0.107%	69.9%	1.174	8.30 MJ
<i>Comm</i>	-0.391%	-10.1%	0.984	6.66 MJ

6. CAPTURING THE IMPACT OF SPEED, GRADE, AND TRAFFIC ON CLASS 8 TRUCK PLATOONING

6.1 Motivation

The simulation framework described here brings together unique aspects, including the aforementioned real-world traffic and road grade data, and a production-intent two-truck platooning controller. Together with high fidelity class 8 truck models, the simulation framework uniquely demonstrates how speed, grade, and traffic affect the absolute, and relative, fuel saving benefits of two-truck platooning.

6.2 Simulation Framework

6.2.1 Corridor Grade Data Acquisition & Post-processing

Figure 6.1 shows west-bound I-74 in Indiana between US 231 and the Illinois state line. Road grade data is obtained by integrating the velocity output from a VectorNav VN-200 Inertial Measurement Unit (IMU) shown in Figure 6.2, per Equations (6.1)-(6.3). Figure 6.3 shows a visual representation of how grade is calculated.

A 150 point moving average filter is used to remove noise from the road grade data. A moving average filter acts as a low-pass filter which is appropriate for post-processing grade data because the noise introduced to grade data, such as from suspension travel and vehicle dynamics, is high frequency relative to the slower changing topography of grade. [42]

To ensure that the data obtained by integrating the IMU's velocity output is accurate, a comparison study was done using high accuracy LiDAR grade data provided by colleagues in Purdue's Civil Engineering available for a 5,432 m stretch of US 231.



Figure 6.1. I-74 is a trucking corridor in Indiana, west-bound I-74 from US 231 to the Illinois border spanning 54.7 km (34 miles) is used as a simulation corridor in this study.

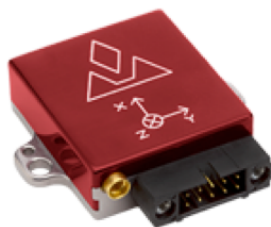


Figure 6.2. A VectorNav VN-200 IMU is used to obtain grade data for I-74 west-bound in Indiana.

A regression analysis of the grade calculated from the integrated IMU velocity versus the LiDAR grade showed a good match, with R^2 of 0.979. [56]

$$Grade(\%) = \frac{\Delta h_n}{D_n} \times 100 \quad (6.1)$$

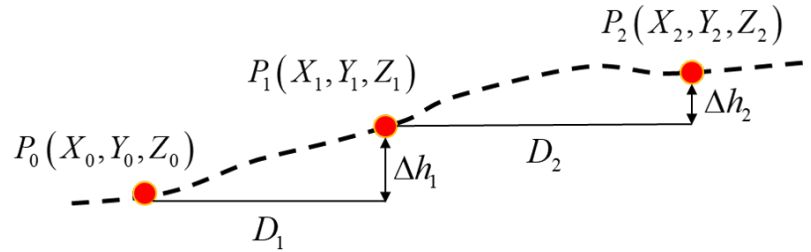


Figure 6.3. The IMU provides horizontal velocity which is integrated to obtain distance traveled, D , as well as vertical velocity which is integrated to find elevation, h , which is used to calculate grade by Equations (6.1)-(6.3).

$$D_n = \int \sqrt{V_x^2 + V_y^2} dt \quad (6.2)$$

$$\Delta h_n = \int V_z dt \quad (6.3)$$

6.2.2 INDOT Traffic Speed

Traffic speed data available in 15 minute intervals and 0.1 mile marker increments from INDOT is used to simulate a real-world scenario. [64] Data from a Friday evening at 5:00 PM is used in this study. The INDOT data is used to set an upper bound on the truck's speed, effectively reducing the speed limit of the corridor. The INDOT data is shown in Figure 6.4 in a histogram format, where the color corresponds to the traffic speed and the size of the color band corresponds to the percent of time (over an hour) spent at that speed.

The INDOT traffic data is converted to an average traffic speed by calculating the weighted average speed. This speed profile, in Figure 6.5, is used as the speed reference for the Class 8 truck in simulation. In this scenario, traffic near the beginning of the corridor is moving at 25 m/s (56 MPH), or 4 m/s (9 MPH) slower than the 29 m/s (65 MPH) heavy truck speed limit. As shown, throughout the corridor, based on

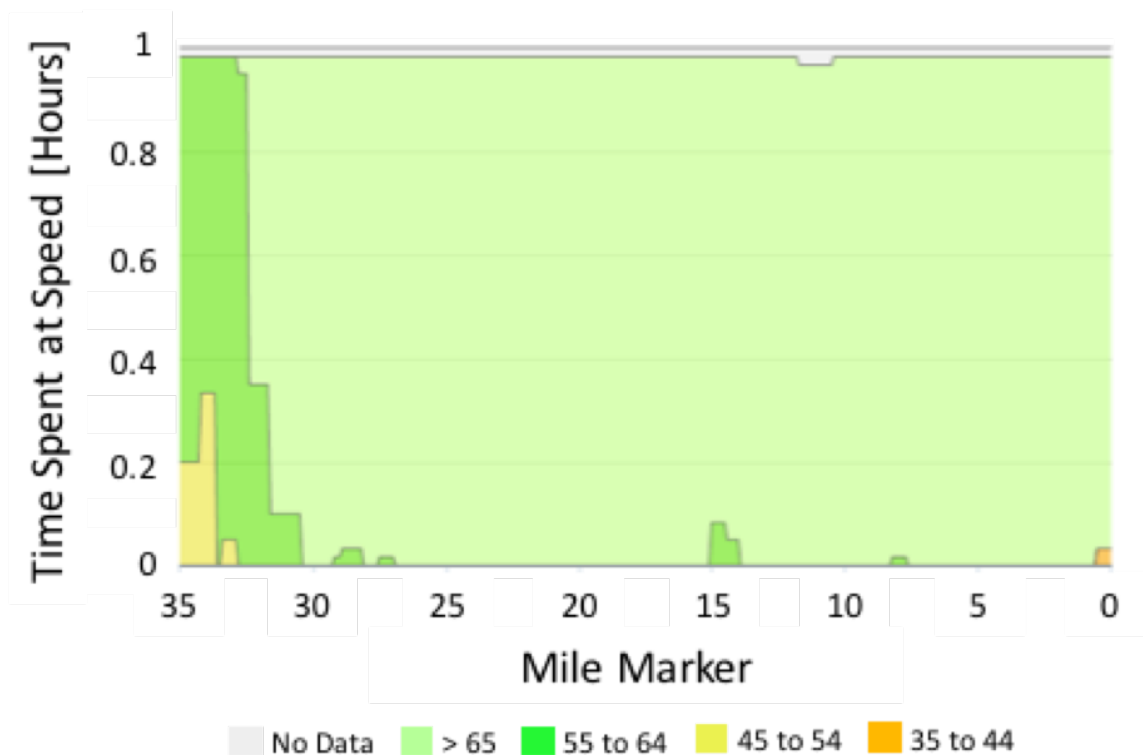


Figure 6.4. Traffic speed data obtained from INDOT for west-bound I-74 at 5PM on a Friday, color code corresponding to traffic speed and the width of the color band demonstrating the percent of an hour spent at that speed.

traffic data for a typical Friday at 5PM, the truck is not able to maintain the route's actual speed limit of 29 m/s (65 MPH).

Another corridor, I-69 in southern Indiana, is also used in this study to understand the impact of high grade on platooning class 8 truck performance and fuel savings. The posted speed limit and road grade of north-bound I-69 is shown in Figure 6.6. The heavy grade on this 60 km (37.3 mile) span of I-69 ranges from -5 to +5%. Grade data is obtained using the VN-200 IMU shown in Figure 6.2.

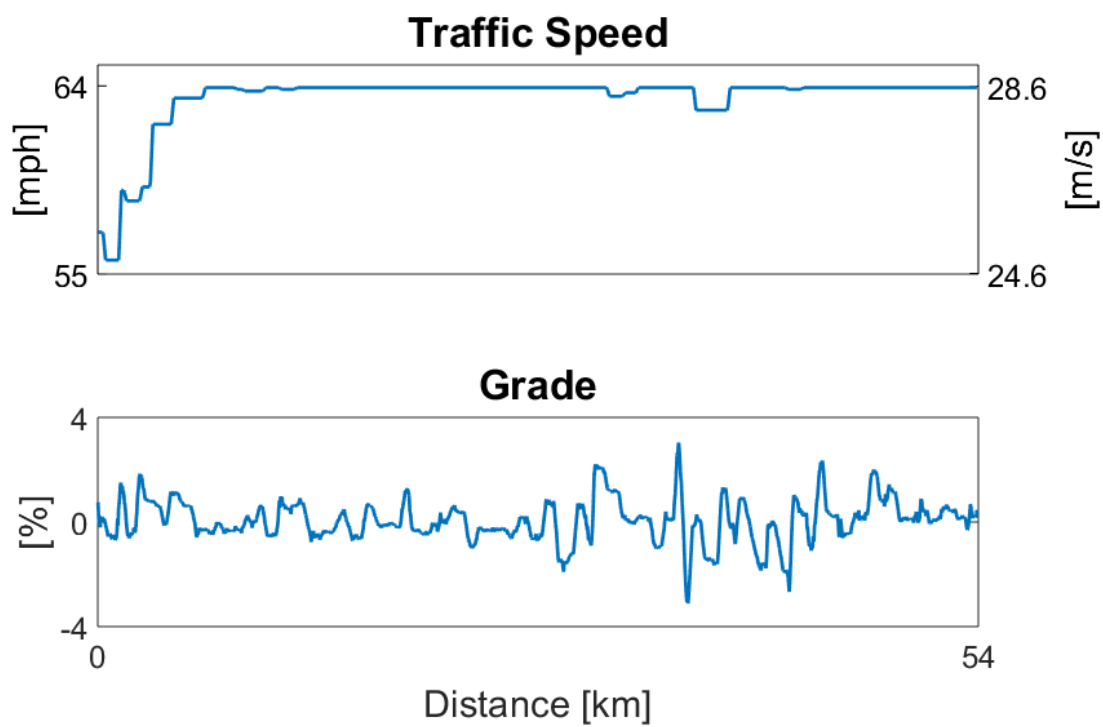


Figure 6.5. INDOT traffic speed for west-bound I-74 in Indiana at 5PM on a Friday converted to a reference speed for the simulated Class 8 truck. Due to traffic, the truck is not be able to obtain the posted commercial vehicle speed limit of 29 m/s (65 MPH). Mile Marker 0 (54 km) is at the Illinois state border.

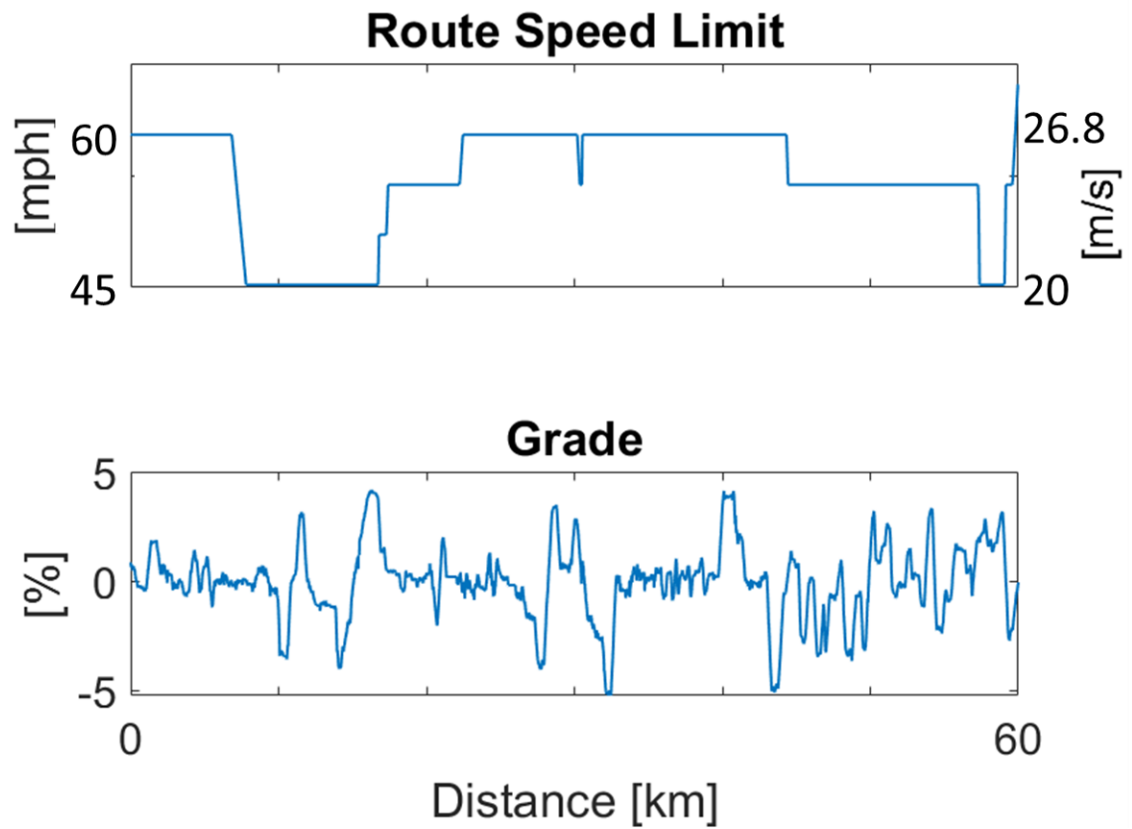


Figure 6.6. The posted speed limit for north-bound I-69 in Indiana is used as the reference speed for the simulated Class 8 truck. Road grade on I-69 is aggressive, ranging from $\pm 5\%$.

6.2.3 Single Truck Simulation

The single class 8 truck simulation framework is shown in Figure 6.7. The modeled truck is a Peterbilt 579 Class 8 truck loaded to 29,484 kg (65,000 lbs) with a Cummins X15 efficiency series engine and an Eaton Endurant 12-speed transmission. The class 8 truck model (red box in Figure 6.7) itself is proprietary. The truck model's inputs include vehicle mass, drag coefficient, rolling resistance coefficient, friction brake command, and road grade. The truck model's torque input is actuated by a driver model, which outputs a torque command (positive torque, motoring torque, or engine-brake) based on tracking a vehicle speed reference input.

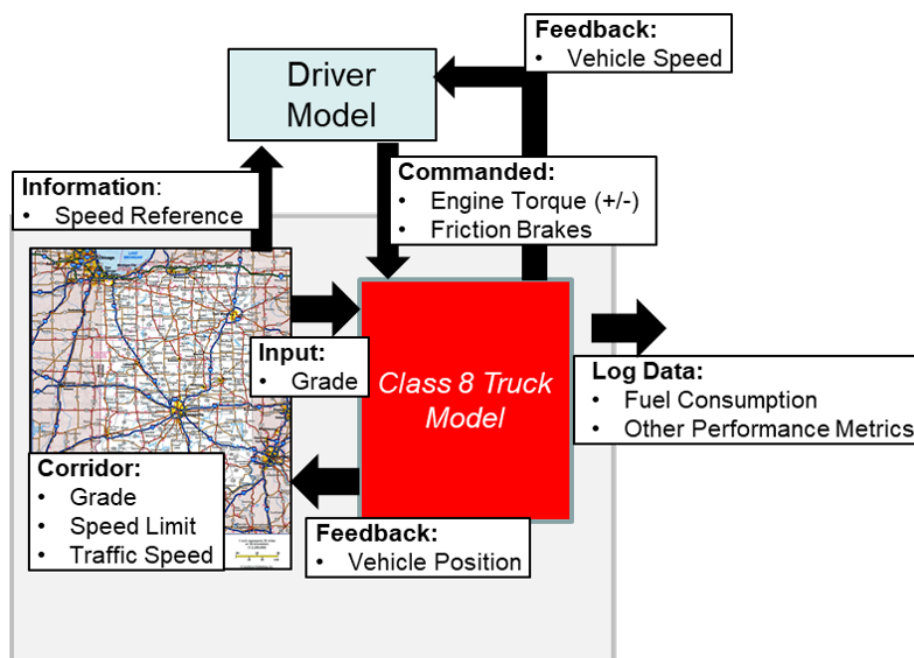


Figure 6.7. The single truck simulation framework utilizes a driver model to track a desired speed reference. Unique aspects include: speed reference modified using traffic speed data available from IN-DOT and road grade for the corridor obtained by the authors with a known quality.

A constant drag coefficient, C_D , of 0.63 was used as an average value for a Class 8 truck. [62,63] A free body diagram of the truck, shown in Figure 6.8, illustrates the

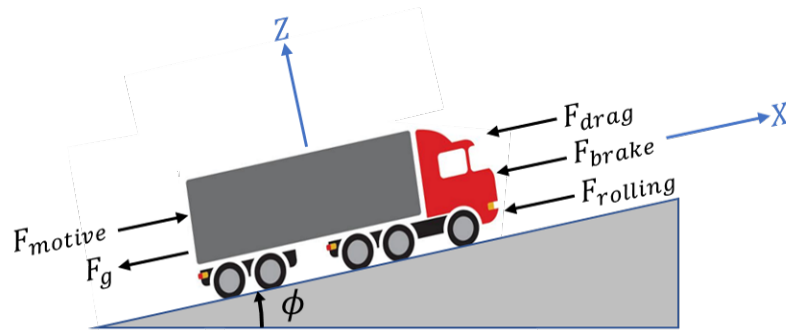


Figure 6.8. A free body diagram of the modeled Class 8 truck, detailing the modeled forces from aerodynamic drag, engine and friction brakes, rolling resistance, gravity, and propulsive force.

forces that are considered in the vehicle model: aerodynamic drag, rolling resistance, engine or friction brakes, and gravity through road grade. Outputs from the vehicle model include predicted fuel consumption, engine speed and torque, vehicle position and speed, gear number and other variables.

6.2.4 Platooning Trucks Simulation

The simulation framework used to study two trucks in a platoon, Figure 6.9, includes two copies of the same class 8 truck model shown in Figure 6.7. The lead vehicle operates in the same fashion as the single vehicle simulation framework (Figure 6.7), where a driver model tracks a speed reference by commanding engine torque or friction brakes.

The rear vehicle is operated via a model representative of Peloton Technology's production-intent platooning controller. The platooning controller details are kept confidential, but inputs to the controller include information about both the lead and rear vehicles. The controller actuates engine torque (positive, motoring, or engine-braking) or foundation brakes (if necessary) to maintain desirable follow distances. In this study, the vehicle gap setpoint is 11 m (36 ft). The aerodynamic drag coefficients (experimentally obtained by Salari [65]) as a function of platooning gap for both the

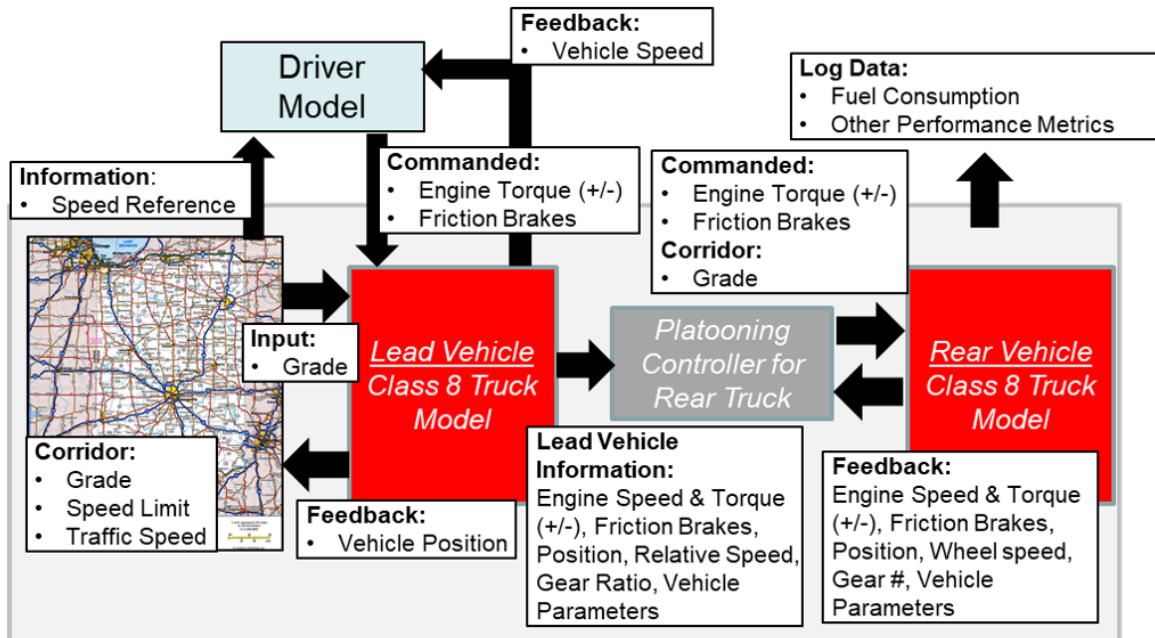


Figure 6.9. Platooning truck simulation framework: The lead truck utilizes the same driver model to track the speed reference input, while the rear truck is controlled by a commercially available platooning controller. Unique aspects include: speed reference modified using traffic speed data available from INDOT, road grade with a known accuracy for the corridor obtained by the authors, and a commercially available platooning controller automating the rear truck.

front and rear vehicles in the platoon shown in Figure 6.10 are from Salari's DOE annual merit review presentation.

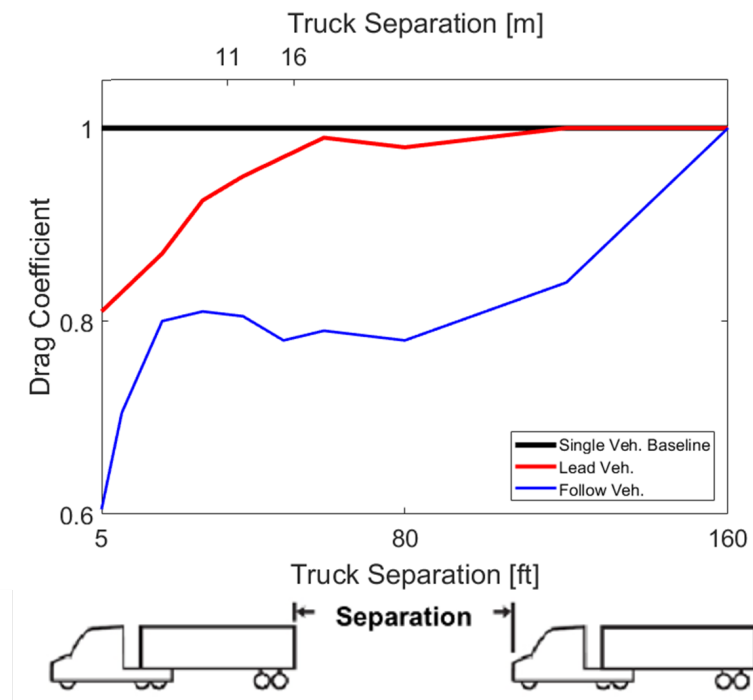


Figure 6.10. Aerodynamic drag coefficient as a function of platoon spacing normalized to that of a single truck, both the lead and rear vehicles have reduced drag in a platoon. [65]

6.3 Results

6.3.1 Comparison to Flat Ground Experimental Data

Experimentally obtained fuel consumption results for platooning Peterbilt 386 trucks, which used the same platooning controller studied here, showed a platoon average fuel consumption benefit of 7.25% over a baseline single vehicle (4.5% lead vehicle, 10% rear vehicle) on flat ground traveling at 28.6 m/s (64 MPH) with an 11m (36 feet) following distance. [58] The platooning Peterbilt 386 trucks used in the experiment were both equipped with Cummins ISX15 engines and Eaton 10-speed transmissions.

The simulation framework in this work assumes Peterbilt 579 trucks powered by Cummins X15 efficiency series engines with Eaton 12-speed transmissions. Although the experiment and simulated trucks and powertrains are different, a relative-to-baseline comparison using the same platooning controller and following distance (11 m, 36 ft) is performed to understand if the fuel consumption savings through reduced aerodynamic drag are similar.

With a constant speed of 28.6 m/s (64 MPH), the simulation predicts an average fuel savings of 7.45% for the platooning Peterbilt 579 trucks, which is consistent with the experimentally obtained fuel savings of 7.25%. Figure 6.11 shows the diverging cumulative fuel consumptions of the single vehicle baseline and platooning trucks over 1,900 s of operation. Relative to baseline fuel consumption, the lead truck saves 3.61% and the rear truck saves 11.29%. An aerodynamic drag force of 2,785 N acts on the single truck, which reduces to 2,613 N on the lead truck in the platoon and 2,248 N on the rear truck.

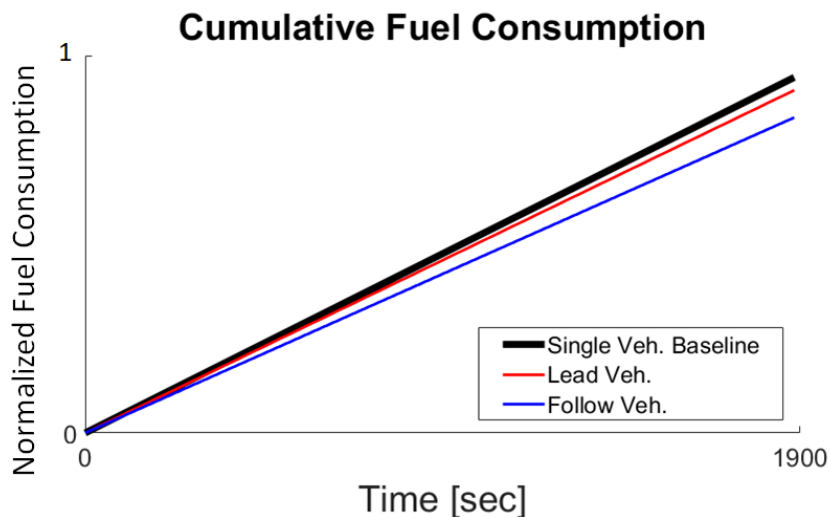


Figure 6.11. Cumulative fuel consumption from simulation of 11 m (36 ft) spaced platooning Peterbilt 579 trucks traveling at a constant 28.6 m/s (64 MPH) on flat ground, where the lead truck saves 3.61% over a baseline single truck, and the rear truck saves 11.29% for a platoon averaged 7.45% fuel savings.

Table 6.1. Experimentally obtained fuel savings of platooning Peterbilt 386 trucks over a baseline single Peterbilt 386 truck compared to simulated platooning Peterbilt 579 trucks fuel savings relative to a single Peterbilt 579 truck. Trucks on flat ground traveling at 28.6 m/s (64MPH) with a platooning distance of 11m (36ft).

Tested Peterbilt 386 Trucks	%Δ Fuel Cons. from Baseline
Platoon: Lead	-4.5%
Platoon: Rear	-10%
Platoon Avg.	-7.25%
Simulated Peterbilt 579 Trucks	%Δ Fuel Cons. from Baseline
Platoon: Lead	-3.61%
Platoon: Rear	-11.29%
Platoon Avg.	-7.45%

6.3.2 Steady-state Flat Ground Platooning

On-road platooning is expected to occur at larger gap setpoints greater than 11 m (36 ft) such as 16.7 m (54.8 ft). The aerodynamic drag coefficient for the lead truck increases relative to that of an 11 m (36 ft) gap but the drag coefficient is unchanged for the rear truck in the platoon per Figure 6.10. When traveling on flat ground at a constant speed of 28.6 m/s (64 MPH) at this higher gap setpoint, the simulation predicts a platoon average fuel savings of 6.9%, with 1.19% savings from the front truck and 12.60% from the rear. An aerodynamic drag force of 2,785 N acts on the single truck baseline, which reduces to 2,728 N on the lead truck and 2,185 N on the rear truck.

Traveling at a reduced speed of 24.5 m/s (54.8 MPH) on flat ground, the two-truck platoon averages 5.54% fuel savings over baseline (0.29% for the front truck and 10.79% for the rear truck) as shown in Table 6.2. As aerodynamic drag force changes with the vehicle velocity squared, there is less absolute drag force to be reduced through platooning at slower speeds and thus lower fuel savings from platooning. At lower speed the single truck baseline's aerodynamic drag is 2,042 N, while the lead platooning truck sees 2,000 N and the rear truck has 1,603 N.

Table 6.2. Comparison of platooning trucks' fuel savings with a gap setpoint expected to be used in the real world (distance = 16.7 m (54.8 ft)) at high and low speeds. At lower speeds, the platooning trucks save less fuel relative to baseline due to lower absolute aerodynamic drag.

High Speed 28.6 m/s (64 MPH)	%Δ Fuel Cons. from Baseline
Platoon: Lead	-1.19%
Platoon: Rear	-12.60%
Platoon Avg.	-6.90%
Low Speed 24.5 m/s (54.8 MPH)	%Δ Fuel Cons. from Baseline
Platoon: Lead	-0.29%
Platoon: Rear	-10.79%
Platoon Avg.	-5.54%

6.3.3 Steady-state Uphill and Downhill Platooning

Constant grade uphill (1% grade) and downhill (-3% grade) scenarios are simulated to better understand how the platooning controller handles road grade, and how grade impacts fuel savings. In both the uphill (Figure 6.12) and downhill (Fig 6.13) scenarios, the single vehicle baseline and platooning trucks travel at a constant 28.6 m/s (64 MPH), on constant grade, operating in steady-state (no gear changes, or acceleration).

Figure 6.12d shows that the platooning trucks require less engine torque to maintain speed uphill, through aerodynamic drag reduction.

The platooning controller, given a setpoint of 16.7 m (54.8 ft), keeps the rear truck in the uphill scenario at the prescribed setpoint, Figure 6.12b, but opts to keep the rear truck at 16.94 m (55.6 ft) on the downhill, per Figure 6.13b. The trucks in both the uphill and downhill simulations experience roughly the same aerodynamic drag

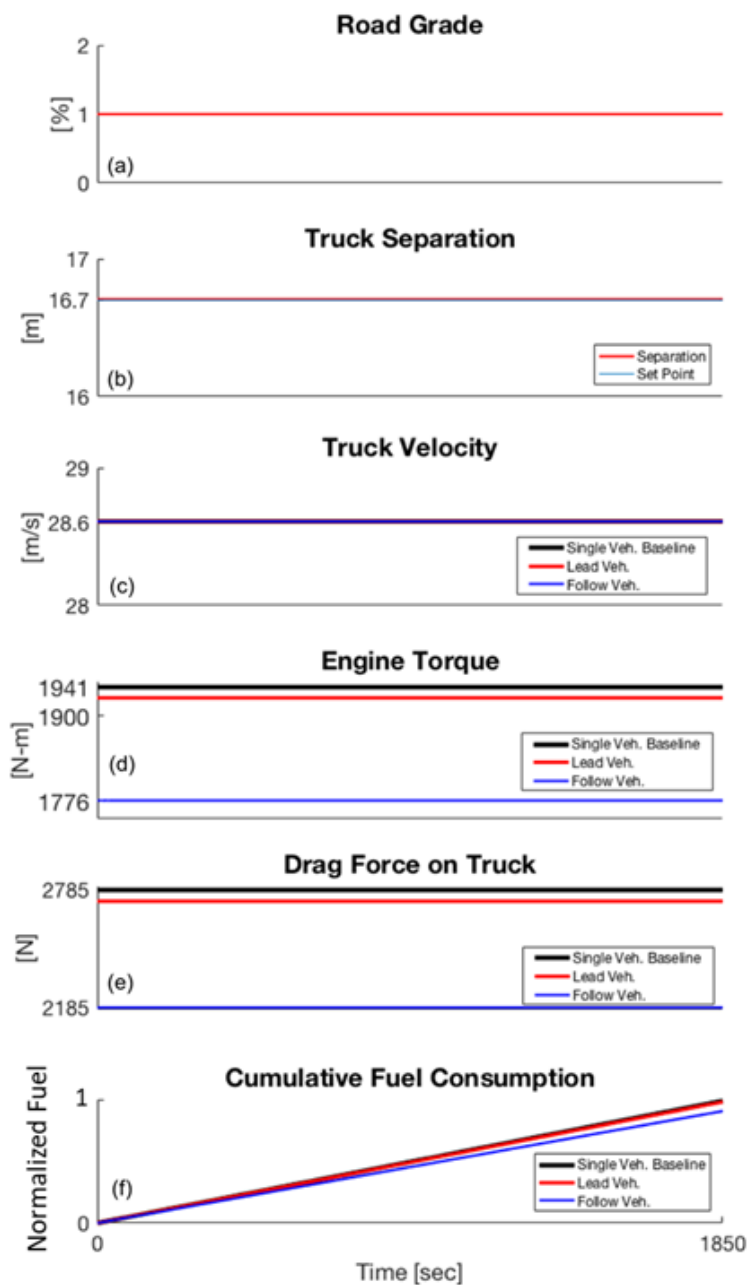


Figure 6.12. Traveling at 28.6 m/s (64 MPH) uphill (grade=1%), in steady-state, the platooning trucks with a 16.7 m (54.8 ft) gap save less fuel relative to the single vehicle baseline (4.58% platoon avg. savings) than on flat ground (6.90% platoon avg. savings), but have the same absolute aerodynamic force reduction.

forces, per Figures 6.12e & 6.13e, with slight variation due to drag from the 0.24 m (0.8 ft) gap difference and slightly different drag coefficients (C_d in Figure 6.10). The single vehicle baseline has 2785 N of drag, and the platooning trucks experience drag forces of 2,728 N on the lead truck uphill (2,732 N on the lead truck downhill), and 2,185 N on the rear truck uphill (2,188 N on the rear truck downhill). As expected, the aerodynamic drag forces both up and downhill match those from the high speed flat ground simulation because the trucks are traveling at the same speed.

Engine torque required to maintain speed for the single vehicle baseline on the uphill is 1,941 Nm. The lead truck in the platoon utilizes 1,926 Nm of torque, while the rear truck uses 1,776 Nm. Subsequently, the lead truck saves 0.81% fuel over baseline, while the rear truck reduces fuel by 8.35%, an average savings of 4.58% for the platoon as summarized in Table 6.3. The uphill relative fuel savings reduce from flat ground (Table 6.1), because though aerodynamic drag force reduction is the same, total propulsive energy increases due to the addition of grade. There are no fuel savings from platooning on the downhill (-3% grade) because the trucks are not consuming fuel (Figure 6.13f) while engine braking. As shown in Figure 6.13d, both the lead and rear trucks require more engine braking than the single vehicle baseline to maintain speed downhill (-982 Nm for the single vehicle baseline, -996 Nm for the lead truck, and -1,145 Nm for the rear truck).

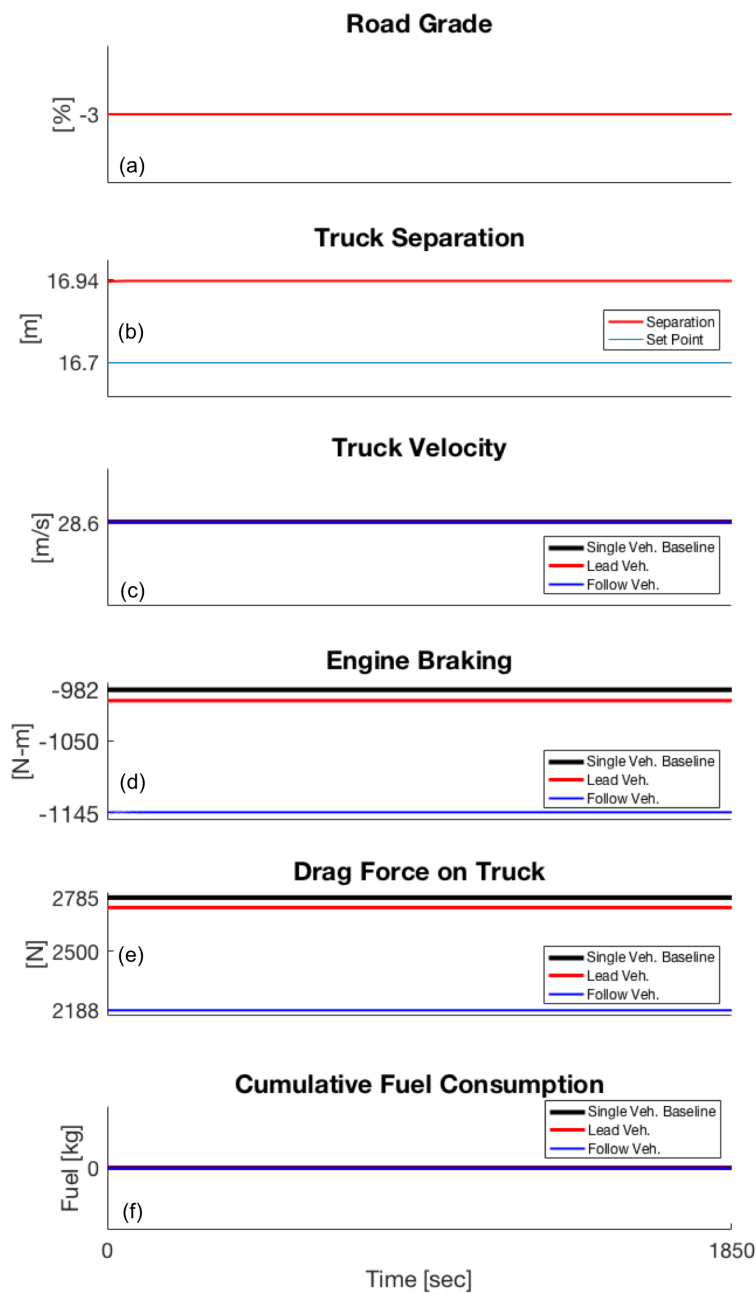


Figure 6.13. Traveling at 28.6 m/s (64 MPH) downhill (grade=-3%), in steady-state, the platooning controller maintains a gap higher than the setpoint of 16.7 m (54.8 ft) of 16.94 m (55.6 ft). Platooning enabled fuel savings through lower drag forces are not realized downhill as the trucks are engine braking and not consuming fuel.

Table 6.3. Summary of predicted fuel and energy consumption over a 33.5 mile constant uphill (1% grade) for platooning Class 8 trucks relative to the single Class 8 truck baseline, operating at steady-state and constant speed of 28.6 m/s (64 MPH). Operation downhill (-3% grade) shows no fuel consumption as the trucks are engine braking.

Simulation	%Δ from	Cumul.	%Δ from
Avg. Speed = 28.6 m/s	Baseline	Energy	Baseline
Single Class 8 Truck	-	150.3 MJ	-
Platoon: Lead	-2.35%	149.1 MJ	-0.80%
Platoon: Rear	-7.52%	137.5 MJ	-8.49%
Platoon Avg.	-4.94%	143.3 MJ	-4.64%

6.3.4 West-Bound I-74 in Indiana (Moderate Traffic & Grade)

Both the single truck baseline (per Figure 6.7) and two-truck platoon (per Figure 6.9) start with the same initial conditions, an initial speed of 25.5 m/s (57 MPH) and then track the reference traffic speed in Figure 6.14d a for 5PM on Friday which was obtained from INDOT. The route's grade is shown in Figure 6.14a. The platooning trucks had completed draw-in and were already at the desired gap distance of 16.7 m (54.8 ft) when the simulation begins. A summary of the simulation parameters and initial conditions is shown in Table 6.4.

Table 6.4. Simulation parameters and initial conditions for west-bound I-74.

Simulation	Initial	Follow Dist.	C_D	Truck
	Speed	Setpoint		Mass
Single Class 8 Truck	25.5 m/s	-	0.63	29,484 kg
Two-Truck Platoon	25.5 m/s	16.7 m	Variable	29,484 kg

The single truck baseline requires 96.87 MJ of propulsive energy to complete the 57.4 km (34 mile) long I-74 west-bound corridor. The single vehicle baseline results are overlaid with the lead and rear platooning trucks' results in Figures 6.14-6.17.

The two-truck platoon has an average propulsive energy use of 90.39 MJ (6.69% reduction over baseline), and reduces fuel consumption by 6.18% over baseline. The percent reduction of fuel consumption over baseline is 1.06% for the lead truck and 12.29% for the rear truck. The fuel and energy consumption summary is shown in Table 6.5. The single truck baseline and front truck in the platoon both shift 9 times over the corridor, while the rear truck in the platoon shifts 6 times.

As shown in Figure 6.14b, the platooning gap temporarily increases by up to 7.3 m during sustained 2.5% grades (e.g., at the 68 and 113 second marks). Otherwise the platooning distance setpoint is maintained. The controller does not allow the gap to decrease below the 16.7 m (54.8 ft) setpoint at any point.

An enlargement of the sustained 1.5-2% grade section and subsequent 24 m (78.7 ft) platoon gap is shown in Figure 6.15. The lead vehicle in the platoon down-shifts from 12th to 11th gear (Figure 6.15f) in order to maintain the reference speed on the 1.5-2% grade, as it approaches the halfway point of the hill (Figure 6.15a). Engine torque output, Figure 6.15e, from the lead vehicle drops to 0 Nm during the down-shift (while driver intended torque saturates at the torque curve). Driver intended torque is defined as what the driver model (lead truck) or controller (rear truck) would have otherwise commanded torque to be had a shift not occurred, in this case maximum torque.

The rear truck slows down as a result of the grade and the platooning controller matching the lead vehicle's engine torque output of 0 Nm in an attempt to prevent the separation distance from reducing. The rear truck performs a down-shift to 11th gear as it slows down. The subsequent drop in engine torque also contributes to the speed reduction of the rear truck, resulting in a rear truck relative speed reduction of 0.67 m/s (1.5 MPH) per Figure 6.15d, and gap increase to 24 m, as shown in Figure

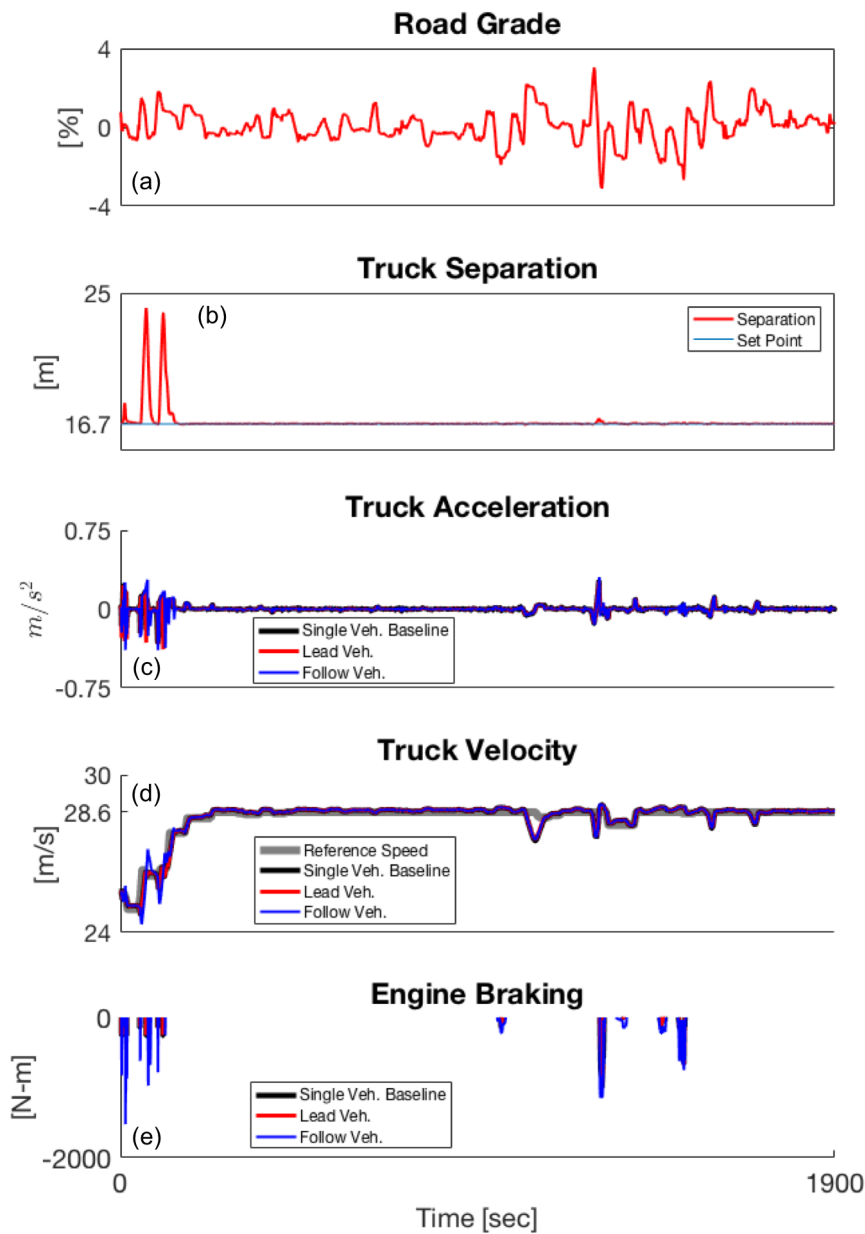


Figure 6.14. The single truck baseline and the platooning trucks track the reference speed (set by average traffic speed) throughout the simulation. The rear vehicle in the platoon is able to exceed the reference speed because vehicle cut-ins to the platoon are not considered. The platooning gap set point of 16.7 m is also maintained except during sustained grades of around 2.5% or more.

6.15c. The rear vehicle subsequently accelerates, returning to the follow distance set point of 16.7 m (54.8 ft).

As just described, the platooning controller is temporarily challenged, but recovers, during elevated grades scenarios. In the scenario just described, the platoon is maintained, but with a temporary (30 s), and moderate (~ 7 m) increase in the gap. Similar behavior was exhibited two times throughout the corridor, as shown in Figure 6.14b. As a result of maintaining platooning-enabled fuel savings throughout the route, the two-truck platoon achieves a 6.18% fuel consumption reduction on this moderately challenging traffic/grade route, close to the 6.90% fuel savings on flat road per Table 6.2.

More specifically, Figure 6.16 shows the engine torque and drag force for the single truck baseline, as well as the lead and rear trucks in the platoon. The rear truck requires less propulsive engine torque throughout the 54.7 km (34 mile) corridor, a result of the rear truck's lower aerodynamic drag force. During the sustained 28.6 m/s (64 MPH) section of the test corridor, the rear truck's drag force is roughly 2,200 N, compared to the lead truck's 2,740 N and the single truck baseline's 2,800 N.

Cumulative fuel use (normalized) and propulsive energy are shown in Figure 6.17. The rear truck's fuel use is lower than both the single truck baseline and lead truck's fuel consumption throughout the corridor. This is shown again in Figure 6.17 where the rear truck's cumulative propulsive energy use is lower throughout the corridor as well.

A lower speed simulation on I-74 with an average speed of 24.5 m/s (54.8 MPH) shows diminished fuel savings through platooning despite better following distance maintenance with a max gap of 16.9 m (55.4 ft) as compared to the faster average speed simulation's max gap of 24.1 m (79.1 ft). The two-truck platoon averages 5.03% fuel savings over a single truck baseline, with 9.18% fuel savings from the rear truck and 0.87% from the lead truck. The predicted fuel and cumulative propulsive energy results are summarized in Table 6.6. This follows the trend of decreased fuel savings

Table 6.5. Summary of predicted fuel and energy consumption over a 34 mile section of I-74 in Indiana of the platooning Class 8 trucks relative to the single Class 8 truck baseline, using real-time traffic speed data as the reference speed.

Simulation	%Δ from	Cumul.	%Δ from
Avg. Speed = 28.3 m/s	Baseline	Energy	Baseline
Single Class 8 Truck	-	96.87 MJ	-
Platoon: Lead	-1.06%	95.75 MJ	-1.16%
Platoon: Rear	-11.29%	85.03 MJ	-12.22%
Platoon Avg.	-6.18%	90.39 MJ	-6.69%

through platooning at lower speeds as shown for the flat ground simulation in Table 6.2.

Table 6.6. A lower speed (24.5 m/s or 54.8 MPH) summary of predicted fuel and energy consumption over a 34 mile section of I-74 in Indiana of the platooning Class 8 trucks relative to the single Class 8 truck baseline.

Simulation	%Δ from	Cumul.	%Δ from
Avg. Speed = 24.5 m/s	Baseline	Energy	Baseline
Single Class 8 Truck	-	81.65 MJ	-
Platoon: Lead	-0.87%	80.83 MJ	-1.00%
Platoon: Rear	-9.18%	72.88 MJ	-10.74%
Platoon Avg.	-5.03%	76.86 MJ	-5.87%

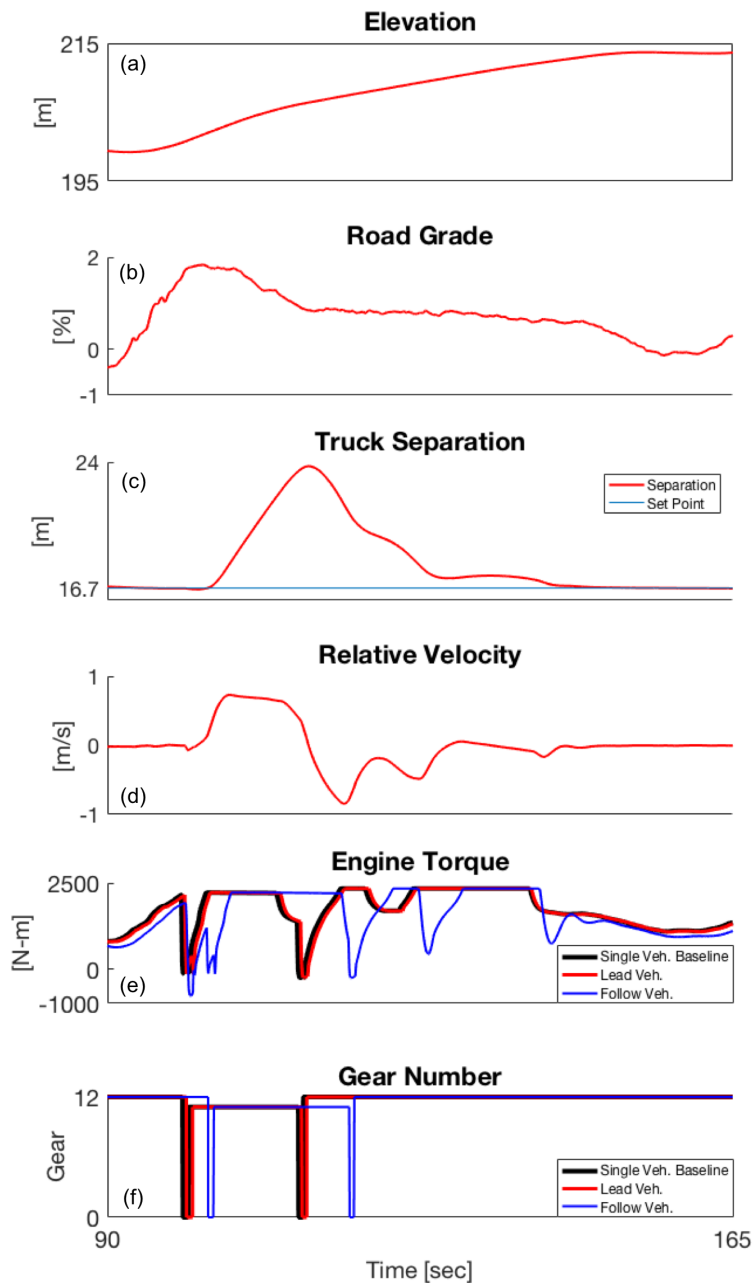


Figure 6.15. Enlargement of Figure 6.14, between 90 and 165 seconds, where a grade of 2.5% caused truck separation to increase to 24 m (78.7 feet). As the lead vehicle performs a down-shift from 12th to 11th gear, its engine torque drops to 0 Nm (despite driver-intended torque being saturated at max torque), the platooning controller matches the drop to 0 Nm such that the rear vehicle does not encroach. The front vehicle, now in a lower gear, is able to out-accelerate the rear vehicle and maintain speed on the grade. The rear vehicle then performs a 12 to 11th gear down-shift and the gap increases to 24 m.

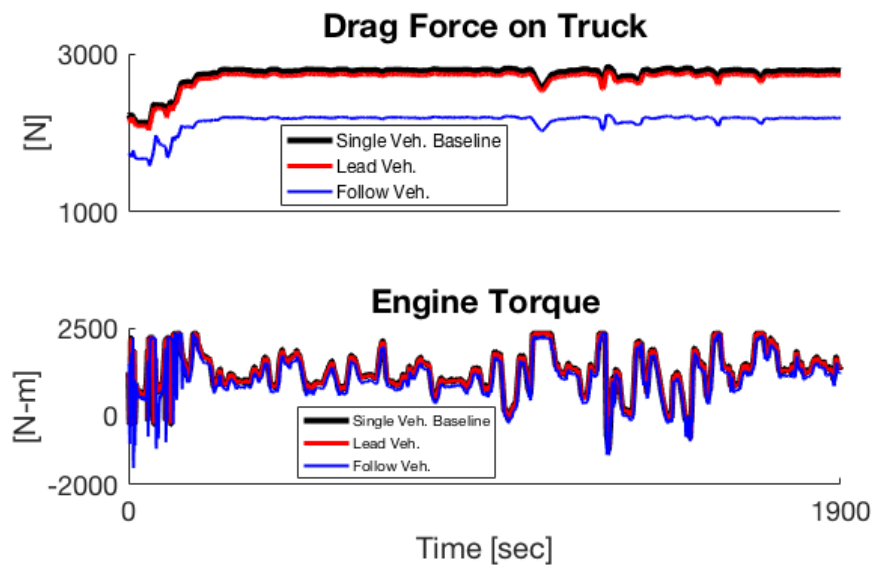


Figure 6.16. Drag force on the rear truck in the platoon is lower throughout the 57.4 km (34 mile) simulated corridor, and thus requires less engine torque to maintain speed than either the lead truck or the single truck baseline.

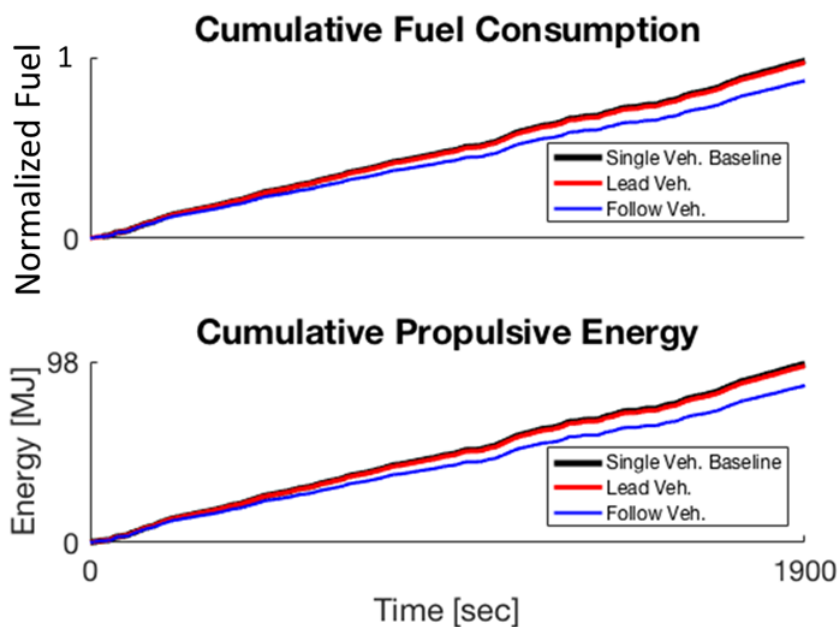


Figure 6.17. Cumulative propulsive energy and fueling for the rear truck in the platoon tracks, with some offset, that of the lead and single truck baseline, and results in a lower cumulative propulsive energy and fuel consumption over I-74.

6.3.5 North-Bound I-69 in Indiana (Heavy Grade)

Interstate 69 in southern Indiana has heavy road grade up to $\pm 5\%$, per Figure 6.18a. A 60 km (37.3 mile) stretch of north-bound I-69 is simulated to understand the impact of higher, real-world road grade on platooning performance and fuel savings.

The simulation begins with an initial speed of 26.8 m/s (60 MPH), then follows the reference speed set by the route's posted speed limit (Figure 6.18d). Per Figure 6.18b, despite the challenging grade, the trucks are never within 14.5m (47.6 ft) of each other. The gap increases above 26 m (85.3 ft) (and never more than 34.2 m or 112 ft) on two occasions. As also shown in Figure 6.18e, and expected, the single and platooning trucks both utilize more engine braking to track the reference speed on this route than on I-74, most notably during the very low grade (-4 to -5%) sections of the corridor. The lead truck tracks the reference speed well throughout the route, except during a section where the road grade increases from 0% to 5% and speed drops from 26.8 m/s (60 MPH) to 22.4 m/s (50 MPH). This section of road (1600 to 1725 s) is unique on this span of I-69, as this grade increase (uphill) is not preceded by a grade decrease (downhill).

A zoom-in of one of the most challenging sections (1620-1740 s as shown in Figure 6.19) shows where the platoon's separation distance, Figure 6.19c, increases from the set point of 16.7 m (54.8 ft) to 34.2 m (112 ft). In a manner similar to that discussed previously for sustained grades on I-74 in Indiana, as the platoon climbs the nearly 5% grade in Figure 6.19b, the lead vehicle performs a down-shift from 12th to 11th gear (Figure 6.19f), during which time the engine's torque output drops to 0 Nm in Figure 6.19e. The platooning controller, having knowledge of the lead vehicle's engine torque output, conservatively decreases its torque command for the rear vehicle to 0 Nm as the front truck is down-shifting. Next, the rear vehicle performs a down-shift to 11th gear, temporarily dropping the engine provided torque to 0 Nm. Together, these two phenomenon reduces the rear-to-front trucks relative velocity by 0.5 m/s (1.1 MPH) per Figure 6.19d. Both the lead and rear vehicles, now in 11th gear,

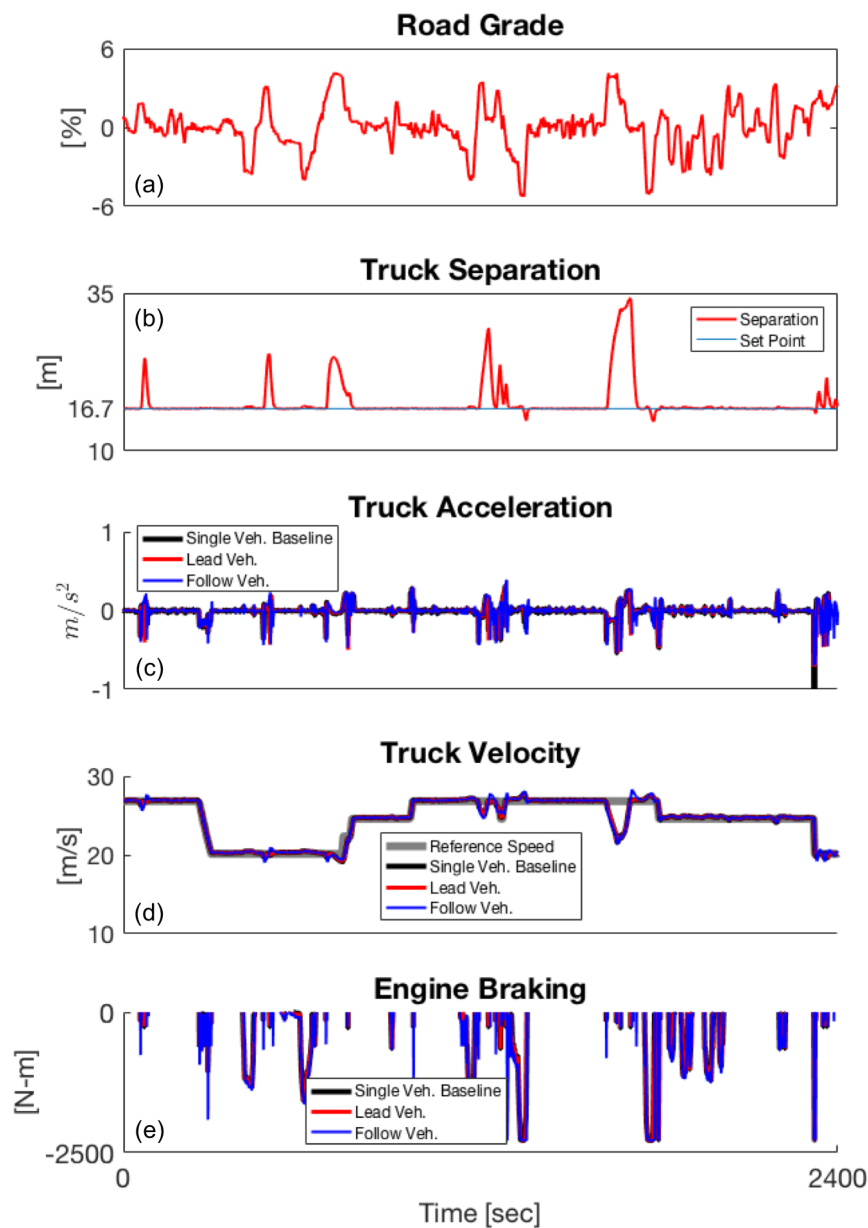


Figure 6.18. I-69 in Indiana presents challenging road grade for platooning ($\pm 5\%$), which results in increased separation distances of up to 34.2 m (112 ft) from the 16.7 m (54.8 ft) setpoint. The reference speed is tracked well throughout the route, except for a section where grade increases to nearly $+5\%$ which is not preceded by a downhill (1620 to 1740 s as shown in Figure 6.19).

saturate engine torque output for the duration of the hill. The rear vehicle is not able to catch up immediately and close the gap until road grade decreases again to 1-2% as the platooning trucks approach the crest of the hill shown in Figure 6.19a.

The drag force and engine torque output for the single vehicle baseline and both the platooning trucks are shown in Figure 6.20. As was also the case for I-74, by maintaining the platoon gap close to the setpoint, drag reductions continue to occur even during challenging grade scenarios.

The platooning trucks require less propulsive energy and fuel consumption to complete the 60.0 km (37.3 mile) corridor, as shown in Figure 6.21. As summarized in Table 6.7, the simulated single truck baseline requires 101.2 MJ of propulsive energy. The platoon averages fuel reduction of -3.71% and propulsive energy of 96.87 MJ (-4.28%), with the front truck in the platoon saving 0.77% fuel and the rear truck saving 6.65%. Fuel savings from platooning on this route are lower than both Indiana's I-74 and the flat-ground highway speed simulations.

Table 6.7. Summary of predicted fuel and energy consumption over a 60.0 km (37.3 mile) section of I-69 in Indiana of the platooning Class 8 trucks relative to the single Class 8 truck baseline. The corridor's speed limit is used as the speed reference, with an average speed of 24.5 m/s (54.8 MPH).

Simulation	%Δ from	Cumul.	%Δ from
Avg. Speed = 24.5 m/s	Baseline	Energy	Baseline
Single Class 8 Truck	-	101.2 MJ	-
Platoon: Lead	-0.77%	100.31 MJ	-0.88%
Platoon: Rear	-6.65%	93.43 MJ	-7.68%
Platoon Avg.	-3.71%	96.87 MJ	-4.28%

Platooning trucks on I-69 are simulated at a higher average speed to understand the trade-off between average vehicle speed and fuel savings from platooning. The

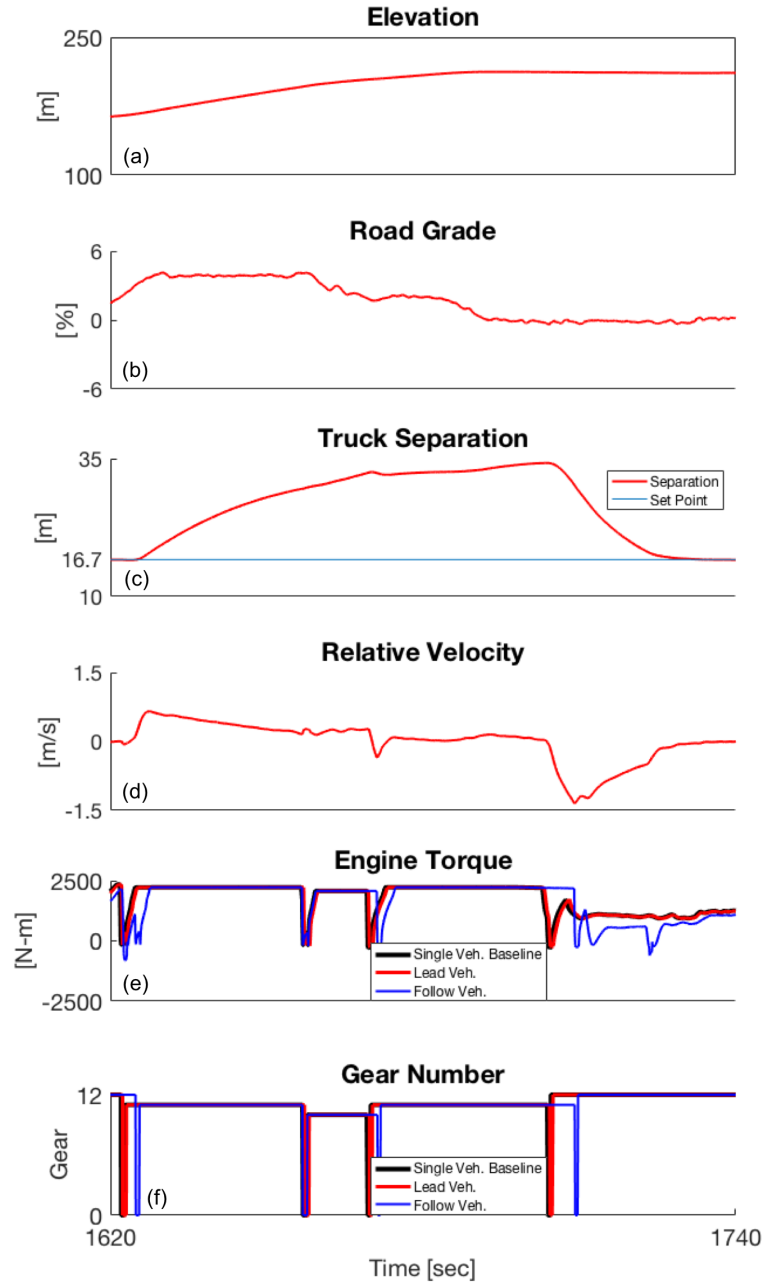


Figure 6.19. A zoom-in from Figure 6.18, where the platooning gap increases to 34.2 m (112 ft) due to a limitation of the platooning controller, namely uncoordinated down-shift events where the lead vehicle out-paces the rear vehicle while climbing the hill. The rear vehicle is unable to gain relative speed on the front vehicle until the trucks near the top of the hill (grade=1-2%) and grade decreases.

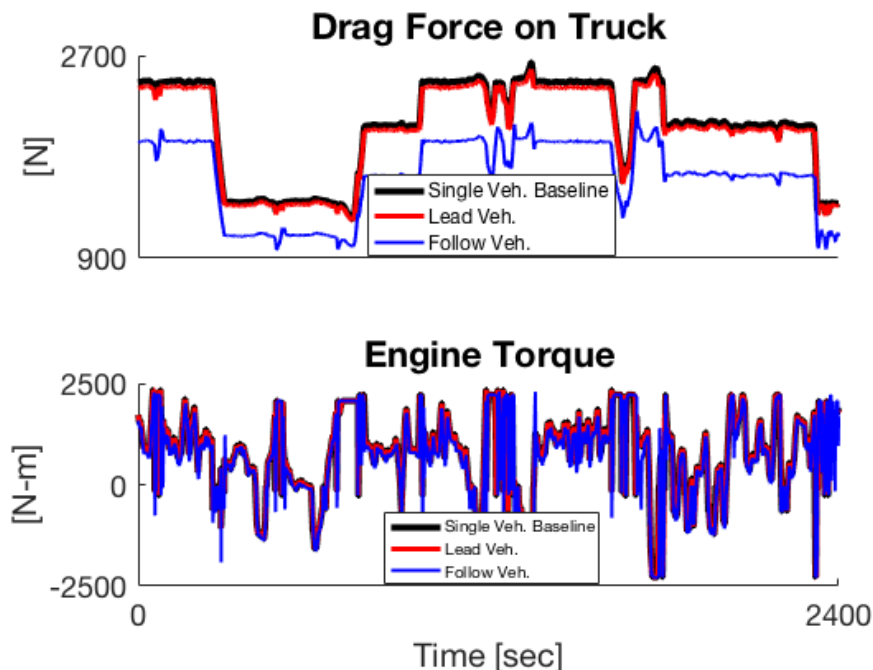


Figure 6.20. Although drag forces on both the lead and rear platooning trucks are lower than the single vehicle baseline throughout the 60.0 km (37.3 mile) corridor, engine torque output does not have a noticeable difference as frequent torque saturation is necessary to climb the high (nearly 5%) grades.

fuel consumption and cumulative propulsive energy summary from simulation of platooning trucks on I-69 at higher average speed of 28.2 m/s (63.1 MPH) are shown in Table 6.8. At higher speeds the trucks' engines saturated at the torque curve more frequently, and the average gap distance increased from 17.7 m (58.1 ft) to 19.4 m (63.6 ft), with the maximum gap increasing from to 34.2 m (112 ft) to 41.1 m (134.8 ft).

As is shown for the flat ground (no grade), I-74 (moderate grade), and here on I-69 (heavy grade) simulations, aerodynamic force increases as a function of velocity squared and thus more fuel is saved through platooning at higher speeds. On I-69, traveling at a faster speed improved the platoon average fuel savings from 3.71% (24.5 m/s) to 4.17% (28.2 m/s).

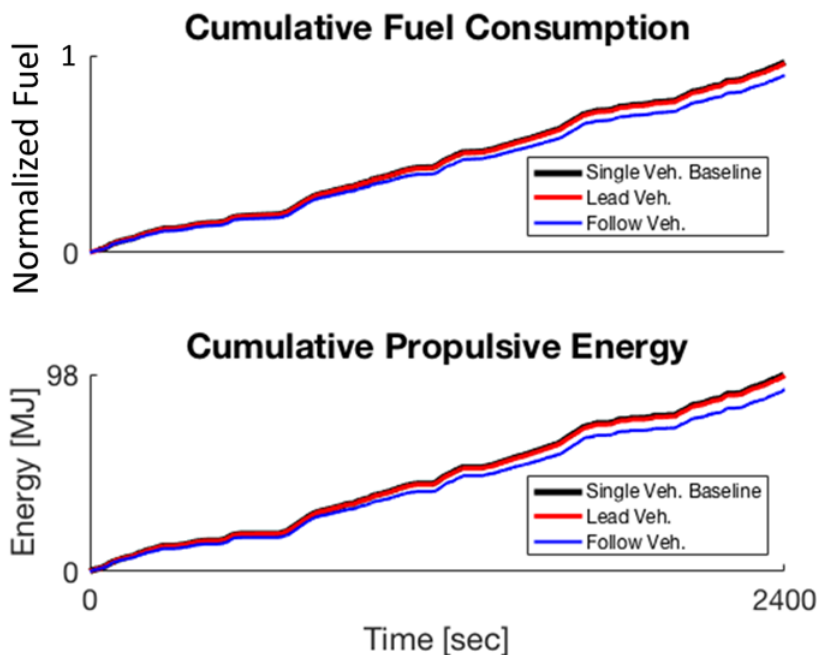


Figure 6.21. The simulated platooning Class 8 trucks do not save as much fuel on I-69 as on Indiana's I-74 or the flat-ground highway speed simulations.

Table 6.8. Summary of predicted fuel and energy consumption over a 60.0 km (37.3 mile) section of I-69 in Indiana of the platooning Class 8 trucks relative to the single Class 8 truck baseline with a higher average speed of 28.2 m/s (63.1 MPH).

Simulation	% Δ from Baseline	Cumul. Energy	% Δ from Baseline
Avg. Speed = 28.2 m/s			
Single Class 8 Truck	-	110.9 MJ	-
Platoon: Lead	-0.77%	109.96 MJ	-0.85%
Platoon: Rear	-7.57%	101.54 MJ	-8.44%
Platoon Avg.	-4.17%	105.75 MJ	-4.64%

6.3.6 Platoon-enabled Fuel Savings - Impact of Speed & Grade

The fuel savings from decreased aerodynamic drag on a per-mile basis through platooning is calculated per Equation (6.4), and normalized relative to the higher speed flat ground fuel savings. Flat ground platooning results in a fuel savings of 0.70 per-mile at slower speed (24.5 m/s, 54.8 MPH), increasing to 1.00 per-mile at higher speeds (28.6 m/s, 64 MPH). Steady-state platooning on a constant 1% grade at 28.6 m/s (64 MPH) provides the same absolute fuel savings as that of flat ground, 1.00 per-mile. Steady-state downhill (-3% grade) platooning shows no fuel savings, as fuel is not consumed while engine braking. On I-74 (moderate grade) with a higher average speed of 28.3 m/s (63.3 MPH), aerodynamic fuel savings are 0.92 per-mile but the savings reduce to 0.66 per-mile when average speed decreases to 24.5 m/s (54.8 MPH). Platooning on I-69 (heavy grade) following the route's speed limit with a slower average speed of 24.5 m/s (54.8 MPH) results in an aerodynamic fuel savings of 0.54 per-mile. Fuel savings increase to 0.65 per-mile on I-69 when the average trip speed is increased to 28.2 m/s (63.1 MPH).

$$Aero\ Fuel\ Savings = \frac{Baseline[kg] - PlatoonAvg[kg]}{Distance[miles]} \quad (6.4)$$

These per-mile fuel savings are captured together in Figure 6.22. As shown, absolute, per-mile, platooning-enabled fuel savings are higher when the platoon traverses the same route at a higher speed as aerodynamic drag approximately increases with velocity squared. As the road grade becomes more aggressive (higher root mean square (RMS) grade), the absolute fuel savings decrease, for two reasons.

First, despite having roughly the same average speed for the flat ground, I-74, and I-69 corridors, the speed profiles and subsequent drag forces are different for these routes. For example, a single truck on flat ground at 28.6 m/s (64 MPH) experiences a drag force of 2,785 N, while a single truck on I-74 is unable to maintain constant speed on the nearly 3% grade, e.g. at 1,100 s in Figure 6.14d, resulting in speed decreases from 28.6 m/s (64 MPH) to 27.3 m/s (61 MPH) and drag decreases from 2,785 N

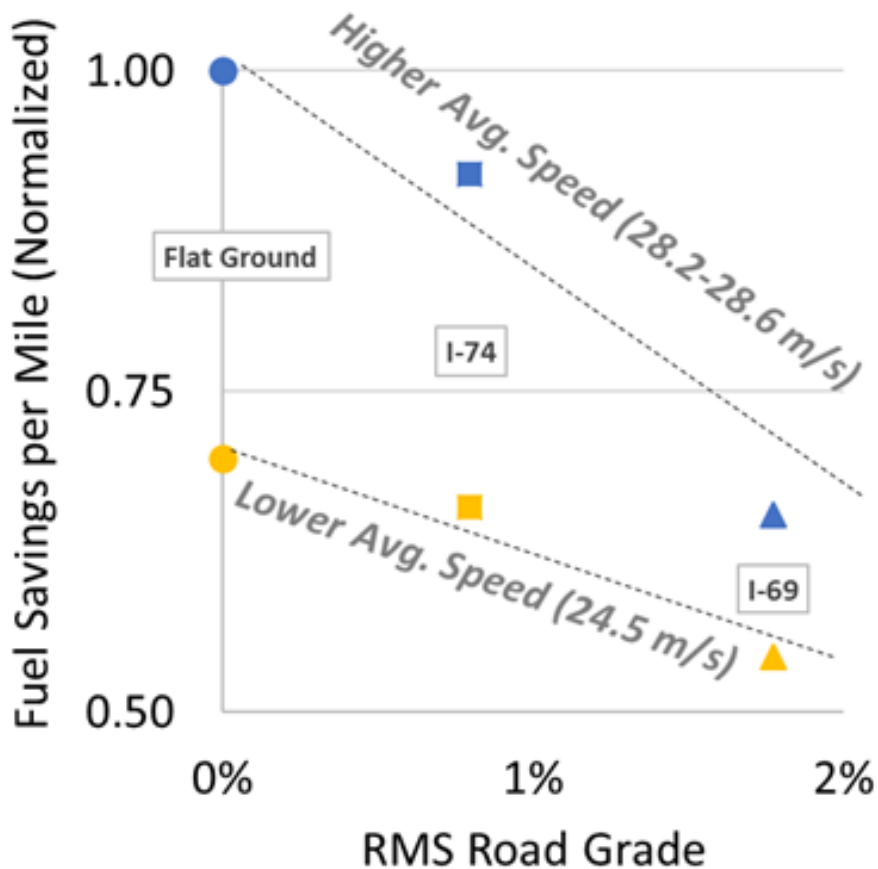


Figure 6.22. The aerodynamic fuel savings on a per-mile basis as calculated per Equation (6.4), normalized to the higher speed I-69 fuel consumption, for high and low average speed platooning on flat ground, I-74 (moderate grade), and I-69 (heavy grade) versus the RMS grade of the route.

to 2,550 N. As a result of different speed profiles and drag forces over the corridors, aerodynamic drag's contribution to single truck fuel consumption (per Figure 6.23) decreases from 0.62 per-mile on flat ground to 0.51 per-mile on the moderately graded I-74, leaving less absolute aerodynamic drag available to be reduced (and less fuel saved) through platooning while on grade. Second, aerodynamic benefits during coasting on downhill sections do not have a direct impact on fuel consumption as i) the engine is not fueling while engine braking (Figure 6.13d&f), and ii) any kinetic energy

benefits from potential increased downhill speeds are not realized on the subsequent uphill since the truck cannot exceed the reference speed (Figure 6.14d). As a result there is less time available during a more aggressively graded route to save fuel via platooning because of the longer amount of time spent on downhills during which time no fuel savings is possible. Taken together, more aggressively graded routes result in lower absolute fuel savings due to reductions in truck speed during uphill sections (lower drag forces to reduce via platooning), and more time spent on downhill sections (generally no fuel saving via platooning).

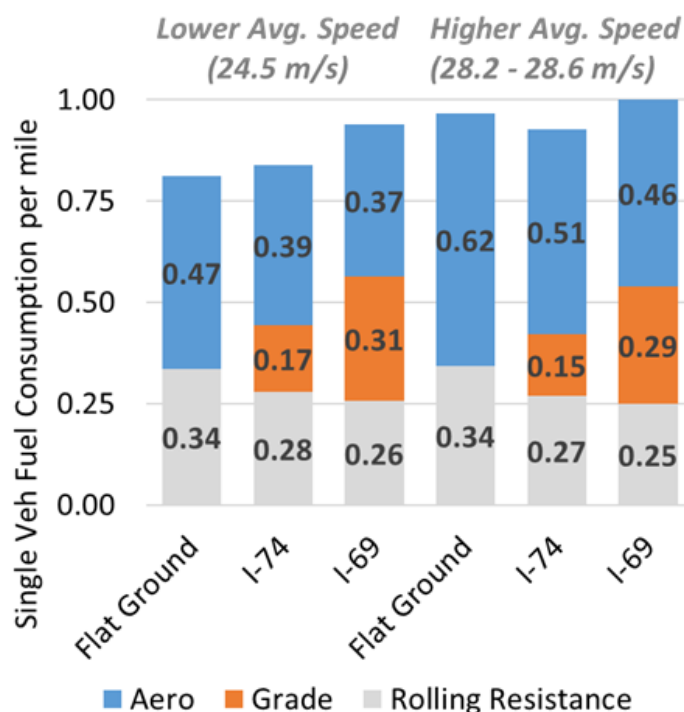


Figure 6.23. Single vehicle baseline: Composite fuel consumption breakdown (propulsive torque use) for the corridors at both lower and higher average speeds, normalized to the higher speed I-69 fuel consumption. Despite having the same average speed, the velocity profiles are different between the routes (e.g. constant speed for flat ground, non-constant for I-74 per Figure 6.14d), and subsequently have different drag forces and contributions for aerodynamic drag.

7. SUMMARY AND FUTURE WORK

7.1 Summary

7.1.1 iEGR & EEVO as Aftertreatment Warm-Up Air Handling Strategies

Both EEVO and iEGR were considered as strategies to improve aftertreatment thermal performance by increasing exhaust gas temperatures through manipulation of air handling through conventional actuators (VGT, EGR) and flexible valvetrain operation. Steady-state test results showed that iEGR yielded higher exhaust temperatures at a lower fuel penalty than EEVO. When applied to the loaded idle portions of the HD-FTP, the air handling strategy of iEGR reduced predicted tailpipe NO_x emissions by 7.9% over the thermal management baseline with a fuel penalty of 2.1%. Considering that the thermal management baseline is the state of the art for aftertreatment warmup and reducing tailpipe NO_x, iEGR provides a NO_x reduction that is not currently achievable.

7.1.2 Cylinder Deactivation as an Aftertreatment Stay-Warm Strategy

CDA applied at idle regions is a viable stay-warm alternative to the state of the art thermal management baseline. Airflow through the engine is reduced by roughly half with half-engine CDA, allowing for reduced pumping losses and a lower AFR for both improved fuel consumption and exhaust temperature. The reduction in exhaust flow eliminates CDA as a viable aftertreatment warm-up strategy, but the increased exhaust temperature showed stay-warm benefits. Half-engine CDA applied at idle regions after 600 seconds into the cold start HD-FTP reduced fuel consumption from the thermal management cycle by 3.0%. An additional 0.4% fuel benefit comes from

deactivating cylinders up to 3 bar BMEP for a total of 3.4% fuel savings. CDA up to 3 bar BMEP is an effective thermal management stay-warm tool, and outperforms the state of the art 6-cylinder thermal management cycle from a fuel consumption standpoint. Compressor surge can be instigated by the reduction in demanded airflow of CDA when applied after high loads.

7.1.3 Model-Based Compressor Surge Avoidance Algorithm for IC Engines Utilizing Cylinder Deactivation During Motoring Conditions

CDA has benefits to both exhaust thermal management and fuel consumption. The transition zone from high loads (high IMP) to motoring requires special attention when implementing CDA as compressor surge may occur and possibly damage the turbomachinery. This work highlighted two methods for compressor surge avoidance: i) a fixed, calibratable time delay and ii) an algorithm with model based prediction of future compressor outlet conditions and staged cylinder deactivation. The surge avoidance algorithm, which relies on a physics based prediction of IMP and both future compressor and engine air mass flow, successfully avoided compressor surge during motoring via implementation of staged cylinder deactivation. This work found the following key conclusions

- (1) Deep decel compressor surge, while not typically a problem on diesel engines, can be instigated by deactivating cylinders during certain high IMP conditions and may damage the turbomachinery
- (2) The increase in IMP is proportional to the decrease in airflow demanded, or the ratio of the number of deactivated cylinders to the number of currently active cylinders.
- (3) IMP increases must be considered when deactivating cylinders because they may push the operating condition into surge

- (4) Staged cylinder deactivation mitigates the magnitude of the IMP increase and airflow decrease, and in so doing enables surge to be avoided via a robust, model-based methodology

7.1.4 Road Grade Quality Necessary for Accurate Fuel Consumption & Performance Predictions in Class 8 Truck Simulation

Comm road grade data ($R^2=0.992$) provided the best match to the truth reference LiDAR over a 5,432 m span of US 231, although Comm has limitations (demonstrated here for US 231 and I-69 in Indiana) in that the accuracy and availability of this grade data varies. Integrating the velocity output of an IMU provided the second best match ($R^2=0.972$) to the truth reference, while using the pitch measurement from the same IMU produced the third best ($R^2=0.958$). The single antenna GPS method of grade estimation ($R^2=0.122$) was a poor match to the reference. The quality of the road grade data used in simulation of a Class 8 truck has a significant an impact on both the vehicle and powertrain dynamics and predicted fuel consumption.

This work found the following key conclusions:

- (1) Average grade over a corridor provided a useful comparison of grade data to a reference baseline, since RMS does not distinguish between negative and positive grades.
- (2) The fuel penalty to climb a grade is greater than the fuel benefit of descending a grade, as evidenced by a corridor relative error in mean grade from baseline versus fuel consumption trade-off in Figure 5.16.
- (3) Small absolute errors in grade data (.248 difference in mean percent grade) for use in a simulation framework may still produce up to a 17.4% error in predicted fuel consumption as a result of average road grade impacts (per above).
- (4) Road grade obtained from a GPS system without a base station produced an unreliable estimate of grade.

- (5) Integrating IMU velocity provided a better estimate of road grade than the IMU pitch, which was found to be susceptible to error from suspension movement.
- (6) Both the Comm grade data (when available and accurate) and integrated IMU road grade data result in a simulated Class 8 truck model fuel consumption predictions within 2.5% of those simulated with truth reference grade data.

7.1.5 Capturing the Impact of Speed, Grade, and Traffic on Class 8 Truck Platooning

Platooning class 8 trucks save fuel due to reduced aerodynamic drag, and in so doing result in both the lead and follow truck requiring less engine power to maintain desired vehicle speeds. A novel simulation framework that includes high fidelity class 8 truck models, a two-truck platooning controller provided by Peloton Technology, accurate road grade data, and real-time traffic speed data was used to understand the impact of average speed and grade on the fuel savings and robustness of a production-intent two-trucks platooning system. Key findings include:

- (1) Platooning (gap = 11 m) on flat ground at higher speeds (28.6 m/s, 64 MPH) fuel savings are 7.45% for the platoon, which agrees with experimental data in the literature. With a gap setpoint of 16.7 m (54.8 ft), fuel savings decrease to 6.90% at the same higher speed. Platooning with a lower average speed (24.5 m/s, 54.8 MPH) enables 5.54% platoon-averaged savings compared to the single vehicle baseline. Aerodynamic drag increases with speed, and as such, a larger absolute drag force reduction is possible on each truck in a platoon. This results in higher relative fuel savings via platooning as speed is increased.
- (2) Absolute aerodynamic fuel savings (normalized) are 1.00 per-mile when traveling at 28.6 m/s (64 MPH) on both flat ground and uphill (1% grade) with a 16.7 m (54.8 ft) gap setpoint, though relative fuel savings decrease with the addition of road grade (from a platoon-averaged fuel savings of 6.90% on flat ground

to 4.94% on a 1% grade) because overall fuel consumption increases when on grade (Figure 6.23). Downhill scenarios that require engine braking (such as -3% grade), or coasting, do not see fuel savings through platooning as the engine is not consuming fuel per Figure 6.13f, and as a result drag reductions via platooning do not reduce the engine propulsive effort.

- (3) On a moderately graded section of I-74, at a higher average speed of 28.3 m/s (63.3 MPH), platooning reduces the platoon-averaged fuel consumption by 6.18%, a reduction compared to flat road operation, due to a larger fraction of truck operation occurring on downhill sections, during which time no fuel savings is possible, per (2), and because the speed decreases during the uphill sections. The platooning controller prevented vehicle gap to drop below the 16.7 m (54.8 ft) setpoint at any point in the route, per Figure 6.14b. The gap held at/near the setpoint except for two brief, and modest (<7 m) increases resulting from uncoordinated down-shifts, such as those shown in Figure 6.16. Consistent with (1), platoon-average fuel savings decrease to 5.03% when the trucks traverse the route at a slower average speed of 24.5 m/s (54.8 MPH).
- (4) On a heavily graded section of Indiana's I-69, at a slower average speed of 24.5 m/s (54.8 MPH), platooning reduces the platoon-averaged fuel consumption by 3.71%, a further reduction compared to both flat road operation and I-74 as (per (2)) coasting and engine braking comprise an even larger fraction of truck operation (Figure 6.18e). Despite the challenging grade, the platooning controller maintains gap distance within 17.5 m (57.4 ft) of the 16.7 m (54.8 ft) setpoint, albeit with several brief increases in gap due to uncoordinated shifting (such as Figure 6.19). The platoon-average fuel savings increase to 4.17% when the trucks travel at a higher average speed of 28.2 m/s (63.1 MPH), consistent with (1).

7.2 Future Work

7.2.1 Air Handling on VVA Engine

Aftertreatment Thermal Management Strategies

The warm-up air handling strategies of iEGR and EEVO and stay-warm strategy of CDA are being applied to other relevant drive-cycles, such as the city bus routes and the Class 8 truck drayage cycle. The drayage drive-cycle simulates a Class 8 truck near a harbor port, where a significant (>80%) amount of time is spent at or around idle conditions which presents a thermal management stay-warm issue for the aftertreatment system. Work on this is progressing with colleagues as the focus of my PhD program shifts towards the NEXTCAR project.

Compressor Surge

Work in this area should progress towards an improvement or optimization of the amount of time spent at high airflow, high speed motoring. The controller's cost function should seek to minimize cool airflow as quickly as possible. One method to achieve this is by manipulating volumetric efficiency, η_{vol} , in 6 cylinder operation by means of variable valve actuation. The goal would be to avoid the IMP increase of CDA by continuing in 6 cylinder operation with ever decreasing η_{vol} until fresh airflow is at or near zero. This could allow for a more rapid decrease in fresh airflow without the piece-wise action of staged CDA.

The compressor surge avoidance algorithm could be applied to fired engine operation, with some modification. The surge detection algorithm could also be applied to inform actuation of a "blow off" valve, which releases intake tract pressure (mass) to open atmosphere or recirculates it to the air inlet.

7.2.2 NEXTCAR Project - Connected & Automated Class 8 Trucks

The simulation framework developed by the author, shown in Chapters 5 & 6, will be used to study connectivity-enabled fuel saving algorithms on Indiana corridors. Drive-cycles (speed and torque patterns) for engine testing in the new Test Cell #2 should be generated from the simulation framework to confirm that the vehicle model accurately estimates/captures i) engine transient torque response and ii) fuel consumption. If it is determined that the simulated vehicle's engine model does not accurately capture transient torque response, the engine testbed should be reconfigured to allow for real-time hardware-in-the-loop (HIL), with the engine in the loop instead of the engine model.

There are three connectivity-enabled concepts which combined are predicted to meet the 20% fuel savings goal of the NEXTCAR project, detailed in Figure 7.1. As part of concept 3, coordinated shifting should be studied and implemented in simulation to address limitations of the current platooning controller, which were detailed in Chapter 6.

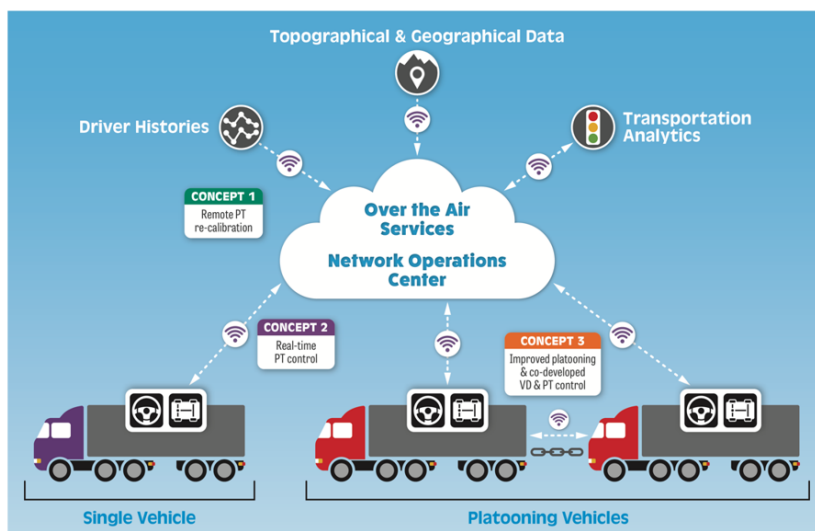


Figure 7.1. All 3 concepts utilize connectivity to enable additional fuel savings, concept 3 involves improved platooning.

The final stage (2019-2020, Year 3) of this project involves using the candidate control algorithms, developed in both simulation and drive-cycle testing on the new engine testbed in Test Cell #2, and testing them on trucks, shown in Figure 7.2. Experimental truck test results should be compared to those of the simulation and engine testbed to understand what, if any, differences in performance and fuel consumption exist.



Figure 7.2. The final stage of the NEXTCAR project involves showcasing 20% fuel consumption benefit on two Peterbilt 579 trucks in a platoon on-road in Indiana.

REFERENCES

REFERENCES

- [1] A. Taylor. *Test Cell Set-Up to Enable Drive-Cycle Testing of a Variable Valve Actuation Enabled Camless Diesel Engine*. M.s., Purdue University, 2016.
- [2] United States Environmental Protection Agency. *Inventory of U.S. Greenhouse Gas Emissions and Sinks 1990-2015*. Technical report, United States Environmental Protection Agency, 2017.
- [3] United States Department of Transportation Federal Highway Administration. *Freight Quick Facts Report 2016*. Technical report, United States Department of Transportation, 2016.
- [4] United States Department of Transportation. *Beyond Traffic: 2045 Final Report*. Technical report, United States Department of Transportation, 2017.
- [5] Federal Highway Administration. *Federal Highway Administration Table VM-1 and American Public Transit Association's Public Transportation Fact Book -*, 2015.
- [6] Environmental Protection Agency (EPA). *Nitrogen oxides (NOx), why and how they are controlled*. *Epa-456/F-99-006R*, (November):48, 1999.
- [7] NASA Health and Air Quality Applied Science Team. *NASA Aura Satellite Data: Atmospheric NOx Concentrations in 2005 and 2015 -*, 2017.
- [8] United State Environmental Protection Agency. *United States Environmental Protection Agency Green Book -*, 2017.
- [9] M. Brauer, G. Freedman, J. Frostad, A. van Donkelaar, Randall V. M., F. Dentener, R. van Dingenen, K. Estep, H. Amini, J. Apte, K. Balakrishnan, L. Barrera, D. Broday, V. Feigin, S. Ghosh, P. Hopke, L. Knibbs, Y. Kokubo, Y. Liu, S. Ma, L. Morawska, J. Sangrador, G. Shaddick, H. Anderson, T. Vos, M. Forouzanfar, R. Burnett, and A. Cohen. *Ambient air pollution exposure estimation for the global burden of disease 2013*. *Environmental Science & Technology*, 50(1):79–88, 2016. PMID: 26595236.
- [10] J. McCarthy, E. Dykes, and E. Ngan. *Aftertreatment System Performance of a Fuel Reformer, LNT and SCR System Meeting EPA 2010 Emissions Standards on a Heavy-Duty Vehicle*. *SAE*, 2010.
- [11] C. Sharp, C. Webb, S. Yoon, M. Carter, and C. Henry. *Achieving Ultra Low NOx Emissions Levels with a 2017 Heavy-Duty On-Highway TC Diesel Engine - Comparison of Advanced Technology Approaches*. *SAE International Journal of Engines*, 10(4):2017–01–0956, 2017.

- [12] D. Stanton. Systematic development of highly efficient and clean engines to meet future commercial vehicle greenhouse gas regulations. *SAE Int. J. Engines*, 6:1395–1480, 09 2013.
- [13] DieselNet Technology Guide. Heavy-Duty Diesel Engines with Aftertreatment , 2016.
- [14] M. Naseri, S. Chatterjee, M. Castagnola, H. Chen, J. Fedeyko, H. Hess, and J. Li. Development of SCR on Diesel Particulate Filter System for Heavy Duty Applications.
- [15] J. Kim and C. Bae. Emission reduction through internal and low-pressure loop exhaust gas recirculation configuration with negative valve overlap and late intake valve closing strategy in a compression ignition engine. *International Journal of Engine Research*, 0(0):1468087417695897, 2017.
- [16] D. Gosala, A. Ramesh, C. Allen, M. Joshi, A. Taylor, M. VanVoorhis, G. Shaver, L. Farrell, E. Koeberlein, J. McCarthy, and D. Stretch. Diesel engine aftertreatment warm-up through early exhaust valve opening and internal exhaust gas recirculation during idle operation. *International Journal of Engine Research*, page 146808741769400, 2017.
- [17] K. Blumenroder, G. Buschmann, J. Kahrstedt, A. Sommer, and O. Maiwald. Variable valve trains for passenger car diesel engines-potentials, limits and ways of realisation. *FORTSCHRITT BERICHTE-VDI REIHE 12 VERKEHRSTECHNIK FAHRZEUGTECHNIK (Internationales Wiener Motorensymposium)*, 622(2):280, 2006.
- [18] Anand Nageswaran Bharath, Yangdongfang Yang, Rolf D Reitz, and Christopher Rutland. Comparison of Variable Valve Actuation , Cylinder Deactivation and Injection Strategies for Low-Load RCCI Operation of a Light Duty Engine. 2015.
- [19] L. Roberts, M. Magee, G. Shaver, A. Garg, J. McCarthy, E. Koeberlein, E. Holloway, R. Shute, D. Koeberlein, and D. Nielsen. Modeling the impact of early exhaust valve opening on exhaust aftertreatment thermal management and efficiency for compression ignition engines. *International Journal of Engine Research*, 16(6):773–794, 2015.
- [20] S. Davis, S. Williams, R. Boundy, and S. Moore. 2015 Vehicle Technologies Market Report. Technical report, 2015.
- [21] Sajit Pillai, Julian LoRusso, and Matthew Van Benschoten. Analytical and Experimental Evaluation of Cylinder Deactivation on a Diesel Engine. *SAE Technical Paper*, 2015.
- [22] C. Schenk, J. Sanchez, C. Moulis, and C. Laroo. HD Diesel Thermal Management Improvement EPA. *SAE Technical Paper*, 2007.
- [23] X. Lu, C. Ding, A. Ramesh, G. Shaver, E. Holloway, J. McCarthy, M. Ruth, E. Koeberlein, and D. Nielsen. Impact of cylinder deactivation on active diesel particulate filter regeneration at highway cruise conditions. *Frontiers in Mechanical Engineering*, 1(9), 2015.

- [24] M. Joshi, D. Gosala, C. Allen, K. Vos, M. VanVoorhis, A. Taylor, G. Shaver, J. McCarthy, D. Stretch, E. Koeberlein, and L. Farrell. Reducing Diesel Engine Drivecycle Fuel Consumption Through Use of Cylinder Deactivation for Aftertreatment Component Temperature Maintenance During Idle Operating Conditions. *Frontiers in Mechanical Engineering*, 2017.
- [25] C. Schenk and P. Dekraker. Potential Fuel Economy Improvements from the Implementation of cEGR and CDA on an Atkinson Cycle Engine. (1), 2017.
- [26] M. Wilcutts, J. Switkes, M. Shost, and A. Tripathi. Design and Benefits of Dynamic Skip Fire Strategies for Cylinder Deactivated Engines. *SAE International Journal of Engines*, 2013.
- [27] SAE IC Powertrain Steering Committee. Turbocharger nomenclature and terminology. *SAE International*.
- [28] D. G. Shepherd. *Principles of turbomachinery / [by] D. G. Shepherd*. Macmillan New York, 1956.
- [29] J. Andersen, F. Lindstrm, and F. Westin. Surge definitions for radial compressors in automotive turbochargers. *SAE Int. J. Engines*, 1:218–231, 04 2008.
- [30] J. Galindo, F. Arnau, A. Tiseira, R. Lang, H. Lahjaily, and T. Gimenes. Measurement and modeling of compressor surge on engine test bench for different intake line configurations. In *SAE Technical Paper*. SAE International, 04 2011.
- [31] R. Keller, J. Scharrer, and P. Mosher. Performance turbocharger failure analysis - causes and solutions. In *SAE Technical Paper*. SAE International, 12 1994.
- [32] H. Shirai, H. Nakada, A. Matsunaga, and H. Tominaga. An application of a model-prediction-based reference modification algorithm to engine air path control. *SAE Int. J. Commer. Veh.*, 10:291–298, 03 2017.
- [33] G. Theotokatos and N.P. Kyrtatos. Diesel engine transient operation with turbocharger compressor surging. In *SAE Technical Paper*. SAE International, 03 2001.
- [34] C. Wang, C. Shao, and Y. Han. Centrifugal compressor surge control using nonlinear model predictive control based on ls-svm. In *2010 3rd International Symposium on Systems and Control in Aeronautics and Astronautics*, pages 466–471, June 2010.
- [35] K. Hansen, P. Jorgensen, and P. Larsen. Experimental and theoretical study of surge in a small centrifugal compressor. *J. Fluids Eng*, 103(3):391–395, 1981.
- [36] B. Kerres, V. Nair, A. Cronhjort, and M. Mihaescu. Analysis of the turbocharger compressor surge margin using a hurst-exponent-based criterion. *SAE Int. J. Engines*, 9:1795–1806, 04 2016.
- [37] C. D. Rakopoulos, C. N. Michos, and E. G. Giakoumis. Study of the transient behavior of turbocharged diesel engines including compressor surging using a linearized quasi-steady analysis. In *SAE Technical Paper*. SAE International, 04 2005.

- [38] R. Dehner, A. Selamet, P. Keller, and M. Becker. Prediction of surge in a turbocharger compression system vs. measurements. *SAE Int. J. Engines*, 4:2181–2192, 05 2011.
- [39] J. Pinsley, G. Guenette, A. Epstein, and E. Greitzer. Active stabilization of centrifugal compressor surge. *J. Turbomach*, 113(4):723–732, 1991.
- [40] F. Bozza, V. Bellis, L. Teodosio, and A. Gimelli. Numerical analysis of the transient operation of a turbocharged diesel engine including the compressor surge. *Proceedings of the Institution of Mechanical Engineers, Part D: Journal of Automobile Engineering*, 227(11):1503–1517, 2013.
- [41] H. Bae, J. Ryu, and J. Gerdes. Road Grade and Vehicle Parameter Estimation for Longitudinal Control Using GPS. *IEEE Intelligent Transportation Systems Conference Proceedings*, pages 166–171, 2001.
- [42] K. Zhang and C. Frey. Road Grade Estimation for On-Road Vehicle Emissions Modeling Using LIDAR Data. *Proceedings, Annual Meeting of the Air & Waste Management Association*, (2005):1–22, 2005.
- [43] E. Wood, A. Duran, E. Burton, J. Gonder, and K. Kelly. EPA GHG Certification of Medium- and Heavy-Duty Vehicles : Development of Road Grade Profiles Representative of US Controlled Access Highways. (May), 2015.
- [44] N. Kim, D. Karbowski, and A. Rousseau. A Modeling Framework for Connectivity and Automation Co-simulation. *SAE Tech. Pap. 2018-01-0607*, pages 1–10, 2018.
- [45] D. Shen, D. Karbowski, and A. Rousseau. Fuel Efficient Speed Optimization for Real-World Highway Cruising. *SAE Tech. Pap. 2018-01-0589*, pages 1–12, 2018.
- [46] M. Zulkefli, P. Mukherjee, Y. Shao, and Z. Sun. Evaluating Connected. *ASME*, (December 2016):12–17, 2018.
- [47] Y. Shao, M. Zulkefli, and Z. Sun. Vehicle and powertrain optimization for autonomous and connected vehicles. *ASME*, (September 2017):19–23, 2017.
- [48] K. Kim and D. Cho. A multi-vehicle platoon simulator. *SAE Tech. Pap. 2000-05-0363*, pages 1–9, 2000.
- [49] B. Hosking and J. McPhee. Powertrain Modeling and Model Predictive Longitudinal Dynamics Control for Hybrid Electric Vehicles. *SAE Tech. Pap. 2018-01-0996*, pages 1–10, 2018.
- [50] S. Anderson, C. Ciesla, D. Carey, and S. Raja. A Powertrain Simulation for Engine Control System Development. *SAE Tech. Pap. 962171*, 1996.
- [51] D. Assanis, Z. Filipi, S. Gravante, D. Grohnke, X. Gui, L. Louca, G. Rideout, J. Stein, and Y. Wang. Validation and Use of SIMULINK Integrated , High Fidelity , Engine-In-Vehicle Simulation of the International Class VI Truck. *SAE Tech. Pap. 2000-01-0288*, (724), 2000.
- [52] J. Andert, F. Xia, S. Klein, D. Guse, R. Savelsberg, R. Tharmakulasingham, M. Thewes, and J. Scharf. Road-to-rig-to-desktop: Virtual development using real-time engine modelling and powertrain co-simulation. *Int. J. Engine Res.*, pages 1–10, 2018.

- [53] I. Johansson, J. Jin, X. Ma, and H. Pettersson. ScienceDirect September using Look-ahead speed planning for vehicle platoons traffic information for vehicle platoons using Look-ahead speed speed planning planning for vehicle platoons using traffic information traffic information. *Transp. Res. Procedia*, 22:561–569, 2017.
- [54] S. Gelbal, S. Cantas, L. Guvenc, and B. Aksun-Guvenc. A Connected and Autonomous Vehicle Hardware-in-the-Loop Simulator for Developing Automated Driving Algorithms. In *2017 IEEE Int. Conf. Syst. Man, Cybern.*, pages 3397–3402, 2017.
- [55] D. Fredette and U. Ozguner. Dynamic Eco-Driving’s Fuel Saving Potential in Traffic : Multi-Vehicle Simulation Study Comparing. *IEEE Trans. Intell. Transp. Syst.*, pages 1–9, 2017.
- [56] A. Taylor, M. Droege, G. Shaver, and D. Bullock. Making the Grade: The Sensitivity of Class 8 Truck Fuel Consumption and Operational Behavior Predictions to Road Grade Data Quality. *IEEE Transactions on Intelligent Transportation Systems*, (TBD), 2018.
- [57] M. Lammert, A. Duran, J. Diez, K. Burton, and A. Nicholson. Effect of Platooning on Fuel Consumption of Class 8 Vehicles Over a Range of Speeds , Following Distances , and Mass. *SAE Commer. Veh.*, pages 626–639, 2014.
- [58] M. Roeth and J. Switkes. Peloton Technology Platooning Test Nov 2013. Technical report, NACFE, 2016.
- [59] C. Ferguson and A. Kirkpatrick. *Internal Combustion Engines, Applied Thermosciences*. Wiley, Colorado State University, USA, 2016.
- [60] R. Ravi, Y. Lin, M. Elbahnasawy, T. Shamseldin, and A. Habib. Bias Impact Analysis and Calibration of Terrestrial Mobile LiDAR System With Several Spinning Multibeam Laser Scanners. *IEEE Transactions on Geoscience and Remote Sensing*, pages 1–15, 2018.
- [61] TomTom. <https://www.tomtom.com/automotive/automotive-solutions/automated-driving/tomtom-advanced-driving-attributes/>, 2018.
- [62] Yahya Akansu. The Determination of Aerodynamic Drag Coefficient of Truck and Trailer Model by Wind Tunnel Tests. *International Journal of Automotive Engineering and Technologies*, 5(2):55–60, 2016.
- [63] Rose Mccallen, Richard Couch, Juliana Hsu, Anthony Leonard, Mark Brady, James Ross, Bruce Storms, J T Heineck, David Driver, James Bell, and Gregory Zilliac. Progress in Reducing Aerodynamic Drag for Higher Efficiency of Heavy Duty Trucks (Class 7-8). Technical report, 1999.
- [64] Indiana Department of Transportation and Purdue University. INDOT Mobility Dashboard interstate historical traffic speed, <http://its.ecn.purdue.edu/mobility/dashboards/profile/index.html>, 2018.
- [65] K. Salari. DOE’s Effort to Improve Heavy Vehicle Fuel Efficiency through Improved Aerodynamics Overview: LLNL-PRES-688057. Technical report, U.S. Department of Energy by Lawrence Livermore National Laboratory, Washington, D.C.

APPENDIX

A. MEAN EFFECTIVE PRESSURES AND THE LOGP-LOGV DIAGRAM

In-cylinder pressure acquisition allows for characterizing the engine cycle through mean effective pressure (MEP) metrics. MEPs represent the mean pressure acting on the piston during that portion of the cycle. The three MEPs of concern in this work are:

- net indicated mean effective pressure (NIMEP)
- gross indicated mean effective pressure (GIMEP)
- pumping mean effective pressure (PMEP)

An example log in-cylinder pressure vs. log cylinder volume plot is shown in Figure A.1 for a clearer explanation of the MEPs. GIMEP is the area of the loop labeled “Gross work” divided by the cylinder displacement. It represents the work done (by or on the piston) during the compression and expansion strokes. PMEP is the area of the loop labeled “Pumping work” divided by the cylinder displacement. This represents the work to pump gas either from the intake manifold into the cylinder, or from the cylinder into the exhaust manifold during the gas exchange process. PMEP is typically less than zero for diesel engines with high pressure EGR. Finally, NIMEP is the sum of the GIMEP and PMEP. Note that a clockwise loop is “positive” while a counter-clockwise loop is “negative” area.

The brake thermal efficiency (BTE) of an engine is a dimensionless parameter that describes how efficient the engine is at converting fuel energy to useful work. It is formulated in Equation (A.1). BTE is considered the most important efficiency metric in comparing engines. When considering the performance of a single engine, the MEP metrics can be utilized to deconstruct the brake thermal efficiency (BTE) of the engine into subcomponents of open cycle efficiency (OCE), closed cycle efficiency (CCE) and mechanical efficiency (ME) for further analysis via Equation (A.2) [12].

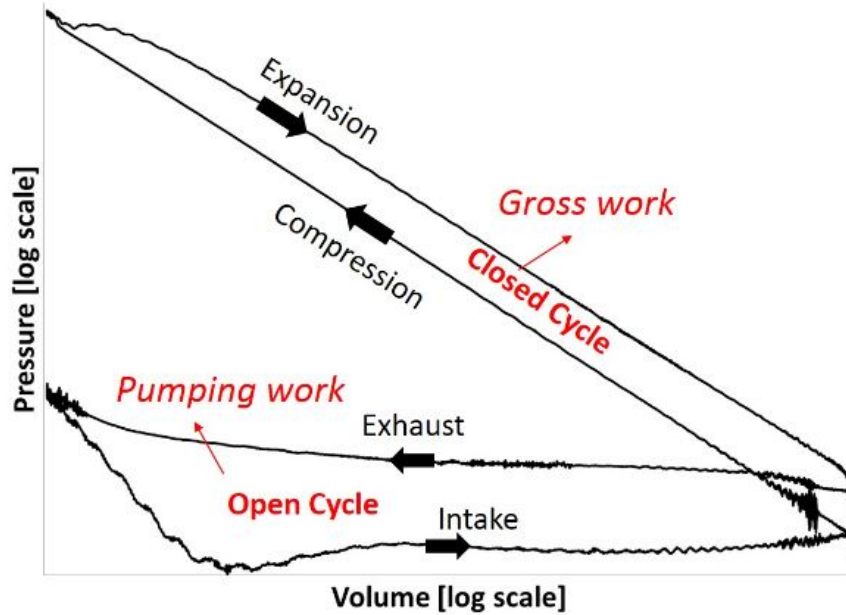


Figure A.1. An example LogP-LogV diagram, for in-cylinder pressure and volume.

The OCE of the engine quantifies the ability of the engine to exchange the charge into the cylinder and exhaust products out of the cylinder. It is defined per Equation (A.3). Factors that affect OCE include turbocharger efficiency, manifold and port design, and volumetric efficiency. The CCE quantifies the efficiency of the combustion and heat transfer processes that occur during the compression and expansion. It is defined per Equation (A.4). The main factors that affect CCE can be generally categorized as combustion efficiency and in-cylinder heat transfer. Finally, ME describes the efficiency of the work transmission of the engine. As shown in Equation (A.6), ME is often back-calculated from BTE using but can also be determined using the brake mean effect pressure (BMEP) of the engine in conjunction with NIMEP. These are the most effective methods of calculating ME when combustion is occurring because the combustion pressure increase can increase friction in the cylinders. However, relative comparisons can also be obtained by using motoring tests to determine frictional losses with different accessory configurations. Numerous factors influence ME, but

among the most prevalent are mechanical friction, accessory loads, and high pressure fuel pump load.

$$BTE = \frac{P_{brake}}{\dot{m}_{fuel} Q_{LHV}} \quad (A.1)$$

P_{brake} is the brake power of the engine (also known as crankshaft power, or the power required to brake the engine), \dot{m}_{fuel} is the fuel flow rate, and Q_{LHV} is the lower heating value of the fuel, which assumes that the latent heat of vaporization of water in the exhaust is not recovered.

$$BTE = OCE \cdot CCE \cdot ME \quad (A.2)$$

$$OCE = \frac{NIMEP}{GIMEP} = 1 - \frac{PMEP}{GIMEP} \quad (A.3)$$

$$CCE = \frac{GIMEP}{\frac{\dot{m}_{fuel} Q_{LHV}}{C \cdot N \cdot V_d}} \quad (A.4)$$

\dot{m}_{fuel} is the fuel flow rate, Q_{LHV} is the lower heating value of the fuel, N is the engine speed, V_d is the displacement of the engine, and C is a constant for unit conversion.

$$BMEP = \frac{P_{brake}}{C \cdot V_d \cdot N} \quad (A.5)$$

where P_{brake} is the brake power of the engine, V_d is the engine displacement, N is the engine speed, and C is a constant for unit conversion.

$$ME = \frac{BTE}{OCE \cdot CCE} = \frac{BMEP}{NIMEP} \quad (A.6)$$

VITA

VITA

Education:

Purdue University, West Lafayette, IN:

Ph.D. in Mechanical Engineering, December 2018

M.S. in Mechanical Engineering, August 2016

B.S. in Mechanical Engineering, August 2010

Employment Experience:

Purdue University, Ray W. Herrick Laboratories: Graduate Research Assistant, April 2015-December 2018

Rolls-Royce Aerospace: Senior Engineer, October 2012-January 2015

DENSO International America: Powertrain Cooling Design Engineer, November 2010 - September 2012

Publications:

Making the Grade: The Sensitivity of Class 8 Truck Fuel Consumption & Operational Behavior Predictions to Road Grade Data Quality, 2018, IEEE Transactions on Intelligent Transportation Systems, A Taylor, M Droege, G Shaver, D Bullock (*submitted*)

Diesel engine cylinder deactivation for improved system performance over transient real-world drive-cycles, SAE Technical Paper 2018-01-0880, 2018. M Joshi, D Gosala, C Allen, S Srinivasan, A Ramesh, M VanVoorhis, A Taylor, K Vos, G Shaver, J McCarthy Jr, L Farrell, E Koeberlein

Diesel engine aftertreatment warm-up through early exhaust valve opening and internal exhaust gas recirculation during idle operation, International Journal of Engine Research, 2017. D Gosala, A Ramesh, C Allen, M Joshi, A Taylor, M VanVoorhis, G

Shaver, L Farrell, E Koeberlein, J McCarthy Jr, D Stretch

Reducing diesel engine drive-cycle fuel consumption through use of cylinder deactivation to maintain aftertreatment component temperature during idle and low load operating conditions, *Frontiers in Mechanical Engineering*, 2017. M Joshi, D Gosala, C Allen, K Vos, M VanVoorhis, A Taylor, G Shaver, J McCarthy Jr, D Stretch, E Koeberlein, L Farrell

Intellectual Property:

Model-Based Compressor Surge Avoidance Algorithm for IC Engines Utilizing Cylinder Deactivation During Motoring Conditions, (*Under review with Cummins IP Board*)